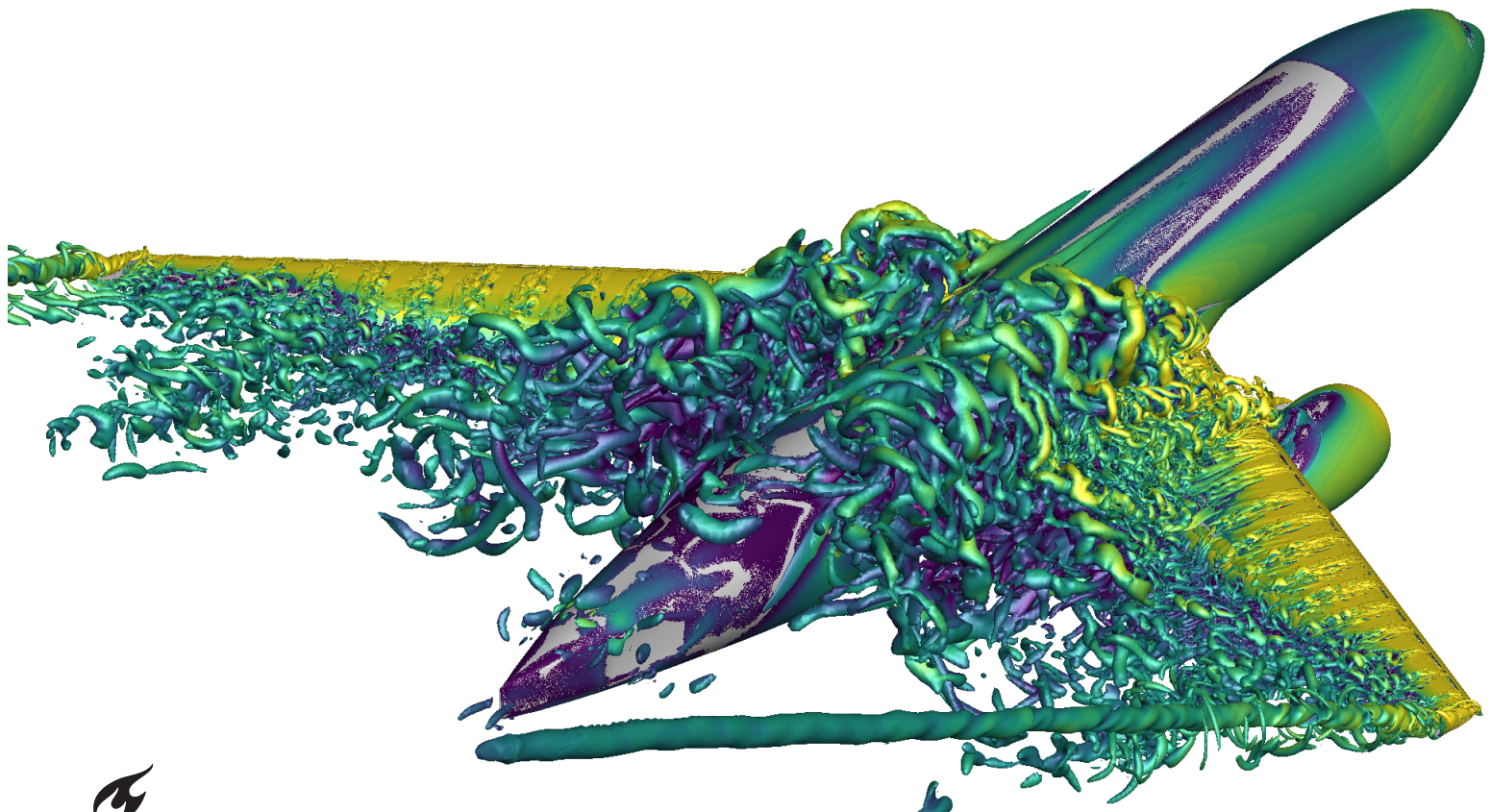


Aeroelastic Study of Leading Edge Minitabs for Gust Load Alleviation

Sharan S Pant



Aeroelastic Study of Leading Edge Minitabs for Gust Load Alleviation

Thesis report

by

Sharan S Pant

to obtain the degree of Master of Science
at the Delft University of Technology
to be defended publicly on November 29, 2024 at 10:00

Thesis committee:

Chair: Dr. Steven Hulshoff
Supervisors: Dr. Jurij Sodja
Dr. Alexander van Zuijlen
External examiner: Dr. Xuerui Wang
Place: Faculty of Aerospace Engineering, Delft
Project Duration: March, 2024 - November, 2024
Student number: 5689953

An electronic version of this thesis is available at <http://repository.tudelft.nl/>.



Copyright © Author Name here, 2022
All rights reserved.

Summary

This thesis investigates the aeroelastic behaviour of a flexible wing with minitabs and their effectiveness in alleviating the peak gust loads. Minitabs, which are small deployable surfaces located on the upper surface of the wing, were examined through a series of static and dynamic Fluid-Structure Interaction (FSI) simulations, which evaluated the aerodynamic and structural responses when deployed and stowed. The transient response of deployment of the minitabs indicated a greater load reduction capability compared to their steady-state performance. Notably, the peak alleviation of the minitabs is achieved when the gust peak lies within the aerodynamic reaction time of the minitab.

Evaluating the deployment of minitabs for various gust profiles further demonstrates that minitabs performed better in response to sharp, high-amplitude gusts, while their efficacy diminishes with longer gust lengths. When deployed at the ideal moment, the minitabs were found to reduce peak gust loads by an average of 5%. As a consequence of the mid-flight deployment and stowing of the minitabs, simulations revealed significant aeroelastic effects, characterized primarily by first bending mode oscillations at approximately 1 Hz. A sweep analysis of the deployment and stowing times revealed that delaying the actuation of the minitab beyond the ideal deployment or stowing time leads to an increased amplitude oscillations and extended recovery time to steady state conditions.

The study evaluated the performance of the minitabs in response to various gust profiles characterized by different gust lengths. The minitabs demonstrated improved performance in alleviating the gust peak loads from short, sharp gusts. However, the effectiveness in reducing the peak loads diminished for gusts of longer gust length and subsequent longer recovery time. The study also identified gusts with frequencies close to the natural first bending frequency of the wing structure as critical cases, where resonant behaviour emerges, leading to large amplitude oscillations and prolonged recovery times.

While minitabs effectively reduce peak lift and bending moments induced by gusts, they also introduce lower amplitude oscillations in the bending and torsion moments that persist over multiple cycles. While the peak moments do not exceed a magnitude that would raise a concern to the structural integrity, the subsequent prolonged multi-cycle oscillations in the moments raises concerns about potential fatigue life issues for the internal structure.

In conclusion, while this research confirms the potential of minitabs as a viable load alleviation method, it emphasizes the need for further investigation. Comprehensive aeroelastic studies on various minitab configurations, geometries and placements over the wing will provide a complete understanding of the aeroelastic effects of the minitabs and determine an ideal configuration to maximize the load alleviation capability.

Additionally, the original actuation method of the minitab involves the rotating them from a vortex generator position to the minitab position. This thesis simplified the actuation to a ON/OFF procedure. Further research is required to incorporate this motion to evaluate any aeroelastic effects resulting from this actuation motion.

Contents

List of Figures	v
List of Tables	vii
1 Introduction	1
1.1 Aeroelastic Analysis	1
1.2 Gusts	3
1.3 Load Alleviation	4
2 Minitabs - Theory and Concept	6
2.1 Background / State of the Art	6
2.2 Active Switchable Vortex Generators	9
2.3 Research Objectives and Questions	11
3 Methodology	12
3.1 Geometric Model	12
3.2 Aerodynamic Model.	14
3.3 Structural Model	24
3.4 FSI Scheme	26
4 Static FSI Results for Minitab Wing	31
4.1 Comparative Analysis of Clean and Minitab Wing.	31
5 Transient Simulation Plan for Minitab Wing	33
5.1 Methodology	33
6 Final Results of CFD and FSI simulations	37
6.1 Transient CFD Results	37
6.2 Minitab Deployment Midflight with No Gust (FSI)	38
6.3 Minitab Stowing Midflight with No Gust (FSI)	45
6.4 Conclusions from Simulations of Deployment and Stowing of Minitab	47
6.5 Clean Configuration with Various Gust Profiles (FSI)	48
6.6 Minitab Deployment Midflight with Gust (FSI)	51
6.7 Minitab Stowing after Gust Peak (FSI).	59
6.8 Final Deployment and Stow Scheme of the Minitab (FSI)	61
7 Conclusions and Future Recommendations	64
References	68
A Appendix	69
A.1 CAD Modelling Minitabs (Complete Procedure).	69
A.2 Damping Coefficient Sensitivity Study	74
A.3 Minitab Deployment on Gust cases (G2, G3)	77

Nomenclature

List of Abbreviations

ASVG	Active Switchable Vortex Generator
CAD	Computer Aided Design
CFD	Computational Fluid Dynamics
CRM	Common Research Model
DOF	Degree of freedom
DTR	Deploy Time Ratio
EAS	Equivalent Airspeed
EASA	European Aviation Safety Agency
FAA	Federal Aviation Administration
GLA	Gust Load Alleviation
RQ	Research Question
RST	Reynolds Stress Tensor

SA Spalart-Allmaras

STR Stow Time Ratio

SWBLI Shock Wave Boundary Layer Interaction

uCRM Undeformed CRM

VG Vortex Generator

List of Symbols

C_d	Drag Coefficient
C_l	Lift Coefficient
C_p	Coefficient of Pressure
T_{rea}	Reaction Time
T_{Rec}	Recovery Time

List of Figures

1.1	Collar's Triangle [collars]	2
1.2	Gust Alignments with respect to the aircraft	3
1.3	Wing Flex of a Boeing 787 inflight	4
1.4	Change in Load Distribution due to Gusts [7]	5
2.1	Flow streamlines around a Gurney Flap[12]	6
2.2	Lift and Drag polars for various chordwise placements [8]	7
2.3	Effect of minitab chordwise position on the lift and drag coefficient[13]	8
2.4	Velocity Contour Plot of Minitab, AOA = 0.6°, M = 0.78 [15]	9
2.5	Concept drawing of the ASVG [6]	9
2.6	3 Configurations of the ASVG [6]	10
3.1	CAD Model of the CRM9 Wing Jig Shape[17]	13
3.2	Minitab Geometry and Position	14
3.3	Overall Comparison of Computational Costs of Turbulence Models [26]	18
3.4	Fluid Domain Model	19
3.5	Lift Coefficient vs Number of Cells	20
3.6	Drag Coefficient vs Number of Cells	21
3.7	Lift Coefficient vs 1st cell height	22
3.8	Drag Coefficient vs 1st cell height	22
3.9	Volumetric Mesh of Fluid Domain	23
3.10	Prismatic Mesh around minitab	23
3.11	Volumetric Mesh around minitab	24
3.12	Example design of the internal wing structure without the skin	24
3.13	Beam Model[29]	25
3.14	Monolithic vs Partitioned Scheme[32]	26
3.15	Strong Coupling Scheme [33]	27
3.16	Weak Coupling Scheme [33]	28
3.17	Static FSI Flowchart	29
3.18	Dynamic FSI Flowchart for Minitab Deployment	30
4.1	Model Wing Shapes at Steady State	32
5.1	Simulation Run Plan for Dynamic FSI of Minitabs	33
5.2	Timeline of the lift coefficient variation due to deployment of the minitabs	34
5.3	Lift Coefficient Timeline with Gust	35
5.4	Complete Timeline of Minitab Deployment for GLA	36
6.1	Time-dependent variation of lift coefficient during minitab deployment: CFD	37
6.2	Time-dependent variation of lift coefficient during minitab deployment: FSI	38
6.3	Time-dependent variation of wing tip displacement during minitab deployment: FSI	39
6.4	Temporal variation of sectional lift forces at multiple spanwise locations	40
6.5	Root Bending Moment & Tip Displacement vs Time	41
6.6	Root Torsion Moment & Tip Twist Angle vs Time	41

6.7	Pressure distribution over upper surface for clean configuration	42
6.8	Pressure distribution at location of minitab installment	43
6.9	Sectional Pressure Coefficient for the clean and minitab configurations: Section 1 (75% Span)	44
6.10	Sectional Pressure Coefficient for the clean and minitab configurations: Section 2 (65% Span)	44
6.11	Wall Shear Stress streamlines over minitab installment location	45
6.12	Variation of lift coefficient with time for minitab stowing	46
6.13	Variation of tip displacement with time for minitab stowing	46
6.14	1-cos Gust Profile [35]	48
6.15	Variation of lift coefficient for all gust profiles in clean configuration	49
6.16	Variation of peak lift coefficient with gust length (m)	50
6.17	Effect of gust length on the recovery time(T_{rec})	50
6.18	Gust G1: Lift coefficient variation for different DTR values	52
6.19	Lift Coefficient at Gust Peak (G1) vs DTR Configurations	52
6.20	Gust G1: Wing tip displacement variation for DTR values	53
6.21	Gust G4: Lift coefficient variation for different DTR values	53
6.22	Lift Coefficient at Gust Peak (G4) vs DTR Configurations	54
6.23	Gust G4: Wing tip displacement variation for different DTR values	54
6.24	Gust G5: Variation in Lift coefficient between the clean and minitab configurations	56
6.25	Gust G5: Variation in Wing Tip displacement between the clean and minitab configurations	56
6.26	Gust G6: Variation in Lift coefficient between the clean and minitab configurations	57
6.27	Gust G6: Variation in Tip displacement between the clean and minitab configurations	58
6.28	Gust G1: Lift coefficient variation in response for different STR values	59
6.29	Gust G1: Wing tip displacement variation in response for different STR values	60
6.30	Lift Coefficient: Clean Wing and Minitab Wing with Deploy-Stow Cycle	61
6.31	Tip Displacement: Clean Wing and Minitab Wing with Deploy-Stow Cycle	62
6.32	Root Bending moment variation: Clean Wing and Minitab Wing with Deploy-Stow Cycle	62
6.33	Root Torsion moment variation: Clean Wing and Minitab Wing with Deploy-Stow Cycle	63
A.1	CAD Model of the uCRM9 Wing	69
A.2	Spline Sketch	70
A.3	Spline Surface Split Sketch	71
A.4	Ruled Surface Preview	72
A.5	Completed Minitab Surface of Wall Ratio = 1	72
A.6	Additional Surfaces due to Split Line Command (Wall Ratio = 0.4)	73
A.7	Example of a Fixed Version of Minitab Surface Model (Wall Ratio = 0.4)	74
A.8	Lift Coefficient vs Timestep (Modal Damping)	74
A.9	Tip Displacement vs Timestep (Modal Damping)	75
A.10	Lift Coefficient vs Timestep (Rayleigh Damping)	75
A.11	Tip Displacement vs Timestep (Modal Damping)	76
A.12	Lift Coefficient vs Timestep (Gust G2)	77
A.13	Lift Coefficient at Gust Peak (G2) vs DTR Configurations	77
A.14	Tip Displacement vs Timestep with (Gust G2)	78
A.15	Lift Coefficient vs Timestep (Gust G3)	78
A.16	Lift Coefficient at Gust Peak (G3) vs DTR Configurations	79
A.17	Tip Displacement vs Timestep with (Gust G3)	79

List of Tables

3.1 Minitab Design Parameters	14
3.2 Boundary Conditions	19
3.3 Mesh Size Parameters (100% Element Size)	20
4.1 Static FSI Results	31
6.1 Gust Profiles	49
6.2 Gust Profile (G5)	55
6.3 Gust Profile (G6)	57
6.4 Minitab Stow Time (Gust G1)	59

Introduction

The aviation market is largely fossil fuel driven, both physically and financially. With the establishment of sustainability goals for the future, there is a growing need for airplane manufacturers to design and build more efficient aircrafts in terms of fuel efficiency, aerodynamic efficiency, lifetime and serviceability requirements, acoustics and many more. With recent advancements in powerplant engineering, the structural part of the aircraft is now under heavy scrutiny. With rising fuel costs, stricter emission control and laws, there is a major need to develop and design more lightweight structures, while still maintaining the overall aerodynamic performance and efficiency. This aim has recently led to the use of composites such as carbon fibres, carbon plastic composites and alloys in main structural components such as wings, wingboxes, fuselages and more. These recent developments have however led to new and unique challenges to the whole aircraft development process.

1.1. Aeroelastic Analysis

Aeroelasticity deals with the behaviour of an elastic structure in an airflow where there is significant interaction between the two. In this definition, there is a heavy importance to the word 'significant'. The simultaneous interaction between the structure and the fluid can result in complex phenomena, resulting in unexpected and interesting behaviours.

Aeroelasticity is intimately connected in the field of aerospace engineering. Its importance has grown in modern aircraft design in the past few decades. The current trend in the design of new aircraft has shifted to lighter and slender aircrafts, which are beneficial for its impact on reducing induced drag, however it has brought increased flexibility to the structure as well. With current operating speeds and conditions for modern airliners, the expected deformations and deflections of these structures are significantly larger, leading to large amplitude aeroelastic responses.

It can be decomposed into 3 major interacting domains: Aerodynamic (A) , Elastic (E) , Inertial (I). The interactions between these 3 domains is represented in the Collar's Diagram Figure 1.1.

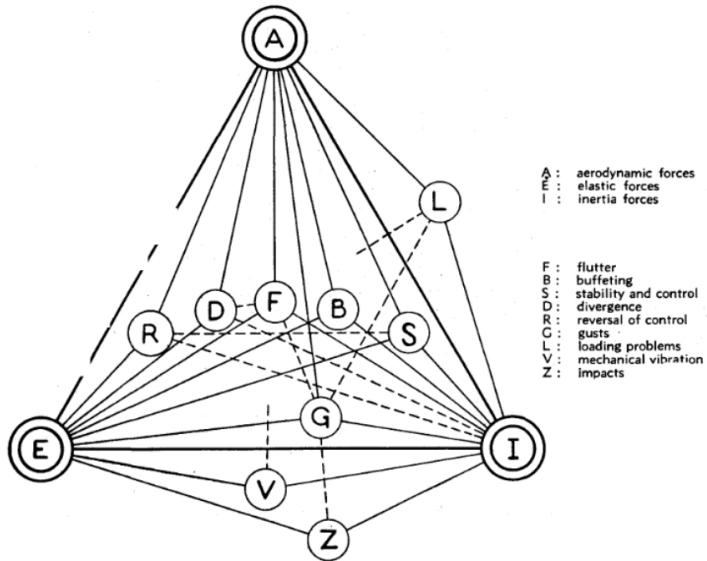


Figure 1.1: Collar's Triangle [collars]

The Collar's diagram is a representation of the forces involved in aeroelastic problems and how each individual sub-domain, for example gusts, mechanical vibrations etc. is interconnected with the 3 main domains. First, the aerodynamic forces are those caused by the interaction with the flow. Second, elastic forces arise from the structural properties of the studied object and appear when it is subject to deformation. Finally, inertial forces are related to the acceleration and mass of the object[1].

1.1.1. Transonic Aeroelasticity

An added complication to the aeroelastic study is the regime of flight. Most commercial airlines fly in the transonic regime ($M = 0.8-1.2$) during cruise. Transonic regime is a unique regime of flow where the emergence of flow non linearity is seen and viscosity and compressibility have profound effects, resulting in phenomena such as shockwaves, boundary layer separations, boundary layer bubbles, shockwave boundary layer interaction (SWBLI) and many more.

The calculation of aeroelastic response in the transonic regime holds significant importance in the design of aircraft. This is primarily due to the need to avoid phenomena such as transonic flutter or buzz, which are critical considerations in ensuring the safety and performance of the aircraft. In the transonic regime, even small displacements of the airfoil section can result in substantial changes in the aerodynamic forces and moments about the elastic axis. These unsteady aerodynamic characteristics often lead to aerodynamic instabilities, making flutter most likely to occur. Therefore, a thorough understanding and careful management of these factors are crucial in the successful design and operation of aircraft in the transonic regime [2].

Under purely subsonic and supersonic flow conditions, the flow equations are linearized with certain assumptions such as low mach numbers, potential flow, small perturbations present etc. This implies that the aerodynamic forces and moments vary linearly with the motion of the airfoil, providing a relatively straightforward relationship for analysis and prediction. However, under transonic flow conditions, the situation becomes more complex. The flow equations under these conditions are inherently nonlinear since the previously stated assumptions break down. Compressibility effects, shockwave formation and large disturbances in the flow due to objects in the flow are some of the reasons for the non linearity. These variations significantly affect the moments and forces acting on the airfoil. Hence we can conclude the transonic regime presents unique challenges in the analysis and prediction of aerodynamic behavior.

As a result of numerous aeroelastic studies done computationally and in wind tunnels, flow nonlinearity was found to be the cause of the complexity of transonic aeroelasticity. Nonlinearities can arise from aerodynamics (e.g. shocks, separation, vortices) and structural dynamics (freeplay, geometric and friction) [3]. The following thesis does not involve complex structure motions and deformations, it involves typical macro-structure motions such as pitch, heave and twist.

1.2. Gusts

Multiple sub domains that can be characterised within the 3 major domains from the Collar's Triangle. It showcases the complex intertwine of the whole picture, all of which have importance in its own way. The one to focus on for this thesis is Gusts (G). Gusts lies in the center, deeply connected to all 3 domains.

Gusts can be characterised as a sharp perturbation of the flow which can modify the aerodynamic characteristics of the wing. Gusts can have various alignments with respect to the aircraft as seen in Figure 1.2. As this is a discrete event, it is a dynamic phenomena, leading to local and time dependent load changes to the wing, and thereby inertial changes to the structure due to the time scale of action and local acceleration of the structure.

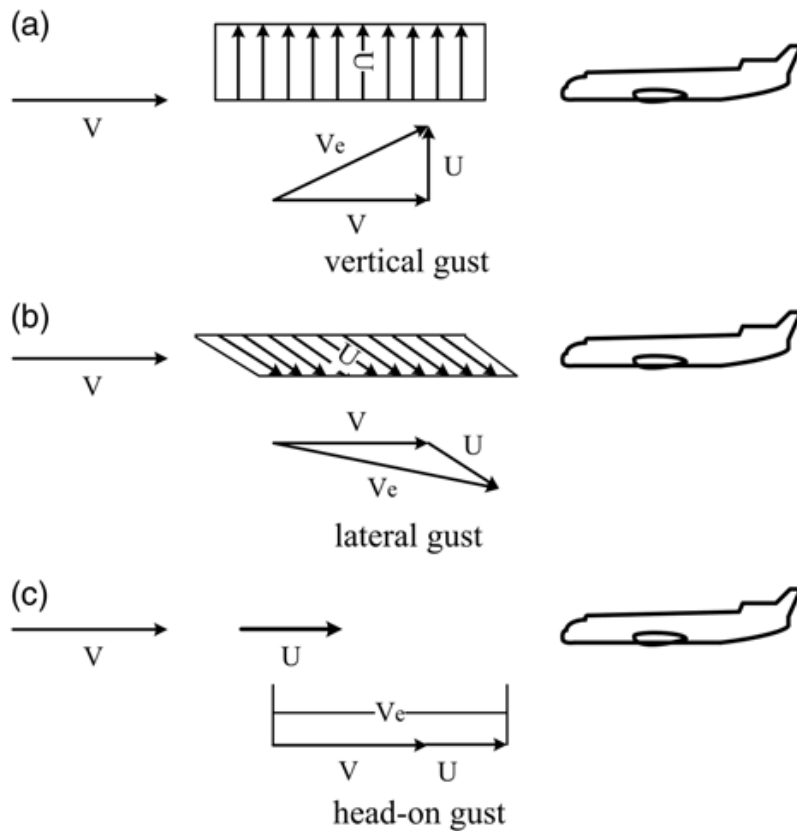


Figure 1.2: Gust Alignments with respect to the aircraft

These gust loads have been known to be a major cause for reduced fatigue life, single event damage to structure and overall reduced lifespan. Due to its potential dangers, aircraft wings are specially designed and tested both in the wind tunnel and in flight to mitigate its potential harmful effects. There also exists certifications set by the regulating authorities such as the Federal Aviation Administration (FAA) [4] and the European Aviation Safety Agency (EASA) [5] which every aircraft manufacturer must uphold and test.

The new generation composite wings, now seen on the Boeing 787, Airbus A350 have enhanced and prominent aeroelastic effects due to the increased flexibility of the composites used. These wings show significant bending, torsion, motion and vibrations when subjected to normal operating and adverse conditions such as gusts, high G maneuvers as seen in Figure 1.3.



Figure 1.3: Wing Flex of a Boeing 787 inflight

The sharp, high frequency loads due to these adverse conditions are serious concerns for the fatigue and overall life span of these highly flexible components. Hence there exists a need to study and develop load alleviation techniques and methods to improve the structure's life and fatigue characteristics when subjected to these sharp and extreme peak loads, given the increased usage of composites in aircraft manufacturing.

1.3. Load Alleviation

Load Alleviation can be defined as an action/technique to reduce the overall load over a structure in response to a prescribed event or time. This would be required in situations wherein one expects the loads to exceed a preset limit or beyond the load capacity of the structure. Load alleviation and control becomes a key factor in high-aspect-ratio wings, where offloading outer wing sections is vital to avoid the over-sizing of the wing structure, and the consequent weight penalty [6].

1.3.1. Active and Passive Load Alleviation

Passive Load alleviation can be categorized into either fixed devices/components attached to the wing such as vanes, fences, separation strips or modified structural designs to either control and restrict motion in particular directions, so called tailoring or control flow separation. Such devices and designs perform the load alleviation actions with no input or source powering them, hence named passive [6].

The most commonly deployed technique to enable load alleviation on wings is by the use of control surfaces and spoilers. These are characterised under Active Load Alleviation Techniques since it involves powered actuation of the devices to achieve the load alleviation. The loads, especially the lift distribution is modified due to the deployment of movable surfaces which change the overall wing shape, boundary conditions such as bending and torsional shape, local AOA in response to the change in flow conditions, maneuvers or a combination of both. Gusts can cause a sudden spike in lift, as seen in Figure 1.4 which results in an increase in wing root bending moment and tip loads. In the case of a gust encounter, the aileron actuation can adapt to the gust so the peak loads produced by the gust are reduced.

While it is a valid solution, it does require complex actuation systems, fast responding actuators and additional sensor arrays to detect sharp gusts, sudden high G maneuvers etc. In addition, the control surfaces are a significant part of the wing itself, Actuation to these surfaces can have profound

aeroelastic responses to the wing, and hence would be limited to small deflections. The actual actuation of such large surfaces makes it less effective to high frequency loads due to the actuation power and speed required to overcome the control surface's inertia itself. These solutions adds a lot of weight to the wing structure, which is going in the negative direction towards more fuel efficient and lightweight aircrafts.

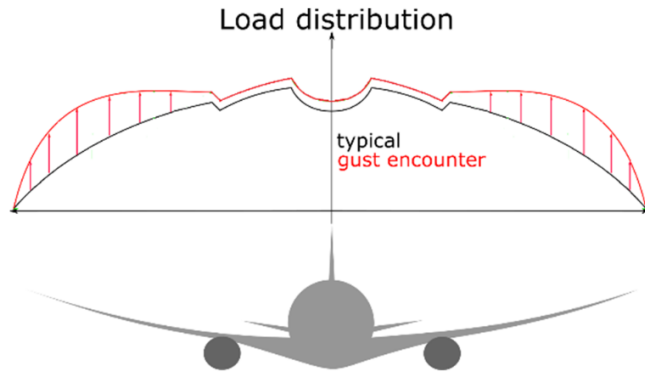


Figure 1.4: Change in Load Distribution due to Gusts [7]

Recently, the concept of minitabs has been experimented with for such purposes. They are a particular configuration of a proposed Active Switchable Vortex Generators(ASVG). ASVG are typical vortex generators, which can be actuated from a VG position to perpendicular to the flow, also known as a minitab. The main idea behind the minitab configuration is to act as a mini-spoiler, which is quick to actuate and effective enough to alleviate the loads due to gusts. An initial design of its multipurpose applications[6] shows a configuration of a combined vortex generator and a minitab, which will be discussed in detail in further sections.

2

Minitabs - Theory and Concept

2.1. Background / State of the Art

Aerodynamic loads can be highly time dependent, with reduced frequency = 0.75-1 during cruise. Current alleviation strategies (such as ailerons, flaps, and spoilers) are unable to control these loads: their large inertia limits their frequency response [8, 9].

Minitabs are small mechanical devices, with similar functionality and form as a gurney flap with the main difference being the location on the upper surface of the wing, close to the leading edge as compared to a typical gurney flap. These simple devices create a region of separated flow directly behind, with 2 counter rotating vortices trailing from the edges of the minitab as seen in Figure 2.1. These separated regions and strong vortices are key to change the load distribution over the wing. The increased pressure downstream of the separated flow disrupts the clean airflow on the upper surface of the wing, which is the main lift generating surface, thereby reducing the overall lift produced[9, 10, 11].

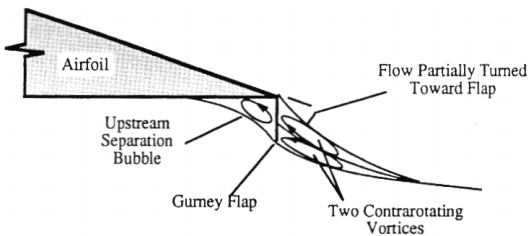


Figure 2.1: Flow streamlines around a Gurney Flap[12]

It is also expected to behave such that they are deployable only when required in extreme conditions such as gusts and maneuvers, and stowed away or placed in a neutral position when not required. For example, these minitabs are placed in a spoiler configuration to perform the load dumping action, and when in low speed conditions such as takeoff and landing configurations, placed at a small angle with respect to the flow such that it behaves like a vortex generator, providing increased lift during low speed flight at higher angles of attack by delaying the separation of the flow.

There are 2 major geometric parameters which determine the performance of the minitabs, the chordwise placement and height of the minitab. Heathcote et al. [8] conducted a comprehensive study on a 2D NACA0012 airfoil with different chord-wise placement and height of minitabs. Primary outcome of the study is that, the further the mini-tab is placed from the leading edge the higher the lift reduction but the increase in lift reduction is diminished the further away it is placed as the AOA increases. This can be seen in Figure 2.2 for various chordwise placements of the minitabs.

Locating the mini-tab at 60% chord length produces a more uniform lift reduction at low angles of incidence upto 5° AOA with a peak lift reduction of -0.60 obtained for a mini-tab of height, $h/c = 4\%$. Beyond 5° AOA, a change in the gradient of the lift polar is observed, with a reduction in the change in lift, ΔCL observed towards stall. The non-linear change in gradient implies a constant effect between 0° and 5° but beyond 5° , the effect reduces significantly towards stall[8].

The effect of the minitab location is more pronounced when placed close to the leading edge. At 15% chordwise distance, the lift polar starts deviating at a low AOA = 2.5° , with a reduced lift slop and a significant drop in Cl compared to the baseline. This effect is exasperated with the taller minitab ($h/c = 4\%$), which show significant change to the lift slope across all AOA, and early onset of stall.

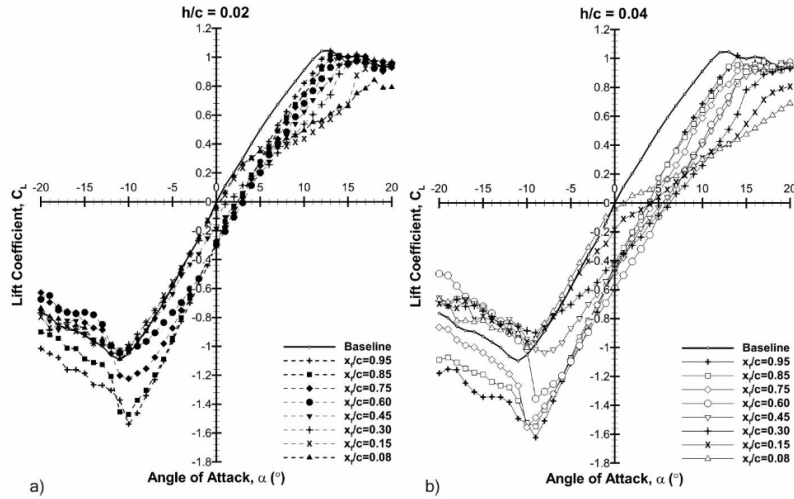


Figure 2.2: Lift and Drag polars for various chordwise placements [8]

Studies conducted by Baker et al. [13] and Jacobs et al. [14], tested various placements of the minitab upstream of the trailing edge on the S809 airfoil, and noted the effect on the change in Cl and lift curve slope. Placement of these minitabs at $\frac{x_f}{c} = 0.6$ showed significantly larger drop in Cl than placement at the trailing edge. Leading-edge placement ($\frac{x_f}{c} = 0.6$) significantly altered the lift curve, with the largest effect at the maximum lift coefficient producing $\Delta Cl = -1.0$.

It can also be noted, the significant increase in drag as the chordwise position of the minitab approaches the leading edge. From Figure 2.3, the 40% chord tab location causes a different lift behavior with an increased effect towards stall at low AOA. With an AOA sweep, this case appears to affect the lift curve almost identically to the 60% chord case until AOA reaches 0° , where a marked decrease in lift occurs until losing effectiveness at around 16° .

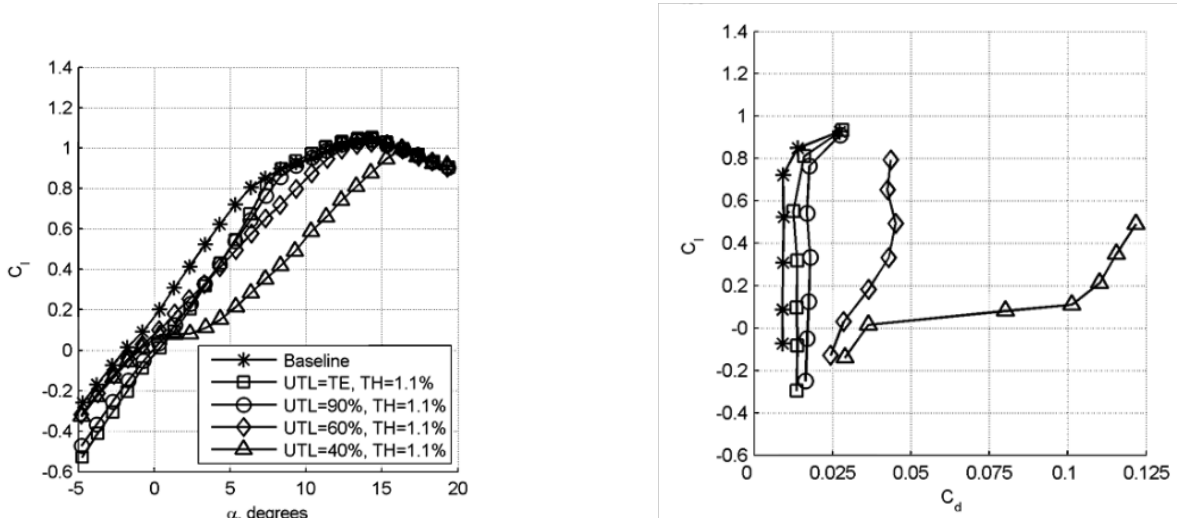


Figure 2.3: Effect of minitab chordwise position on the lift and drag coefficient[13]

A parametric 2D airfoil study of the minitab's dimensions and placements by Marino et al. [6] tested various heights and chordwise locations under transonic flow conditions. The study revealed that positioning the minitabs closer to the leading edge results in significant flow separation directly downstream of the minitab, and alters the position of the attached normal shock. Additionally when the minitab height is substantially increased, new shocks emerge on the upper and lower surfaces when the minitab height was very large.

The study also demonstrated that reducing the height of the minitab beyond a certain limit, the minitab is still significantly within the turbulent boundary layer. Its ability to produce strong vortices and flow separation is hence diminished, resulting in a lower load alleviation capability. Key findings from this study emphasizes close attention to parameters such as height, aspect ratio, chordwise and spanwise placement when integrating the minitabs into the wing design. Undesirable phenomena such as local flow acceleration and emergence of shockwaves on the lower pressure side of the airfoil were observed when the minitab heights were increased.

In order to determine the aerodynamic effect of these minitabs in high speed cruise conditions, high fidelity transonic static CFD simulations of these minitabs were conducted with varying height and wall ration in both 2D and 3D domains on the DLR F25 wing [15].

When the minitabs are deployed in cruise, large pressure buildups developed on the front face of the minitab. This is followed by a significant pressure drop across the minitab due to flow separation behind the minitab, but later reattached to the wing, with increasingly aft position for a greater minitab height as seen in Figure 2.4. With greater heights of the minitabs, the load alleviation capability also grew, but a significant drag penalty was introduced due to large flow separations seen in the wake of the minitab. The static CFD study of the minitab revealed that a minitab height of 0.03m placed at a chordwise location of 20% from the leading edge, can achieve a significant lift load reduction of 15% in comparison to the clean configuration.

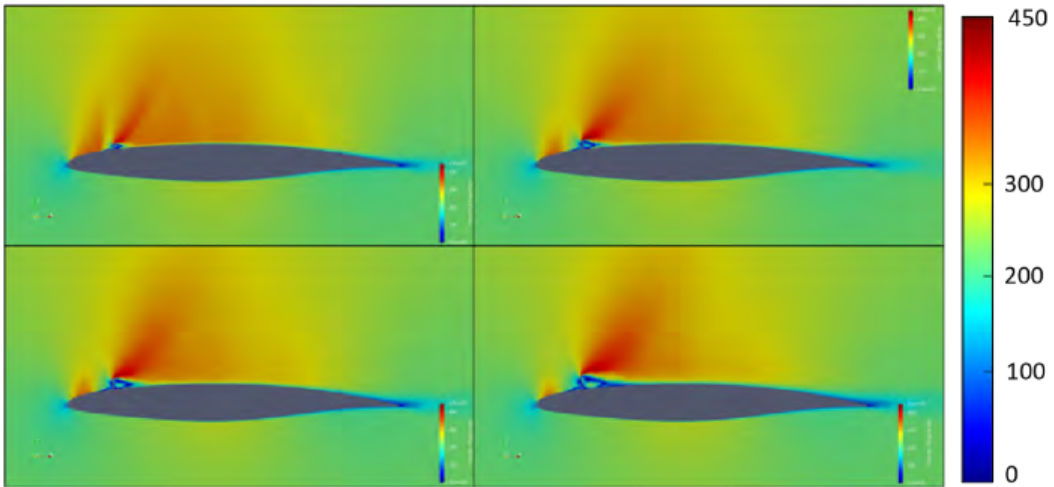


Figure 2.4: Velocity Contour Plot of Minitab, $\text{AOA} = 0.6^\circ$, $M = 0.78$ [15]

A majority of the previous literature and studies were limited to static steady state CFD simulations, which provides a good baseline for further development. Transient behaviour of the flow due to the presence of these minitabs was not included as a part of the study. Another key aspect to consider is that the minitabs were hard modelled into the wing model, with CFD simulations with the minitabs deployed from the start. Switching the minitabs on and off to simulate deployment and stow operations should be the next step to determine how this will affect the flow around the wing.

2.2. Active Switchable Vortex Generators

Active Switchable Vortex Generators(ASVG) is a novel proposed concept, which blends the functionality of a vortex generator(VG) and a minitab. Figure 2.5 represents a functional concept sketch of the ASVG, with various rotational positions.

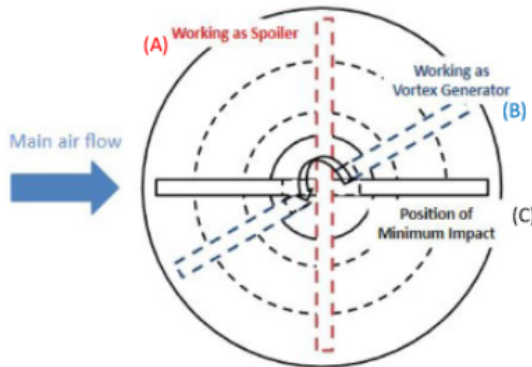


Figure 2.5: Concept drawing of the ASVG [6]

The functionality between the vortex generator and the minitab can be switched by a simple rotation of the ASVG. Figure 2.6 shows 3 possible configurations that can be set based on the regime of flight and the load alleviation requirement:

In cruise, the main goal is to minimize drag and thereby reduce fuel consumption. The ASVG will be aligned in the direction of the local flow and hence introduces minimal parasitic drag.

In low speed, high AOA cases, the ASVG is rotated to be slightly inclined with respect to the flow. The resulting configuration generates vortices from the tips of the ASVG. These vortices delay the onset of flow separation and increases the lift characteristics for higher angles of attack. This configuration is of particular importance during the takeoff and landing phases of flight.

In high speed cases, the ASVG can be rotated to be perpendicular to the flow for load alleviation. This configuration acts like a mini-spoiler, inducing flow separation. The separated flow over the wing results in a loss of lift and offloads the wing section. Manually inducing flow separation is a characteristic which can be utilized for alleviating large amplitude, high frequency loads such as gusts.

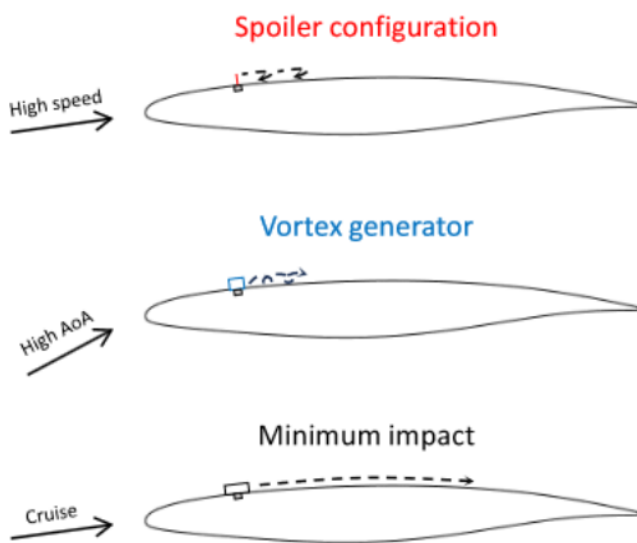


Figure 2.6: 3 Configurations of the ASVG [6]

A novel concept currently being worked on is to make this ASVG to stow when in cruise, to eliminate the unnecessary drag, and deploy when required in the presence of sudden peak loads. However, this thesis will focus on only the minitab model, and its actuation from stowed to deployed will be done with a simple ON/OFF condition.

While the fluid effects of these minitabs have been studied, there exists a general lack of research in its application to 3D wing geometries and how these devices influence a flexible wing when deployed. The aeroelastic effects of these minitab when deployed mid flight has not been studied and knowledge is sparse. There is a need to obtain a good understanding on the aeroelastic behaviour of wings with these minitabs to determine its efficacy in alleviating maneuver and gusts loads, which are of particular importance to flexible aircraft for not only certification of flight, but also for its life cycle and fatigue life. This thesis will build upon the previously conducted work, adding transient CFD simulations, static and dynamic aeroelastic responses of the wing, due to the presence of these minitabs.

Building upon the previously completed CFD Study of the Minitabs[15], the next step would be to study transient behaviours of these minitabs in high speed configurations and utilize this data to conduct an aeroelastic study to determine the responses of a flexible wing. The large gap in literature, requires prominent study and research in order to bring the concept to the next stage, wherein prototype and real world flight tests can be conducted.

2.3. Research Objectives and Questions

Research Question

Can Minitabs be introduced to a flexible wing design as a method to enable active gust load alleviation?

1. *What is the influence of a minitab deployment over aerodynamic factors such as lift and load distribution, spanwise local angle of attack etc. during cruise conditions?*
2. *When these minitabs are deployed in flight over a flexible (aeroelastic) wing, what are the temporal aerodynamic and structure responses of the wing?*
3. *Given the knowledge of the timescales of the effects of the minitabs, develop a scheme for deployment of the minitab for an incoming gust encounter to maximize load alleviation.*

3

Methodology

The methodology of the thesis is subdivided into Geometric, Aerodynamic and Structural Models followed by the FSI Scheme used.

3.1. Geometric Model

For this FSI study, the NASA Common Research Model (CRM) will be used. It is a representative model of a common transonic aircraft that is present today, particularly a Boeing 777-200. Vasseberg et al. [16] developed this model in 2008 for setting benchmark results for future aircraft development and research on upcoming iterations of the design.

This thesis will focus on the wing only, excluding the horizontal, vertical tail and the fuselage as the main focus is on the wing responses and motions. It is assumed, the inclusion of other surfaces of the aircraft will not have any major impact to the responses of the wing, if so, it will be very minimal. This model has been studied extensively by numerous authors for its aerodynamic, structure and aeroelastic behaviours, through wind tunnel experiments and computational methods as well.

The original designers calculated detailed aerodynamic performance data and CFD results that include wing pressure distributions with and without the nacelle/pylon, Lift by Drag ratios, and drag-divergence curves for various flow conditions [16], and will provide a solid foundation to validate the CFD and the coupled FSI codes.

An important point to note with the current CRM wing model is the fact that it was purpose built for aerodynamic analysis. This implies the wing is already deformed into the shape as it would ideally be in flight, so called "*1-g shape*". Given the aeroelastic nature of the research objective, we require a baseline undeformed shape of the CRM wing, a so called "*jig shape*", which deforms due to forces exerted by the flow.

Brooks et al.[17] introduced the uCRM to enhance its functionality for aeroelastic analysis. The uCRM features an undeflected wing that allows for in-depth exploration of the interaction between aerodynamics and structural dynamics. Due to the research objective, the uCRM is chosen as the benchmark model and will be used as a basis for developing the geometrical model.



Figure 3.1: CAD Model of the CRM9 Wing Jig Shape[17]

3.1.1. Modelling the Minitab Wing

The process of modelling the minitab over the uCRM9 wing was done with 2 key factors in check. One was to keep the modifications to literature backed and sourced models to a minimum, since it allows easy replication and ease in implementing updates for various future iterations and cases. Secondly, the actual methodology of modelling these minitabs should be computationally efficient and interference with geometric and mesh quality should be minimum.

To model the minitab surface in CAD, 'Ruled Surfaces' Tool on SolidWorks was used. Ruled surfaces allow the creation of surfaces that extend from edges in a specified direction [18]. This allows a surface to be created normal to the curvature of the underlying model. An added benefit of the ruled surface approach is that the normal from the underlying curvature is calculated at each point along the edge, rather than an average normal direction. This allows the minitab surface to also curve along with the normal as it spans across the edge. While this approach ensures that the flow is perfectly normal to the minitab all across the minitab surface, designing and manufacturing such surfaces is very difficult, since other factors such as the surface curvature complexity, ability to manufacture and its deployment mechanism installed in the wing, will all play a role in its final design.

The complete step-by-step procedure to model the minitab surfaces can be viewed in Section A.1.

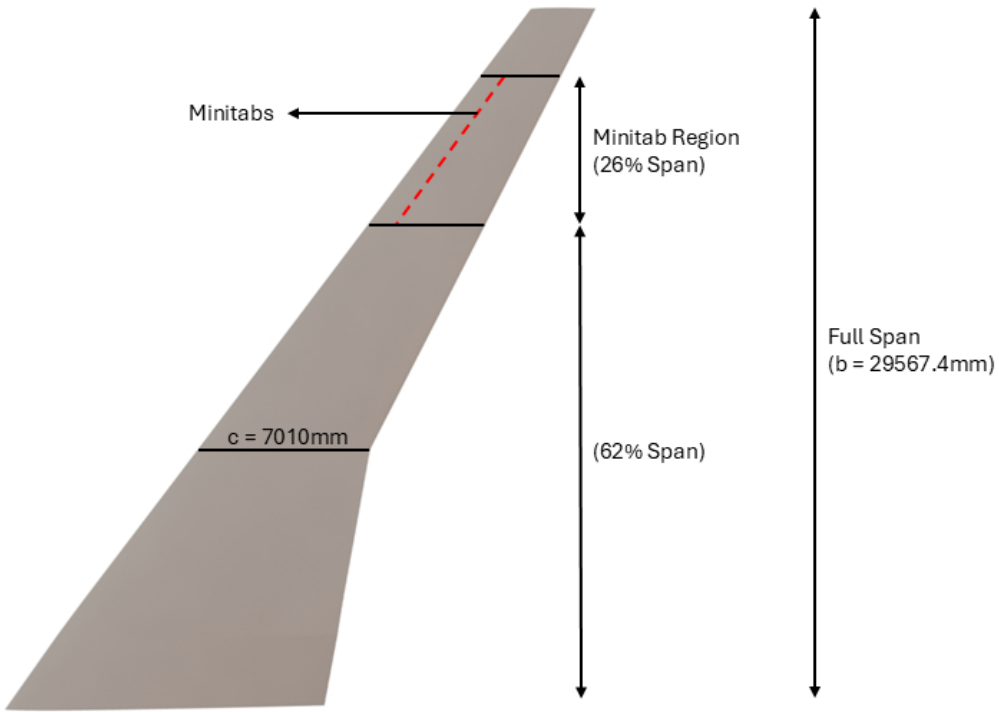


Figure 3.2: Minitab Geometry and Position

The minitabs are modelled as a permanent addition to the baseline uCRM9 wing design. The actuation and motion of the ASVG to switch from the VG to minitab was not modelled due to time and computational constraints. As stated previously, only the minitab configuration will be simulated with the actuation modelled through an ON/OFF switchable condition.

The main reference model for the FSI study as seen in Figure 3.2, has 1 particular configuration of the minitab setup, with design parameters listed in Table 3.1.

Table 3.1: Minitab Design Parameters

Parameter	Value
Height	75mm ($h/c = 1.07\%$)
Wall Ratio	0.4
Covering Span Length	9410mm ($y/b = [0.62 - 0.88]$)
Aspect Ratio	2

3.2. Aerodynamic Model

This section will explain the theoretical background of CFD simulations, followed by the CFD domain modelled, including details about mesh generation. Finally, the setup of the CFD solver is addressed.

3.2.1. Theoretical Background

The base equations which characterize flow in any domain are the Navier Stokes (NS) equations. NS equations describe the motion and transport of any fluid, with the effects of pressure, viscosity and external forces included [19]. NS equations are composed of 3 main components:

1. Conservation of Mass (Continuity Equation)
2. Conservation of Momentum
3. Conservation of Energy

The Continuity equation simply states that no mass can be lost or created in the process. For a Newtonian fluid, the continuity equation can be written as:

$$\frac{\partial \rho}{\partial t} + \nabla \cdot (\rho \mathbf{u}) = 0 \quad (3.1)$$

Conservation of Mass Equation

where ρ is the density and \mathbf{u} is the velocity in X direction.

In order to derive the NS equation for momentum, we start from the Continuity equation, and replace the intensive property used with mass flux. Mass flux is the product of mass and velocity, which is substituted into the continuity equation.

$$\mathbf{u} \left(\frac{\partial \rho}{\partial t} + \nabla \cdot (\rho \mathbf{u}) \right) + \rho \left(\frac{\partial \mathbf{u}}{\partial t} + \mathbf{u} \cdot \nabla \mathbf{u} \right) = \mathbf{s} \quad (3.2)$$

Using the Material Derivative notation, Equation 3.2 can be written as:

$$\rho \frac{D\mathbf{u}}{Dt} = \rho \left(\frac{\partial \mathbf{u}}{\partial t} + \mathbf{u} \cdot \nabla \mathbf{u} \right) = \mathbf{s} \quad (3.3)$$

where \mathbf{s} is the source of momentum.

Based on Newton's 2nd Law, the net momentum source term can be split into 2 terms, 1 to describe the internal stresses, known as the Cauchy Stress Tensor[20], and other to describe the external forces.

$$\rho \frac{D\mathbf{u}}{Dt} = \nabla \cdot \boldsymbol{\sigma} + \mathbf{f} \quad (3.4)$$

Expanding the stress term in a more explicit format, it can be written as the sum of Pressure and Viscous Forces. Overall the final Momentum Equation can be written as: where μ is the dynamic

$$\rho \left(\frac{\partial \mathbf{u}}{\partial t} + \mathbf{u} \cdot \nabla \mathbf{u} \right) = -\nabla p + \mu \nabla^2 \mathbf{u} + \frac{\mu}{3} \nabla (\nabla \cdot \mathbf{u}) + \mathbf{f} \quad (3.5)$$

Conservation of Momentum Equation

viscosity, p is the pressure and f is the external force.

Similar steps can be followed by substituting energy flux as the intensive property into the continuity equation in order to obtain the Energy Equation as well [19]:

$$\frac{\partial \rho E}{\partial t} + \nabla \cdot (\rho \mathbf{u} E) = \boldsymbol{\sigma} : \mathbf{S} - \nabla \cdot \mathbf{q} - \mathbf{f} \cdot \mathbf{u} + q'' \quad (3.6)$$

Conservation of Energy Equation

where q is the heat flux, S is the strain rate tensor and E is the total energy.

Currently, a complete, universal and rigorous solution to these equations has yet to be discovered, however, several assumptions and simplifications can be made based on the speed regime, computational domain, required accuracy of the final solution and many more, in order to get a relatively accurate solution.

Transonic Flow

The domain of transonic flow (Mach 0.8 to 1.2) is a complex compressible flow regime, with emergence of highly non linear flow characteristics such as shockwaves, boundary layer separations and interactions with the shockwaves and many more. There is a lack of a complete understanding of characteristics of turbulent flow such as emergence of instabilities, transitions and the overall chaotic nature. The transonic region of speed is generally the initial point in which these turbulent characteristics have large influences over the mean flow.

Turbulence can be characterized as instability of laminar flow at high Reynolds Numbers due to interactions between the inertial and viscous effects of the fluid. An important characteristic of Turbulence is the random nature of the flow. The previously mentioned interactions are highly temperamental and unpredictable, which makes it very hard to have certainties regarding its location, strength, and its influential region. Unfortunately for engineers, Turbulence seems to have dominance over other flow phenomena, whenever present [21]. This prompted research into developing analytical turbulence models which can approximate the transient flow phenomena accurately as possible. However, the lack of a universal model for turbulence still means certain assumptions are taken, and simplifications are created to obtain solutions within the user's tolerances.

3.2.2. Turbulence Frameworks

RANS Framework

A frequently used turbulence framework is the Reynolds Averaged Navier Stokes (RANS) Framework. The Reynolds Averaged Navier–Stokes (RANS) equations, obtained by time averaging the NS equations, are usually employed to simulate turbulent industrial flows. RANS is based on the principle of the decomposition of Reynolds, which divide the instantaneous measures into a sum of a mean and a fluctuating value[22]:

$$u = \bar{u} + u' \quad (3.7)$$

Substituting this equation into the momentum equation of NS, gives the Reynold's Convection equation:

$$\rho \bar{u}_j \frac{\partial \bar{u}_i}{\partial x_j} = \rho \bar{f}_i + \frac{\partial}{\partial x_j} \left[-\bar{p} \delta_{ij} + \mu \left(\frac{\partial \bar{u}_i}{\partial x_j} + \frac{\partial \bar{u}_j}{\partial x_i} \right) - \rho \bar{u}'_i \bar{u}'_j \right] \quad (3.8)$$

Equation 3.8 involves the double correlation of multiple fluctuating quantities called the Reynold's Stress Tensor $[-\rho \bar{u}'_i \bar{u}'_j]$, which is physically not possible to measure or evaluate analytically. The RANS equations are built to spend a majority of their computational resources to compute the components

of the Stress Tensor. The process of averaging involves a loss of temporal information, hence its application to flows with fewer instabilities and changes versus time.

While the computational time and overall solver accuracy is good to study time averaged flows, the main drawback for this application is the averaging process itself. The highly temperamental behaviour of transonic flow is lost in the process, and its possible influence and interaction with the structure is never evaluated.

In order to have better temporal resolution of the flow, an unsteady form of RANS model can be utilised. (U)RANS is setup by retaining the time dependent terms of the mean velocity of RANS. This means the averaging process can be considered as ensemble averaging of turbulent states of the flow.

$$\begin{aligned}\frac{\partial \bar{u}_i}{\partial x_i} &= 0 \\ \frac{\partial \bar{u}_i}{\partial t} + \bar{u}_j \frac{\partial \bar{u}_i}{\partial x_j} &= -\frac{1}{\rho} \frac{\partial \bar{p}}{\partial x_i} + \frac{\partial}{\partial x_j} \left(\nu \frac{\partial \bar{u}_i}{\partial x_j} \right) + \frac{1}{\rho} \frac{\partial \tau_{ij}}{\partial x_i}\end{aligned}\quad (3.9)$$

Unsteady RANS Equations

To evaluate the Reynolds Stress Tensor, models apply an analogy between molecular diffusion and turbulent mixing, and thus approximate the Reynolds stress in terms of the mean flow gradient together with a spatially varying turbulent viscosity based on local turbulent time velocity and length scales [23].

DNS Framework

Direct Numerical Simulation (DNS) is a turbulence framework, which resolves all the turbulent length and time scales by the computational grid and time step chosen for the problem. This requires very fine three-dimensional grids to resolve the small, dissipative turbulent length scales. Typically, these scales require an immense amount of computational resources and time as seen in Figure 3.3, however, it produces highly accurate solutions [24].

LES Framework

LES has been developed in an attempt to reduce the grid resolution requirements of DNS. LES uses a filtering technique to capture the larger eddies in the flow and numerically model the smaller eddies using a subgrid turbulence model, in order to give information of the flow over a large range of scales. LES provides a more detailed image of the turbulent scales in the flow, for a fraction of the resources that DNS requires. LES is significantly more computationally heavier than RANS, utilizing 2-3 times more resources for a comparable RANS code.

While each one of these turbulence frameworks have their advantages and disadvantages, selection of a turbulence model is highly dependent on the type of case being simulated. These factors can be divided into 2 main sections:

1. Model and Flow Domain Characteristics
2. Computational Resources Availability

During the process of evaluation and selection of a turbulence model, Zhang et al. [25], noted that flow in the transonic domain is dominant in transonic aeroelasticity, however, comparative flutter and transonic buzz analyses showed that an URANS model was sufficient for the pressure force outputs and modelling phenomena such as shock and shock oscillations. Therefore, with an appropriate turbulence model, the URANS method is suitable for the simulation of transonic unsteady problems, i.e. transonic buffet flow.

This model will be well suited to simulate a typical aeroelastic response of the wing to gusts in cruise. While other models such as LES and DES will be able to model the wake regions and boundaries much

better than RANS, it does not fall into the scope of this thesis, which will be more focused on the shock wave and its corresponding forces over the wing.

	DNS	LES	RANS
Physics	full	high	low
Grids	$Re^{9/4}$	$Re^{9/5}$	$\log(Re)$
Computations	$\geq Re^3$	$Re^2 - Re^{2.5}$	Re weakly
Applications	simple flow low Re number	simple flow low Re number	wide

Figure 3.3: Overall Comparison of Computational Costs of Turbulence Models [26]

3.2.3. RANS Turbulence Models

Turbulence models within the categories of RANS, majority of them, use the Boussinesq Formulation to characterise the RST. The Boussinesq Formulation relates the RST to the mean strain rate tensor, which correlates the stresses from turbulence and viscous effects [27].

$$-\rho \overline{u'_i u'_j} = \mu_t \left(\frac{\partial U_i}{\partial x_j} + \frac{\partial U_j}{\partial x_i} \right) - \frac{2}{3} \rho k \delta_{ij} \quad (3.10)$$

Various RANS turbulence models such as Spalart-Allmaras (SA), K- ω and K - ϵ , provide formulations to the turbulent viscosity term. For this thesis, the Spalart-Allmaras model was chosen for the CFD solver. Key reasons for the choice are:

1. Single Equation Model: More computationally efficient, than the 2 equation models of K- ω and K - ϵ .
2. Wall Treatment: The walls in SA model, satisfy the Dirichlet condition, which is a more numerically stable model.
3. Adverse Pressure Gradients: It performs well for boundary layer flows and flows with abrupt pressure gradients, such as shock boundaries, boundary layers, flow separations [28].

3.2.4. CFD Domain and Setup

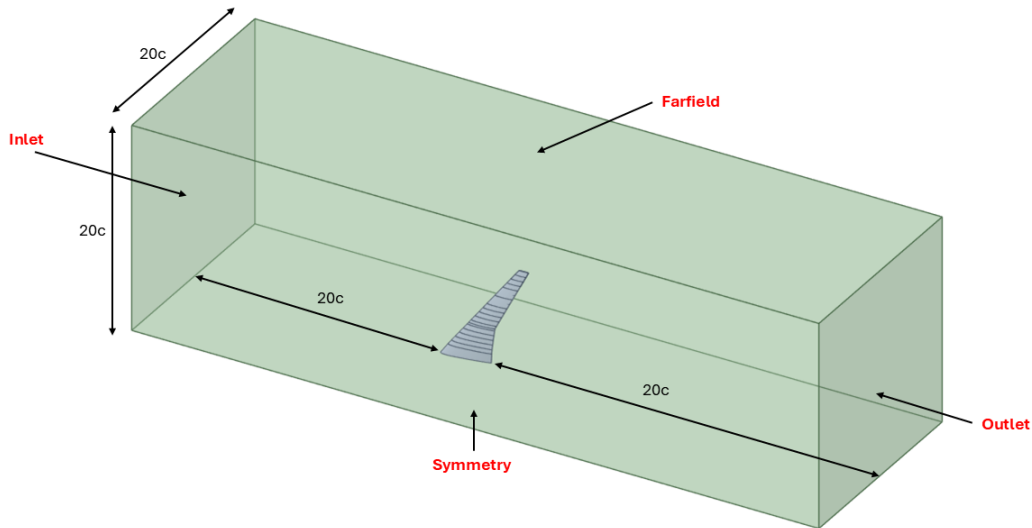


Figure 3.4: Fluid Domain Model

The CFD domain consists of the uCRM9 wing, in a rectangular fluid domain. Each surface of the fluid domain is kept 20 chord lengths away from the wing, in order to avoid any undesirable influence of the boundaries.

The speed regime of the flow is transonic flow, hence compressibility of the fluid must be accounted for, which means the density and viscosity of the fluid cannot be kept constant. The density is set to follow the "*Ideal Gas Law*" and viscosity set to follow "*Sutherland's law*". The wing is set to be simulated in cruise conditions at an altitude of 11000m, giving a decreased operating pressure of 22000Pa, temperature of 215K and a density of 0.35kg/m^3 .

Boundary conditions set for the various surfaces in the CFD Domain are listed in Table 3.2:

Table 3.2: Boundary Conditions

Surface Name	Boundary Condition Type
Inlet	Pressure-Far-Field ($M = 0.85$) ; $\text{AOA} = 0^\circ$
Outlet	Pressure-Far-Field ($M = 0.85$) ; $\text{AOA} = 0^\circ$
Farfield	Pressure-Far-Field ($M = 0.85$) ; $\text{AOA} = 0^\circ$
Symmetry	Symmetrical Boundary
Wing	Wall
Minitab	Interior to Wall (Switch)

3.2.5. Mesh Generation

During the meshing process, quality of the cells alone is not the only parameter to consider. Since the simulations are of FSI nature, the mesh should be able to deform, while retaining mesh quality. Considering the fact that the mesh needs to deform large distances, multiple times the size of the

smallest cells, having a coarser mesh results in a more stable FSI simulation, as the cell sizes itself are larger.

Table 3.3: Mesh Size Parameters (100% Element Size)

Parameter	Value
Wing Surface Mesh Max Size	250mm
General Surface Size	250mm - 25000mm
Volume Element Type	Tetrahedral
Volume Element Max Size	32084mm
Total Cell Count	7149991

2 mesh sensitivity studies of the uCRM9 wing alone were performed, one with the FSI turned off and another with the FSI turned on. This would help determine to what level of coarseness, the mesh can be kept while keeping the overall accuracy of the solutions as high as possible.

For the overall mesh element size sensitivity, taking a reference mesh as the 100% element size mesh, 4 levels of refinement were chosen: [80%, 60%, 50%, 40% reference mesh element size]. It is important to note that the 1st cell height in the boundary layer prismatic mesh was kept constant.

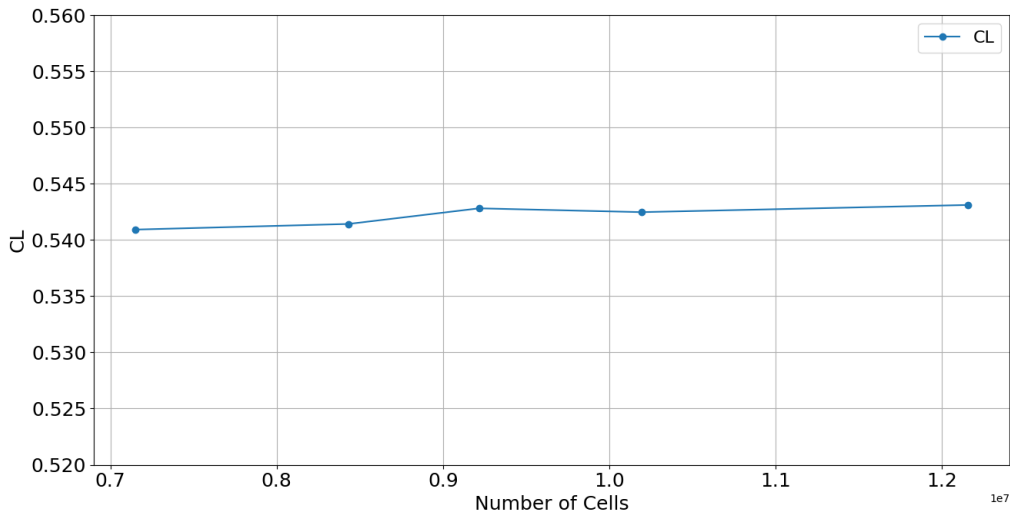


Figure 3.5: Lift Coefficient vs Number of Cells

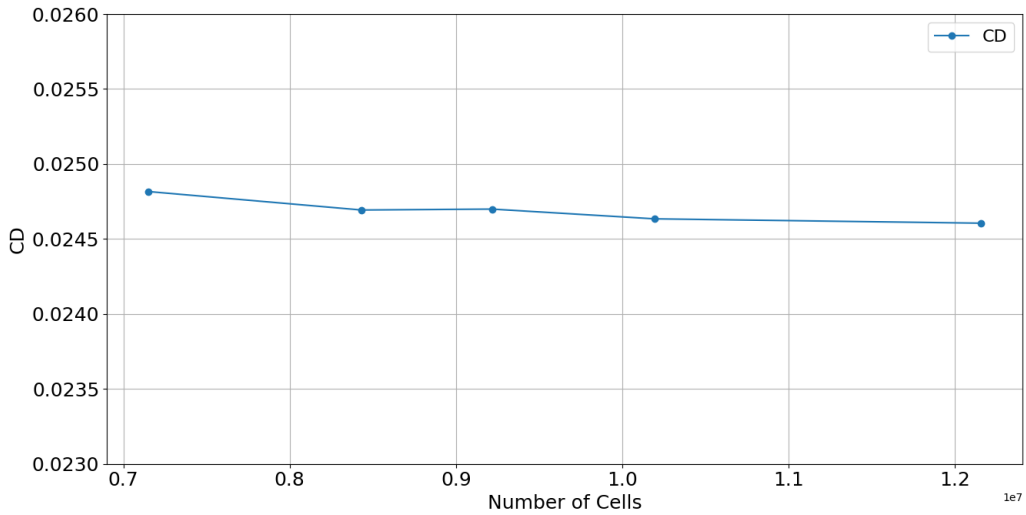


Figure 3.6: Drag Coefficient vs Number of Cells

Variability of the results is very low, with negligible differences when moving from 100% element size to 40% element size. Hence keeping the coarsest option (100% size) is preferred since the computational requirements are lower with the accuracy of the solution remaining high.

Another mesh sensitivity analysis was conducted with the Static FSI turned on. The variation in the mesh in this case, was the 1^{st} cell height from a wall surface. The prismatic cells of the boundary layer mesh have large aspect ratios and small heights, making them the most sensitive to the mesh motion accuracy and stability of the FSI simulation. A more refined 1^{st} cell height and subsequent boundary layer refinement allows the viscous effects to be captured better due to a lower y^+ value, however it can cause stability issues and subsequent mesh fails when mesh motion is imposed.

4 heights of the 1^{st} cell were simulated on a clean wing with Static FSI enabled [1mm, 0.5mm, 0.1mm, 0.05mm]. A 1^{st} cell height of 0.05mm gave the lowest average $y^+ = 7$, however the FSI simulation crashed mid way due to the failed dynamic mesh motion, producing negative cell volumes.

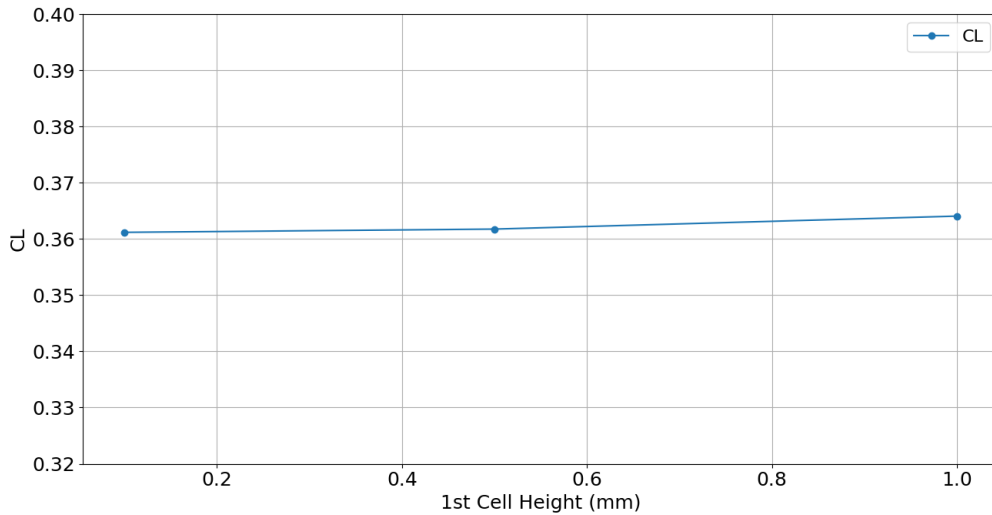


Figure 3.7: Lift Coefficient vs 1st cell height

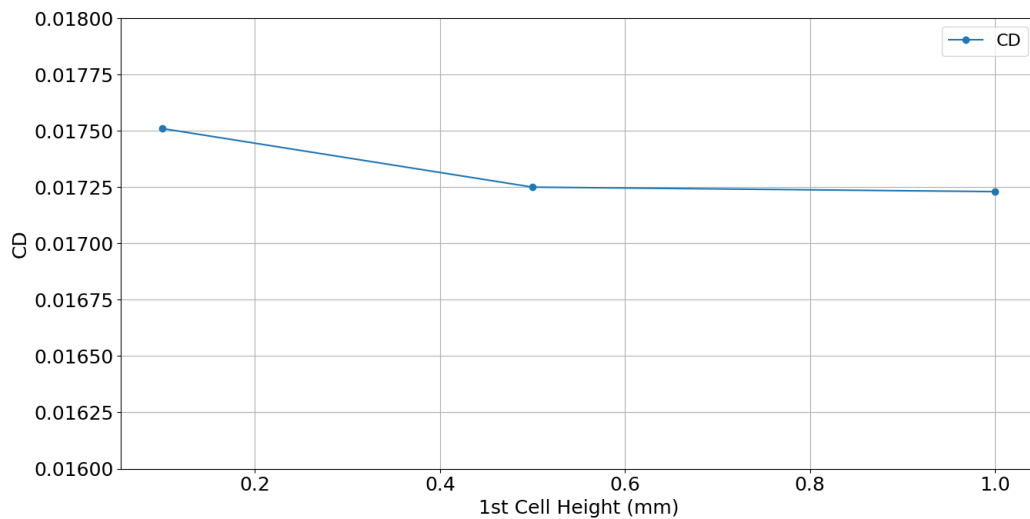


Figure 3.8: Drag Coefficient vs 1st cell height

A 1st cell height of 0.1mm is the most viable option, in terms of accurately modelling the boundary layer and gradients, however mesh quality checks during the FSI simulation showed very poor quality cells, with high skewness and low orthogonality. Given the requirements for a stable FSI simulation, while maintaining a good level of accuracy, a 1st cell height of 0.5mm was chosen for all the models used.

3.2.6. Final Mesh

The volume mesh with mesh parameters as seen in Table 3.3 is displayed in Figure 3.9

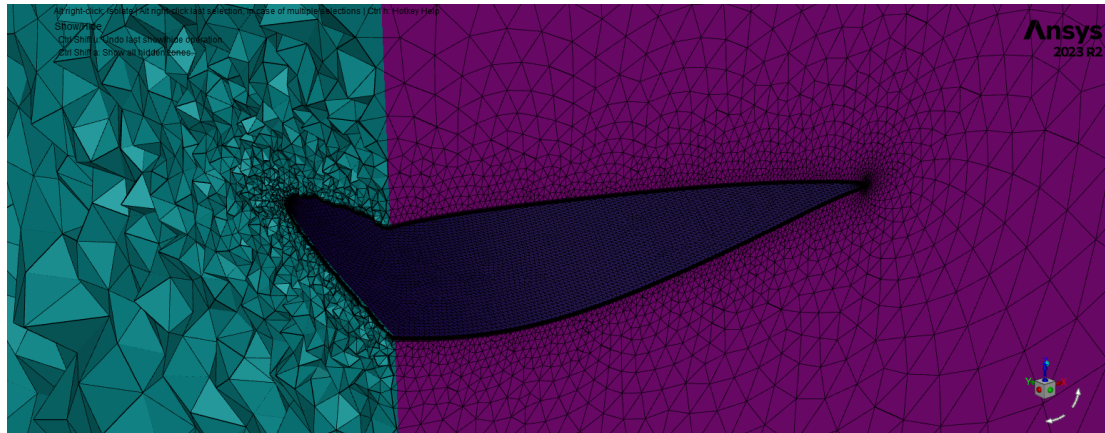


Figure 3.9: Volumetric Mesh of Fluid Domain

The minitab modelled as a surface, requires the mesh to be conformal on both sides of the minitab for higher accuracy. This ensures that the forces and flow around the minitab is transferred across the minitab without any interpolation error.

To capture the gradients and flow near the minitab, the boundary layer mesh itself, is extended upto the height of the minitab. The prismatic layer of cells with very high aspect ratio, captures the intricate flow details around the minitab.

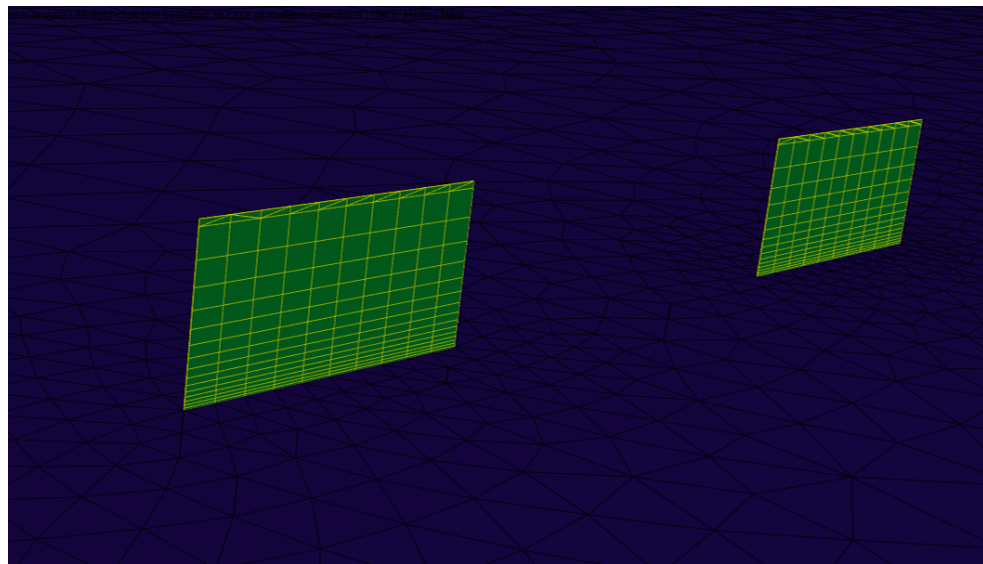


Figure 3.10: Prismatic Mesh around minitab

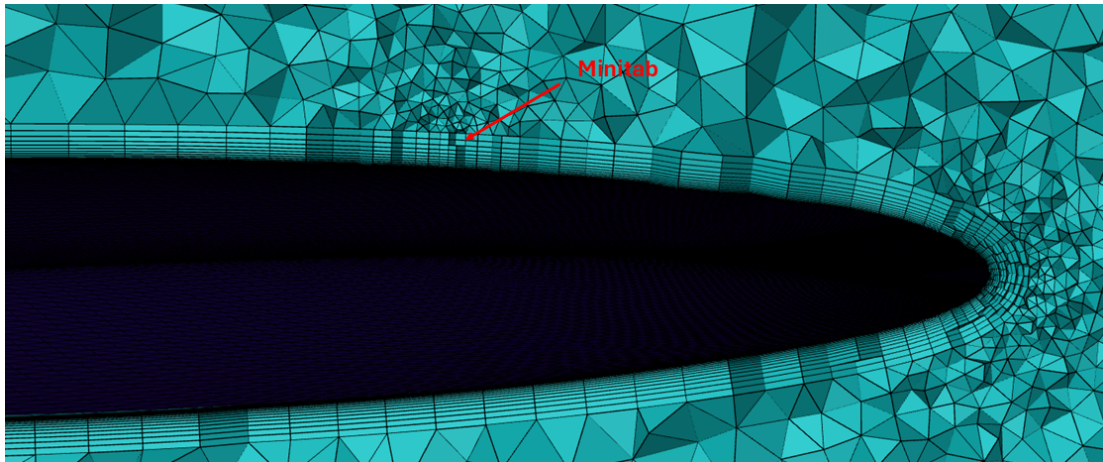


Figure 3.11: Volumetric Mesh around minitab

3.3. Structural Model

Most modern wing designs use an internal substructure called a wingbox for strength and stiffness. The wingbox is the primary load carrying part of the wing. The wingbox consists of ribs enclosed by stiffening spars, which is then surrounded by the external aerodynamic surface.

Two versions of the structural model are taken for this thesis. The Static FSI was conducted with a complete wingbox FEM model. Due to the computational resources and time required for Dynamic FSI simulations, the FEM model is reduced to a beam model.

3.3.1. Wingbox FEM model

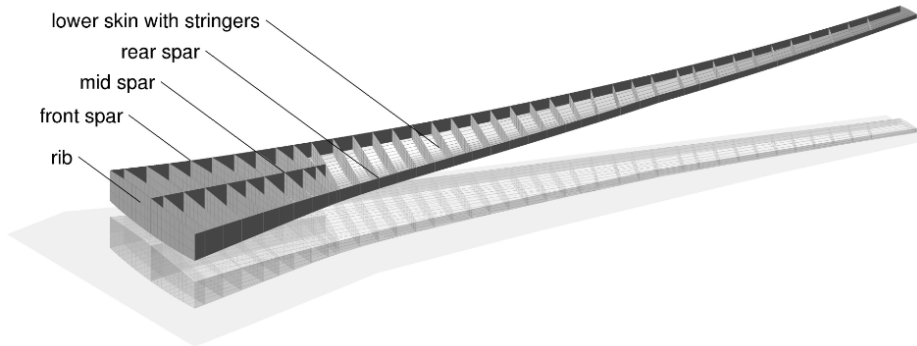


Figure 3.12: Example design of the internal wing structure without the skin

A typical design of a complete wingbox FEM model is depicted in Figure 3.12. It consists of 2 main components: Ribs and Spars.

Front and rear spars carry the majority of the bending and shear loads of the wing, and the general hollow box shape structure contributes to the torsional rigidity of the wing. Mid spars may or may not be a part of the internal wing structure, depending on the size and geometry of the wing, but are usually present for additional strength and load distribution.

Ribs are inserted at periodic sections along the span to support and maintain the external aerodynamic profile of the wing. The ribs also allow the wing to be supported, while leaving major volumes inside the wing empty. These volumes are used for storage of fuel.

For this thesis, the structural model used in this project was provided by the Technical University of Delft which is an in-house developed CRM structural model based on the undeflected CRM structure previously presented by Brooks et al.[17].

3.3.2. Beam Model

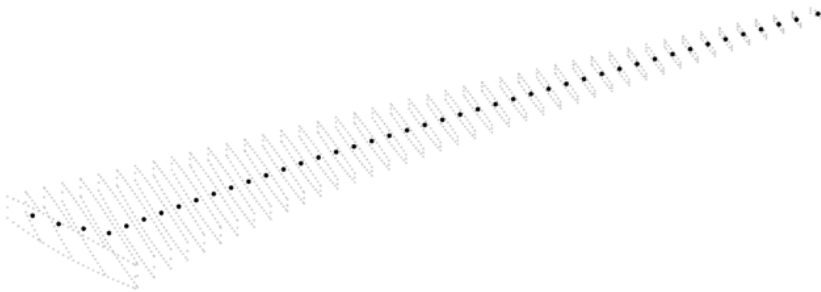


Figure 3.13: Beam Model[29]

In order to reduce the model from the full wingbox to a beam element model, the nodes at the centroid of each of the 44 ribs in the FEM wingbox model were taken to be the beam model. A generalized mass-spring-damping equation is used to calculate the displacement, velocity and acceleration of each of the nodes, subjected to the external aerodynamic loads.

$$MX'' + CX' + KX = f(t) \quad (3.11)$$

where M is the mass matrix, C is the damping matrix, K is the stiffness matrix, X is the DOF of the node and f(t) represents the external force.

NASTRAN offers a "*Model Reduction and Superelements*" process to take in a finite element model, and split it into interior and exterior nodes. The FEM of the component is then mathematically reduced to just the interior nodes, before assembling it into a model of the system. By providing the complete wingbox structure, NASTRAN converts this model into a reduced beam element model and the corresponding mass and stiffness elements are exported as a "pch" punchfile using the (DMIGPCH) command.

Damping Coefficient Calculation

Calculation of the damping coefficient values of a structure is not very intuitive, and typically requires experimental setups such as modal analysis, ground vibration tests (GVT), to determine the damping coefficient values[30]. A previous study by Lancelot [31], utilized a modified version of the same FSI code with a damping coefficient of 10% (K), however a firm reasoning for the chosen value was not established. To justify a reasonable value for the damping coefficient, 2 methods of Damping Coefficient were tested:

1. **Rayleigh Damping:** $C = \alpha.M + \beta.K$

For this thesis, $\alpha = 0$, and $\beta = [0\%, 2\%, 5\%, 10\%]$ were tested as part of the sensitivity analysis.

2. **Modal Damping:** $C = LPD_m P^T L^T$ where $D_m = D_m = \begin{bmatrix} 2\zeta_1\omega_n^{(1)} & \dots & 0 \\ \vdots & \ddots & \vdots \\ 0 & \dots & 2\zeta_p\omega_n^{(p)} \end{bmatrix}$

The model is transformed into modal coordinates, through calculation of all the eigen modes. The damping coefficient is determined through a reasonable set of Damping Ratio values (ζ) [2%, 3%, 4%, 5%], multiplied with the eigen frequencies and transformed back into Cartesian coordinates.

Details on the various test cases and the results from the sensitivity analysis can be viewed in the Appendix Section A.2. As a result from this study, a Rayleigh Damping Coefficient value of 5% (K) was chosen for all the dynamic FSI simulations.

3.4. FSI Scheme

In order to study aeroelastic behaviour, it will involve the synergy between the structure and the aerodynamics, in terms of loads and displacements. The structural and aerodynamic simulations are going to be handled separately on different solvers, and hence would need to be able to communicate with each other.

For this thesis, the aerodynamic solver (CFD) is ANSYS Fluent and the Structure Solver is NASTRAN. The reasons for the choices for these softwares was due to industry wide spread use and commercial availability with good maintenance and update schedules and the fact that these softwares are actively being used and relied upon in the aerospace industry.

The static FSI solver will have the complete coupling of the 2 solvers, running concurrently until solution is converged. For the dynamic FSI simulations, NASTRAN is used to reduce the wingbox FEM model to a beam model, CSM calculations are handled by solving the equation of motion for displacements, velocities and accelerations of the nodes.

The inherent fluid structure interaction model can be one of 2 types:

1. Monolithic Scheme
2. Partitioned Scheme

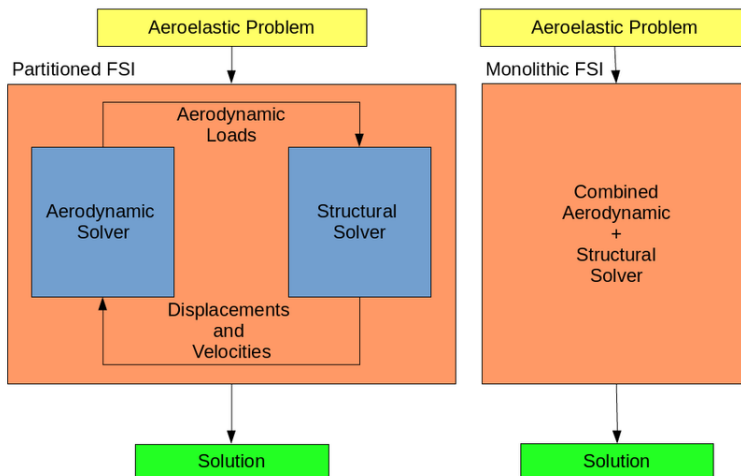


Figure 3.14: Monolithic vs Partitioned Scheme[32]

The monolithic method requires the fluid and the structure to be modelled in a single equation of motion. The monolithic method ensures the stability of the solution, however the discretization of both the domains should be closely interlinked and defined well. Typically the monolithic method is applicable in cases where the structure and fluid domains have a 1 to 1 correspondence with respect

to points, cells or elements. This can result in unnecessary refinement and computation due to the number of cells. Typically, FSI problems require the fluid domain to be a more refined discretization as compared to the structure domain. The majorly linear behaviour of structure for small displacements and motion allows a more simplified and coarsely discretized domain model to be used, with reasonable accuracy.

Partitioned methods enable the flexibility to utilize multiple solvers for the respective domains. It also allows the use of multiple discretization schemes and sizes for each of the domains. The major drawback is the requirement for interpolation methods to transfer information between the 2 domains. The interpolation methods will introduce numerical errors into the solution. The extent and size of these interpolation methods can be regulated based on the method of coupling these solvers:

1. Loosely Coupled
2. Strongly Coupled

The error can be reduced by multiple sub-iterations for each time step till the error balances or reduces based on a chosen criteria. This method is known as *strongly coupled*. It will require the solution that is meant for a future timestep to be sent back to the previous time step and re-calculated in order to check if the error either remains the same or reduces. A visual scheme of a strongly coupled can be seen in Figure 3.15.

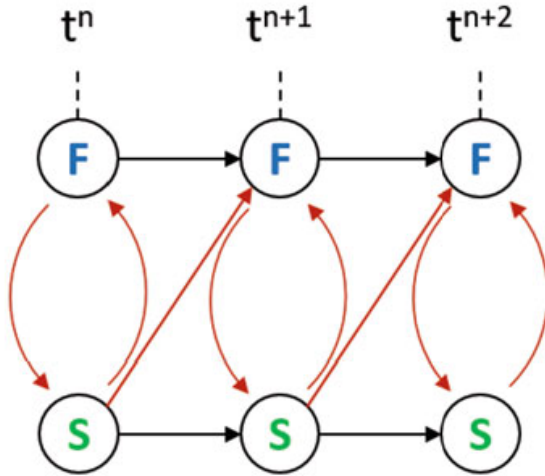


Figure 3.15: Strong Coupling Scheme [33]

A loosely coupled scheme skips the back propagation of the solution at each time step and directly sends the obtained solution at time step t^n to t^{n+1} as seen in Figure 3.16.

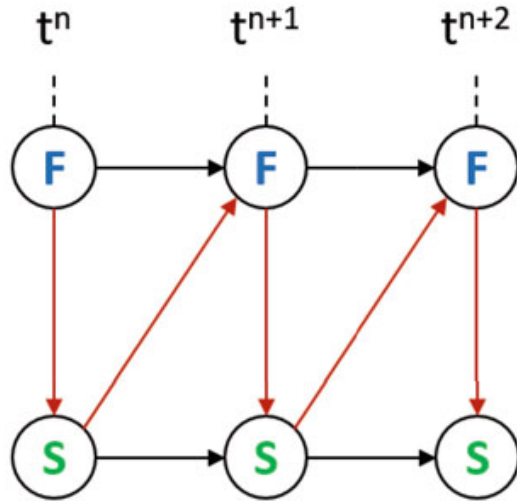


Figure 3.16: Weak Coupling Scheme [33]

The type of coupling scheme depends on the case to be simulated. Factors such as extent of structure displacement, regime of flow, material properties of the fluid and structure will be considered in the determination of the type of scheme for this thesis.

Coupling Conditions

At the interface of the structure and fluid domains, 2 important boundary conditions should be satisfied:

1. Kinematic Coupling Condition
2. Traction Coupling Condition

The kinematic coupling condition at the interface governs the motion/velocity conservation across the 2 domains. This is maintained by equating the flow velocity to be the time derivative of the displacement of the structure [34].

$$u_i = \frac{ds_i}{dt} = \dot{s}_i \quad (3.12)$$

The traction coupling refers to the stress balance or normal force balance over the interface of the fluid and structure. The traction of the fluid and structure respectively should balance out to 0 with the appropriate normal vectors for the 2 domains [34].

$$\begin{aligned} f_i^f &= -pm_i^f + \tau_{ij}n_j^f \\ f_i^s &= \sigma_{ij}n_j^s \\ f_i^s + f_i^f &= 0 \end{aligned} \quad (3.13)$$

In the transonic domain, the inherent non linear fluid mechanics as discussed before, results in a so called non linear transient aeroelastic problem. A nonlinear transient aeroelastic problem where the fluid domain boundaries undergo a motion with a large amplitude can be formulated as a three-field problem: the fluid, the structure, and the dynamic mesh.

For this thesis, an adapted version of the FSI framework, developed by Pinero[29], linking ANSYS Fluent(CFD) and NASTRAN(FEA) is utilized, which has been modified to include the presence and actuation of the minitabs.

3.4.1. Static FSI Algorithm

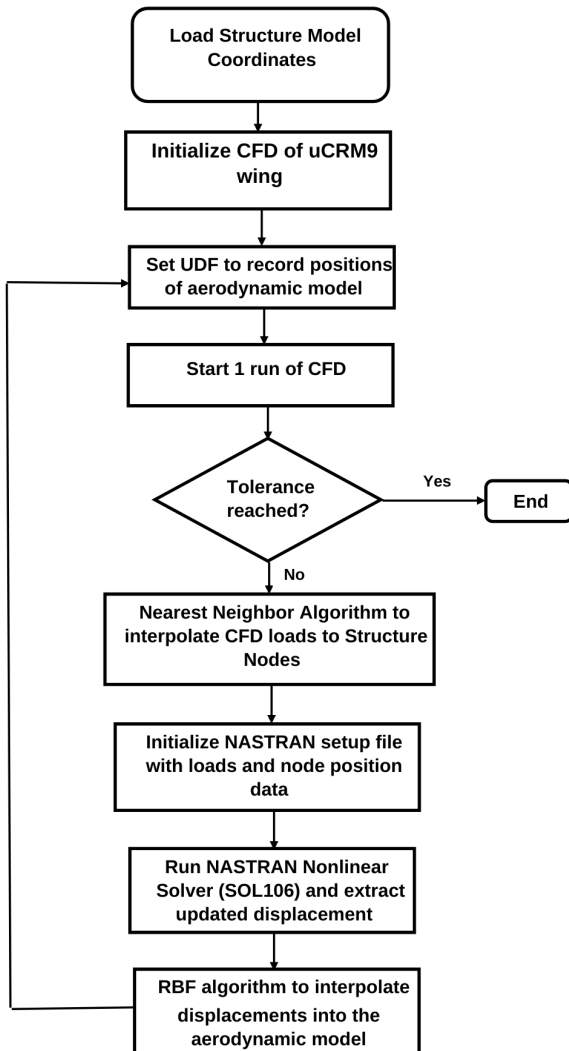


Figure 3.17: Static FSI Flowchart

Static FSI algorithm is run once with the clean wing and the other with the minitab wing in order to obtain the steady state loads and wing geometry for comparison.

3.4.2. Dynamic FSI Algorithm

A systematic flowchart of the FSI framework and modifications made to include the minitab deployment is shown in Figure 3.18.

In order to include the mid flight deployment of the minitab, certain modifications to the FSI framework code had to be made to simulate actuation of the minitab. A sudden inclusion of the minitab into a clean transonic simulation results in instability in the simulation and eventually diverges. The key reason for its instability is the "no-slip" setting for a wall boundary condition in Fluent. The sudden deceleration of the flow on the minitab surface is difficult for the CFD solver to model, even with small

physical time step sizes.

In order to stabilize the simulation at the point of deployment, the minitab surface is converted into wall, with a free slip condition. Free Slip walls slows the flow normal to the surface to 0, but flow tangential to the surface is free, with no boundary layer formed.

This "free-slip" boundary condition was set to run for 1 time-step, to allow the flow to develop around the minitab, slipping past the minitab and not develop any boundary layer. After convergence of the CFD and FSI solution, the minitab surface is changed to a "no-slip" wall. The previous free slip wall allows the change to the no slip wall to be less abrupt, and with the help of under relaxation factors, the solution continue to iterate without any stability issues. The whole process is reversed to simulate the "**Stow Minitab**" operation.

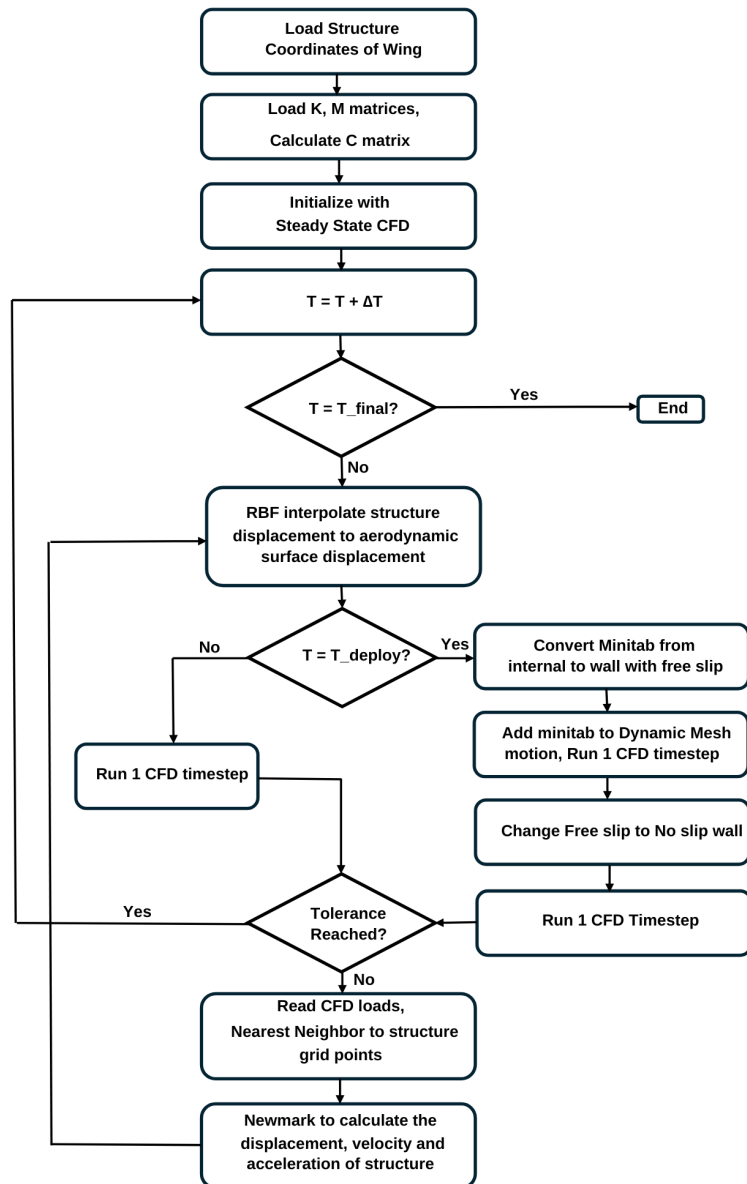


Figure 3.18: Dynamic FSI Flowchart for Minitab Deployment

4

Static FSI Results for Minitab Wing

This chapter will show the results of the static FSI for the CRM wing in the Clean and Minitab configurations.

The purpose of conducting static FSI simulation of the clean and minitab configurations is to determine the differences in the aerodynamic loads, pressure distribution and the deformations of the wing structure. These results will be used to baseline and validate the dynamic FSI results. A key point to note here is that the complete wingbox model is used as the structural model for the FSI simulation as seen in Figure 3.12. Later on, the dynamic FSI case will simplify the wingbox model into a reduced multi node beam model.

4.1. Comparative Analysis of Clean and Minitab Wing

Boundary Conditions of the computational domain were set in accordance to typical cruise conditions for a passenger aircraft. Details regarding the type of boundary condition and values can be seen in Table 3.2. The two wing configurations were initialized at a cruising altitude of 11000m. Using the Altitude-temperature correlation and a constant temperature of 215K (-58°C), air density of 0.35kg/m^3 and a velocity of 249.75m/s which corresponds to a mach number ($M=0.85$) are set as the initial boundary conditions.

The simulations are carried out on both wing configurations in order to compare the effect of the minitabs, considering the aeroelastic behaviour on the lift coefficient and displacement of the wing tip with respect to the *jig shape*.

Table 4.1: Static FSI Results

Wing Configuration	Lift Coefficient (CL)	Drag Coefficient (CD)	Tip Displacement
Clean Wing	0.389	0.017	1288.68mm
Minitab Wing	0.364	0.021	1161.97mm

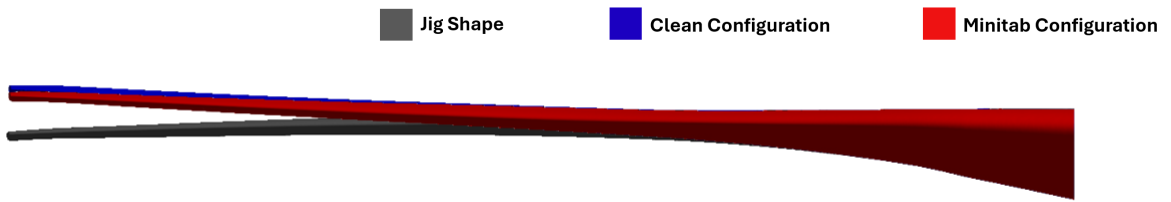
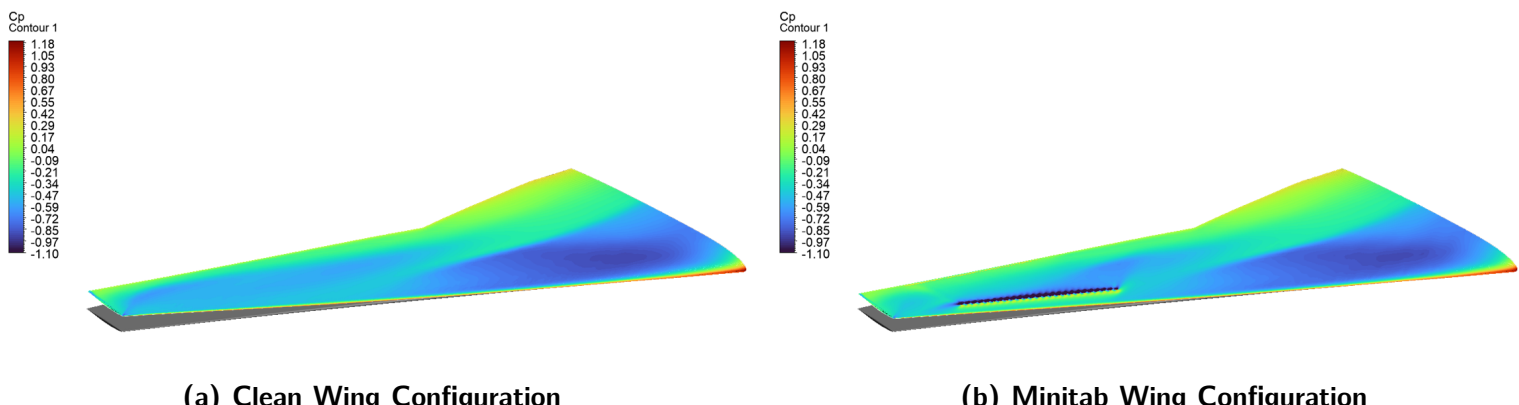


Figure 4.1: Model Wing Shapes at Steady State

As detailed in Table 4.1, the clean wing configuration produces a lift coefficient of 0.389 and a drag coefficient of 0.017. In comparison, the minitab wing configuration exhibits a reduced lift coefficient of 0.364 (6.42% reduction) and an increased drag coefficient of 0.021 (23.52% increase).

From the *jig shape*, the clean wing configuration exhibits an upward deflection as a result of the lift distribution generated by the wing surface along the span. For the clean wing configuration, the wing tip rises 1288.68mm from the *jig shape*. In contrast, the minitab wing configuration shows a reduced upward deflection beyond 50% of the wing span and a wing tip deflection of 1161.97mm from the *jig shape*, which is 9.8% lower than the clean wing configuration.



(a) Clean Wing Configuration

(b) Minitab Wing Configuration

Comparing the clean wing and the minitab wing pressure coefficient contours, the minitab creates a large pressure buildup on the front face followed by a region of low pressure separated flow behind it. This localized pressure differential directly contributes to the increased drag coefficient in comparison to the clean wing configuration from 0.017 to 0.021. It is important to note, the minitab's zone of influence is limited between 60-95% span of the wing and no other significant changes in the pressure distribution over the wing can be seen outside this zone.

5

Transient Simulation Plan for Minitab Wing

5.1. Methodology

A complete schematic of the FSI and CFD simulations carried out is shown in Figure 5.1. The simulations are setup first to build a base foundation with the transient aerodynamic characteristics of the minitabs, which is then followed up with the inclusion of wing flexibility in order to determine how the aeroelastic characteristics affect the performance of the minitabs.

Simulation Type	Wing Structure Type	Wing Shape	Gust	Wing Model		Purpose and Description
				Clean Wing	Minitab Wing	
CFD Transient	Rigid	Cruise Shape	✗	✗	✓	Capture pure transient aerodynamic effects of the minitabs
FSI Dynamic (Gust OFF)	Flexible	Jig Shape	✗	✓	✓	Deploying and stowing of Minitab with no gust. Compare results with baseline clean wing solution.
FSI Dynamic (Gust ON)	Flexible	Jig Shape	✓	✓	✓	Sensitivity study for deploying and stowing time, obtain a final Deploy + Stow time scheme for a gust.

Figure 5.1: Simulation Run Plan for Dynamic FSI of Minitabs

5.1.1. Case: CFD Transient

This CFD case is simulated with the transient mode enabled, which captures time dependent flow phenomena and the wing internal structure set as rigid. This set of results will provide information on the transient aerodynamic effects of the minitabs deployment of the wing alone, with no influence of the structural motion. Aerodynamic data from this case will be utilized in the dynamic FSI simulations in order to identify the sections of the wing's responses which is dominated by the aerodynamics of the deployment alone.

5.1.2. Case: FSI Dynamic (Gust OFF)

The first case of dynamic FSI simulations are conducted to evaluate the aeroelastic effects due to the deployment of the minitabs on the wing structure. These simulations are conducted with the gust input turned "OFF" in order to isolate the aeroelastic effects of the minitab deployment from excitations induced by the gust. In addition, the final wing position, shape and load distribution over the wing span are evaluated once the simulation reaches steady state.

An example representative timeline of a minitab deployment is shown in Figure 5.2. CL_1 represents the lift coefficient of the clean wing, CL_2 represents the lift coefficient of the wing with the minitab deployed.

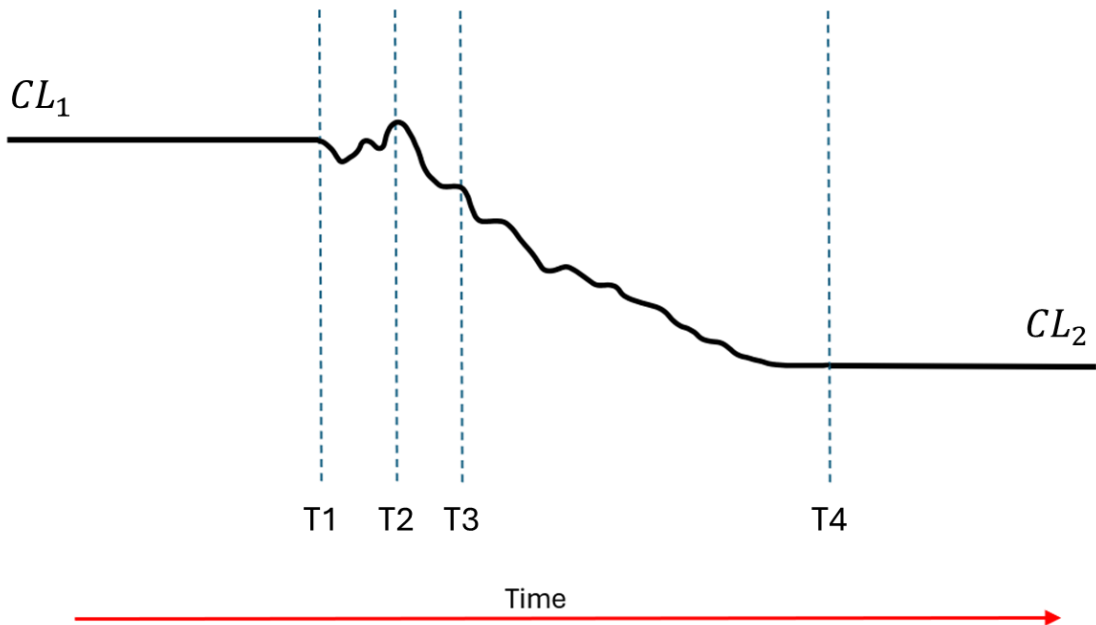


Figure 5.2: Timeline of the lift coefficient variation due to deployment of the minitabs

From Figure 5.2, 4 key points in the timeline are noted: T1 is the point when the minitabs are deployed, T2 is the point at which the peak of the gust reaches the wing, T3 is the point of conclusion of high-frequency transient phenomena in both fluid and structural responses and finally, T4 is the point at which steady state is attained following minitab deployment.

Data from this simulation is focused on capturing the transient flow characteristics and timescales during the deployment phase of the minitabs, particularly between points T1 and T3 in the timeline, with the gust disabled. Data generated for points T4 and beyond in the timeline will also show the final load distribution over the wing span, wing shape.

The midflight deployment of the minitabs during cruise conditions in absence of gusts will yield 4 important sets of data. These comprise of the transient aeroelastic deformation of the wing; the time varying load distribution over the wing surface; the transient flow characteristics, including shock formations and local flow separations during the minitab deployment period and the temporal scales of the minitabs' influence on both wing structure and the surrounding airflow.

This case will be repeated for the "**Stow Minitab**" operation as well. Similar to the minitab deployment process, the purpose of this simulation is to determine the isolated transient aeroelastic behaviour in

terms of the aerodynamics loads and structural deformations of the wing as a result of the minitab stowing.

5.1.3. Case: FSI Dynamic (Gust ON)

Once the isolated aeroelastic behaviors as a result of the minitabs deploying and stowing are determined, the next step is to introduce a discrete gust into the flow. In order to determine the influence of the minitabs in response to a gust, two sets of dynamic FSI simulations with the gust enabled are conducted: first with the clean wing configuration and the second set of simulations are with the minitab wing configuration.

The first set of results simulates the clean wing configuration subjected to various gust cases, in order to obtain a baseline of the expected aeroelastic responses in terms of magnitude and time of peak gust loads, duration of its influence and the motion of the wing structure.

Figure 5.3 illustrates a representative timeline of the lift coefficient variation for a clean wing encountering a discrete gust. In this timeline, T1 denotes the gust onset, defined as the point at which the discrete gust is at the leading edge of the wing root, and T2 is defined as the earliest point, steady state conditions is reached after the gust encounter.

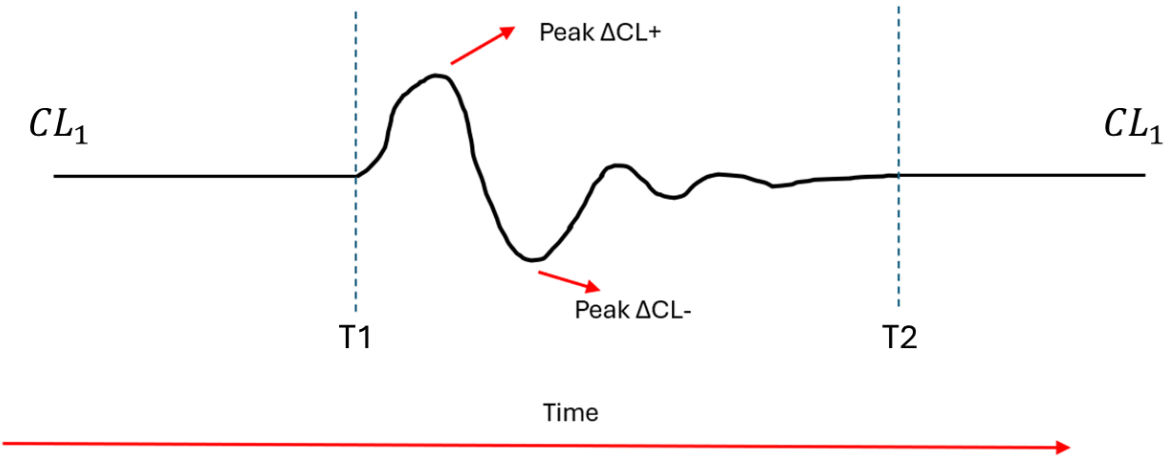


Figure 5.3: Lift Coefficient Timeline with Gust

The second set of results simulates the minitab wing configuration for the same gust cases as the clean configuration. In response to the gust, a sweep of deployment and stowing times is simulated in order to determine the appropriate times to deploy and stow the minitabs to maximize the alleviation of the peak gust loads and minimize any undesirable affects as a result of the deployment and stowing process.

A representative timeline of the variation of lift coefficient of the minitab wing configuration with the ideal deployment and stowing time in response to a discrete gust is shown in Figure 5.4.

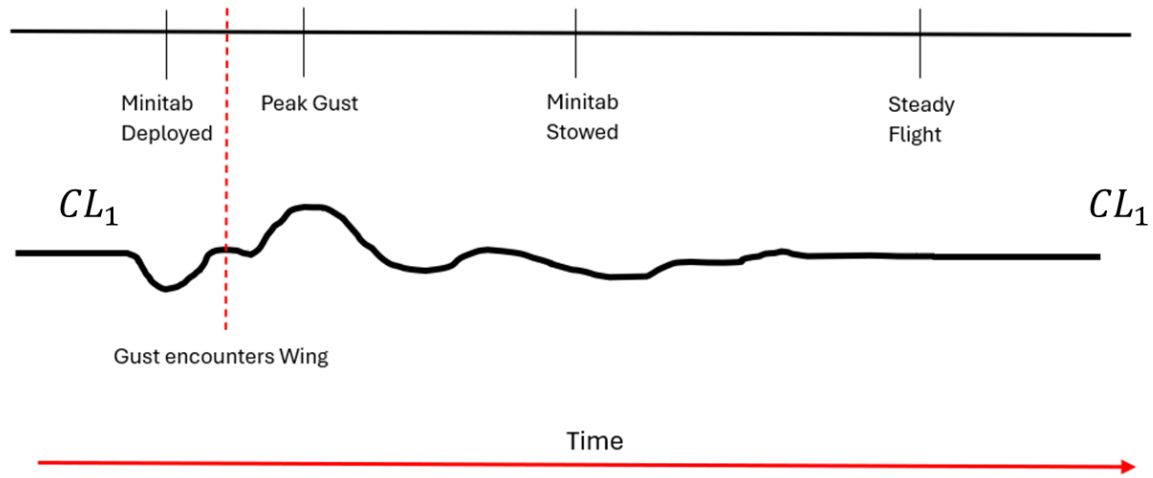


Figure 5.4: Complete Timeline of Minitab Deployment for GLA

6

Final Results of CFD and FSI simulations

This chapter will cover the complete set of CFD and dynamic FSI results of the CRM wing in both clean and minitab configurations. The chapter starts with the transient CFD results of the minitab deployment, followed by FSI results of the minitab deployment and stowing. The final section combines all the previous results to determine a suitable strategy to maximize the load alleviation in response to a discrete gust.

6.1. Transient CFD Results

Transient CFD simulations are conducted to capture the variation in aerodynamic data in terms of the lift forces as a result of the minitab deployment. For this case, the wing structure is set rigid in cruise shape. The minitab deployment operation is simulated under the boundary conditions as stated in Table 3.2. The deployment of the minitab takes place 0.2s from the start of the timeline. From Figure 6.1, the lift coefficient drops sharply after deployment to the peak minima $CL = 0.345$ in 0.2s, and finally settles to a steady state value of $CL = 0.349$.

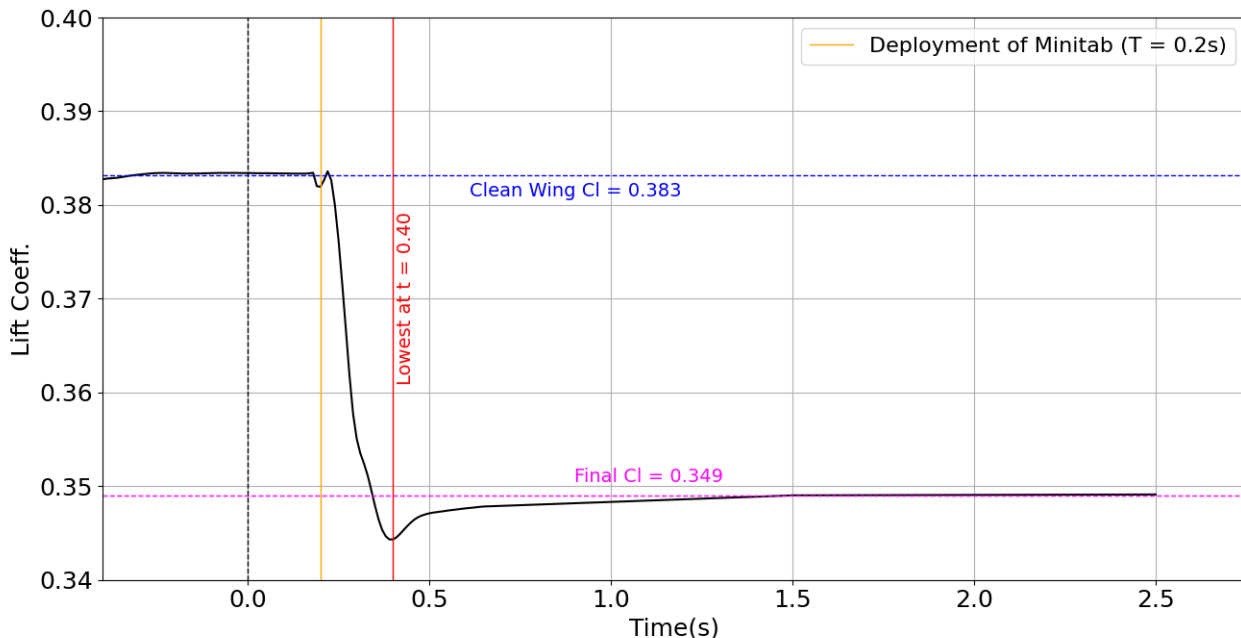


Figure 6.1: Time-dependent variation of lift coefficient during minitab deployment: CFD

At the time of deployment of the minitabs, a region of separated flow forms behind the minitabs. This region of separated flow disrupts the smooth airflow over the upper surface of the wing. Concurrently the minitabs also generate a significant pressure buildup on the front face, leading to an overall rise in pressure over the upper surface. The combination of disrupted flow downstream of the minitabs and the reduced pressure differential between the upper and lower wing surfaces ultimately results in a decreased net lift force.

6.2. Minitab Deployment Midflight with No Gust (FSI)

The first case simulated is the midflight deployment of the minitabs with no gust input. The deployment occurs once the dynamic FSI stabilizes in both lift coefficient and tip displacement. All the graphs start at a reference time ($t = 0$) at which steady state of the clean wing is reached. The minitab deployment was initiated at a physical time of 0.2s after steady state for the clean wing was reached. It is important to note, that the minitab is deployed and stays deployed till the end of the simulation.

6.2.1. Variation of Lift Coefficient with Time (Minitab Deployment)

From Figure 6.2, there is an immediate small drop in lift coefficient, followed by a local increase in lift coefficient in 0.04s from the baseline $CL = 0.383$ to 0.386 . There is followed by a sharp drop in CL to a local minimum $CL = 0.362$ at 0.4s, which is 5.4% lower compared to the steady state lift coefficient of the clean configuration. Once the local minimum peak is reached, the amplitude of the oscillations in the lift coefficient decays to a steady state equilibrium of $CL = 0.37$.

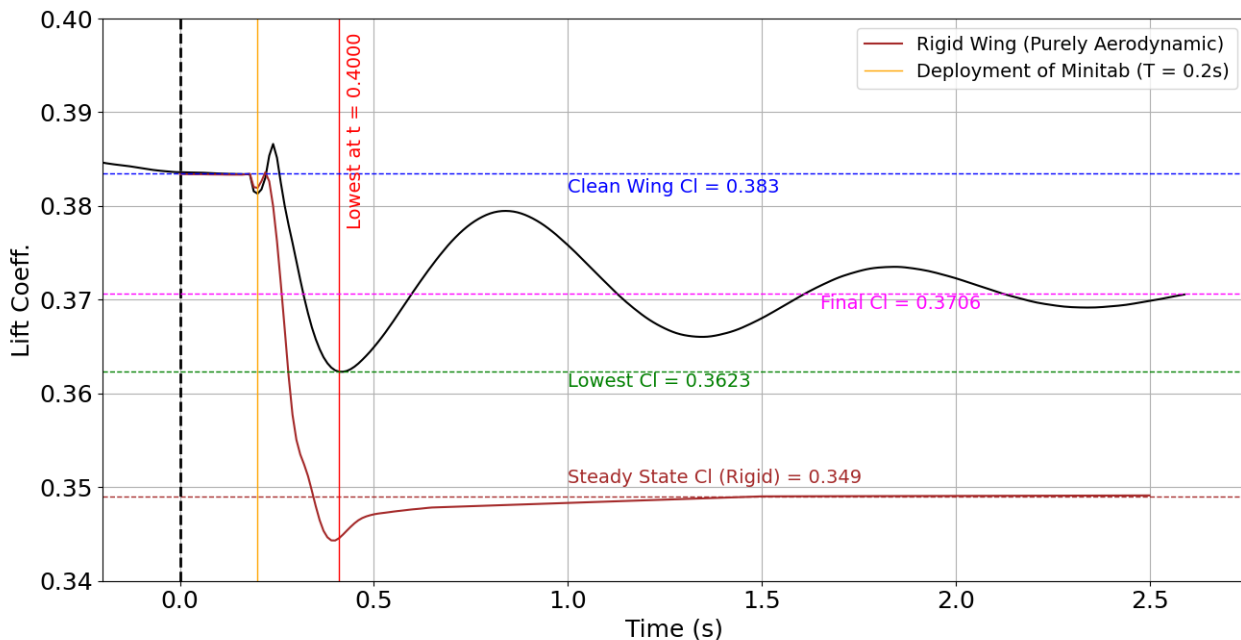


Figure 6.2: Time-dependent variation of lift coefficient during minitab deployment: FSI

The variation in lift coefficient can be split into 2 sections: variation due to the aerodynamic influence of the minitab deployment and variation due to the motion of the wing as a result of the minitab deployment. When evaluating the minitab configuration in relation to the rigid wing, there is a notable similarity in the rapid lift reduction between the time of deployment of minitabs at 0.2s and 0.4s. This

similarity suggests that the variation in the lift coefficient of the minitab configuration between the time frame of 0.2s-0.4s can be primarily attributed to the aerodynamic effects of the minitab itself.

The rapid lift reduction during this interval is characterized as "Reaction Time," denoted by the symbol T_{rea} , with a duration of 0.2 seconds. This time frame captures the immediate response of the aerodynamic forces following the minitab deployment.

Upon comparing the flexible minitab configuration and the rigid wing, the steady state lift coefficient of the rigid wing differs by 5.67%. Since the minitab configuration has a flexible structural model, the wing structure deforms and adjusts its shape to a lower upward deflection in comparison to the rigid wing. For a swept wing, a lower upward deflection increases the effective angle of attack across the wing span, resulting in higher net lift generated.

6.2.2. Variation of Wing Tip Displacement with Time (Minitab Deployment)

From Figure 6.3, although the deployment of the minitab occurs at 0.2s in the timeline, there is no immediate response in the tip displacement. The wing tip begins to drop 0.15s after the minitab deployment and eventually reaches a local minimum of 1172.08mm with respect to the *jig shape*, occurring 0.65s after deployment, which is a 30.29% decrease from baseline. Once the local minima is passed, the amplitude of the oscillations decays and stabilizes to a final wing tip displacement of 1343.80mm with respect to the *jig shape*.

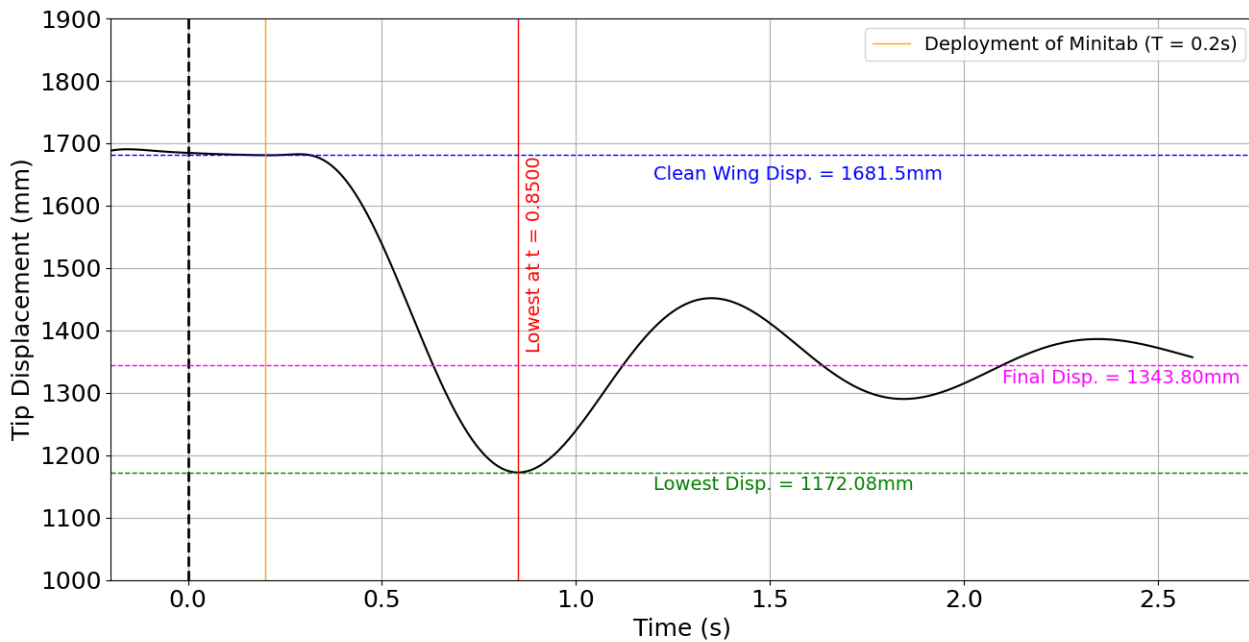


Figure 6.3: Time-dependent variation of wing tip displacement during minitab deployment: FSI

The peak minimum of the lift coefficient occurred earlier than the peak minimum of the structural tip displacement. The oscillations of the wing tip has an approximate frequency of 1Hz. The delayed response in the structural motion as a result of the change in the aerodynamic loads over the wing can be attributed to the wing's significant structural inertia and due to the fact that dynamics of a structure is governed by its eigen modes, primarily dominated by the first bending mode, which is calculated to be 0.82 Hz.

6.2.3. Spanwise Distribution of Lift Forces after Minitab Deployment

The variation of the lift forces at various spanwise locations are illustrated in Figure 6.4. The variation in the load is more pronounced in the wing span where the minitabs are installed (62% - 88% span), while spanwise sections closer to the root of the wing exhibit minimal load variations over time. At spanwise sections of 70% and greater, the load drops sharply within 0.2s after deployment of the minitab, followed by a decaying oscillation until reaching steady state. This load distribution correlates with the trend observed in wing tip displacement.

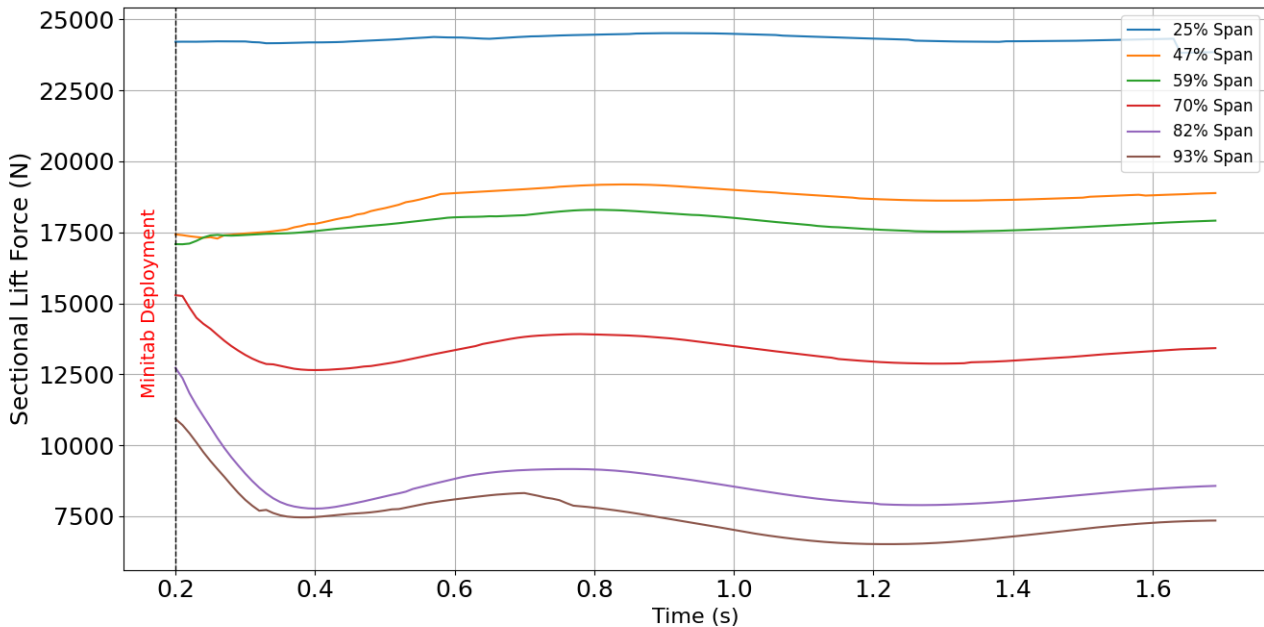


Figure 6.4: Temporal variation of sectional lift forces at multiple spanwise locations

6.2.4. Root Bending and Torsional Moments

In order to determine the internal loads of the wing structure, the root bending moment and torsion moment are plotted in Figure 6.5 and Figure 6.6 respectively.

Upon deployment of the minitabs, the root bending moment follows a similar trend to the lift forces. The wing tip reacts to the changing root bending moment with a delay as a result of the significant structural inertia and dominance of the first bending mode of the wing structure.

In addition, the deployment of the minitab results in an increase in the torsion moment of the wing. Since the minitabs are placed ahead of the wing's elastic axis, close to the leading edge, the additional drag force created as a result of the pressure difference across the minitab induces a positive torsional moment, which results in an increase wing twist angle.

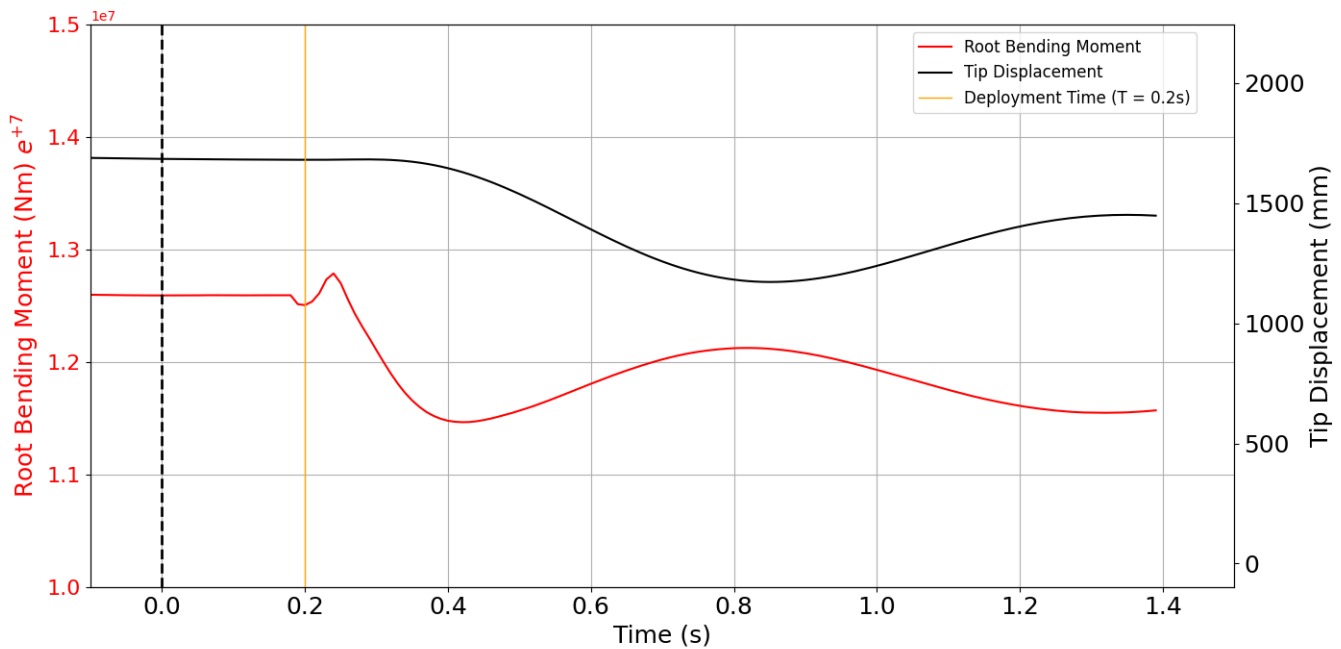


Figure 6.5: Root Bending Moment & Tip Displacement vs Time

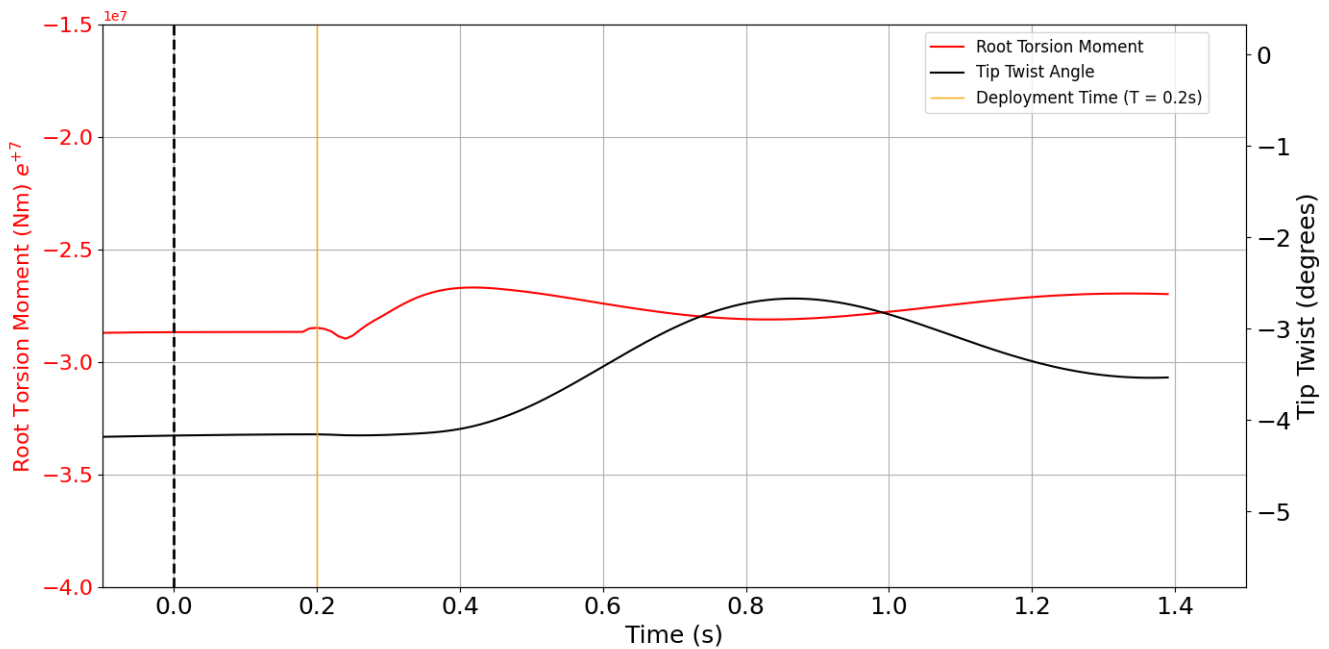


Figure 6.6: Root Torsion Moment & Tip Twist Angle vs Time

6.2.5. Influence of Minitabs on the Pressure Distribution

In order to visualize the changes to the pressure distribution as a result of the deployment of minitabs, contours of the pressure coefficient are plotted over the upper wing surface. The range of pressure coefficient values was limited in order to obtain a better contrast of the contours over the surface of the wing.

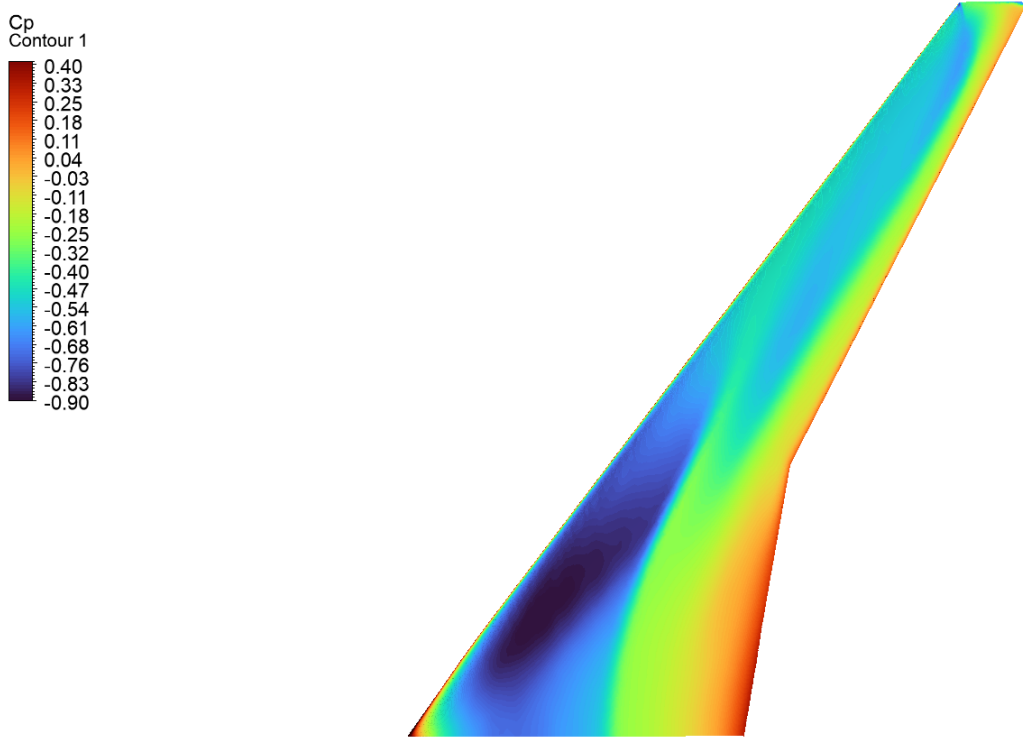


Figure 6.7: Pressure distribution over upper surface for clean configuration

Within a short time frame after deployment of the minitabs (0.04s), a region of high pressure develops in front of each of the minitabs and grows towards the leading edge, seen in Figs. 6.8(b), 6.8(c) and 6.11(a). Directly downstream of the minitab's position, small pockets of separated flow regions form, characterized by significantly lower pressures behind each minitab. These localized regions of separated flow behind each minitab coalesce in 0.04s and stabilizes for the rest of the duration of the minitab deployment.

Analyzing the pressure distribution for the clean configuration as seen in Figure 6.7, it indicates a normal shock located at approximately 80% chord length, parallel to the leading edge of the wing. Upon the minitab deployment and in subsequent time intervals, this normal shock over the outboard span of the wing loses its strength, while an oblique shock forms at the upper edges of the minitabs. As illustrated in Figs. 6.8(d) to 6.8(f), the pressure increases closer to the outboard minitabs, while the inboard minitabs, the pressure gradient is further aft, indicating that the shock is oriented more perpendicular to the freestream direction. This can be explained by the orientation of the minitabs parallel to the wing leading edge. The minitabs are aligned with the natural spanwise flow of a swept wing which enhances the effect on the airflow, particularly on the outboard minitabs. The wing span close to the inboard minitabs still encounter a majoritarian uninterrupted spanwise and mean flow, resulting in marginal change in the position of the shock.

On the reaction time of the minitab is passed, the shock position oscillates marginally in the chordwise

direction with the oscillations of the wing structure, however no major change is noticed.

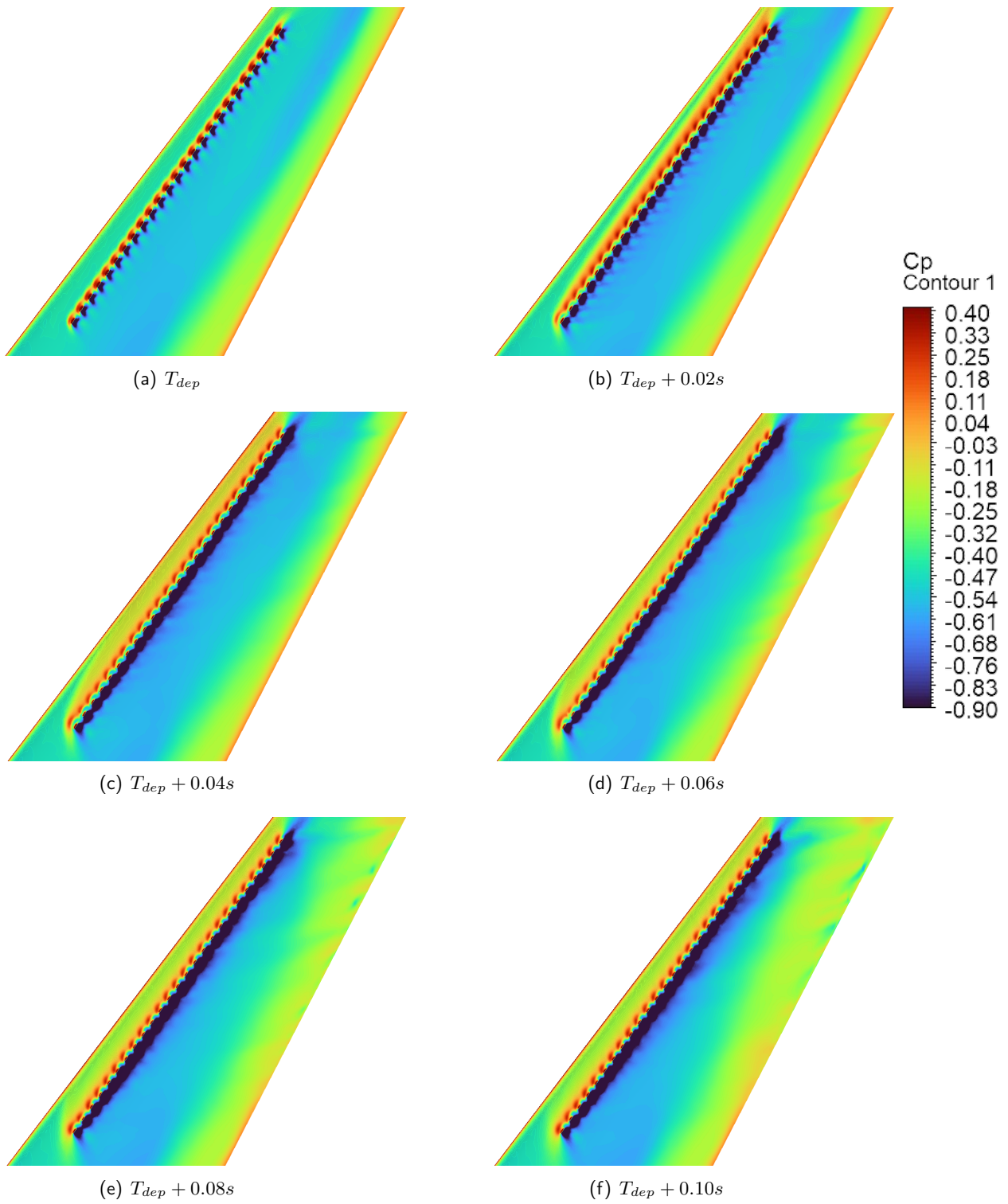


Figure 6.8: Pressure distribution at location of minitab installment

To further analyze the pressure distribution as a result of the minitabs, the sectional pressure coefficient is calculated at 2 spanwise locations. Figure 6.9 is plotted at the section across a minitab (75%

span) and Figure 6.10 is plotted at the section in the gap between 2 minitabs (65% span). When evaluating the difference between the clean and minitab configurations, the decreased lift of the minitab configuration can be attributed to a lower suction peak at the leading edge ahead of the minitabs and the subsequent increased pressure build up on the front face of the minitab.

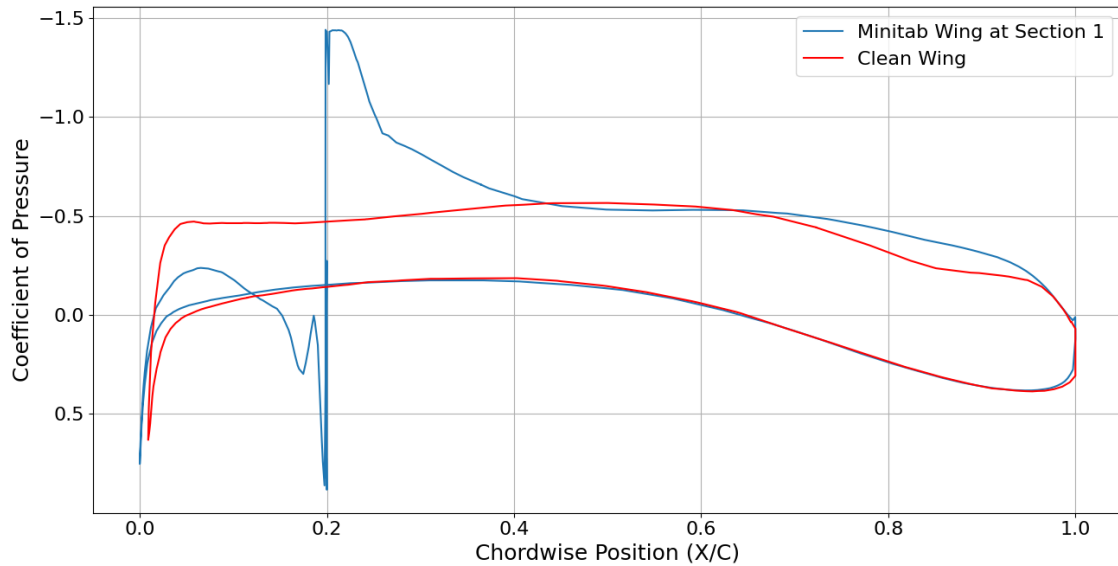


Figure 6.9: Sectional Pressure Coefficient for the clean and minitab configurations: Section 1 (75% Span)

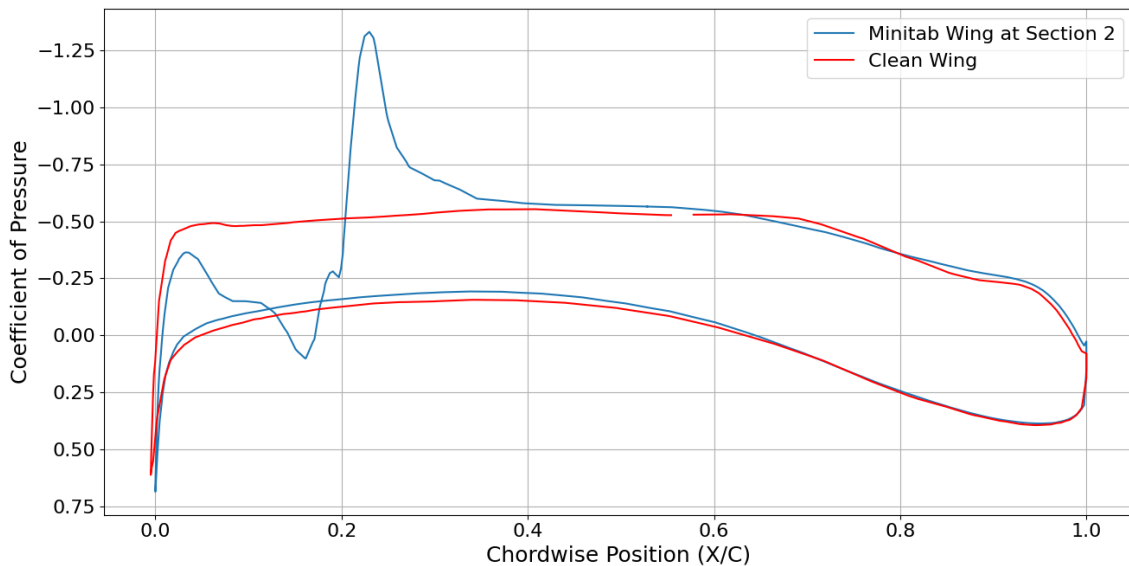


Figure 6.10: Sectional Pressure Coefficient for the clean and minitab configurations: Section 2 (65% Span)

6.2.6. Influence of the minitab on the surface flow characteristics

Analyzing the wall shear stress in the wing span of the minitabs seen in Figure 6.11 gives an indication of the direction of the flow over the surface of the wing. The primary outcome from the wall shear stress is the flow passing through the gaps between consecutive minitabs is forced into the spanwise direction, driven towards the wing tip. Around the regions around the outboard minitabs, this effect is more pronounced, resulting in regions of circulating flow around the minitabs. This result corroborates the enhanced spanwise flow as a result of the minitab's orientation over the wing.

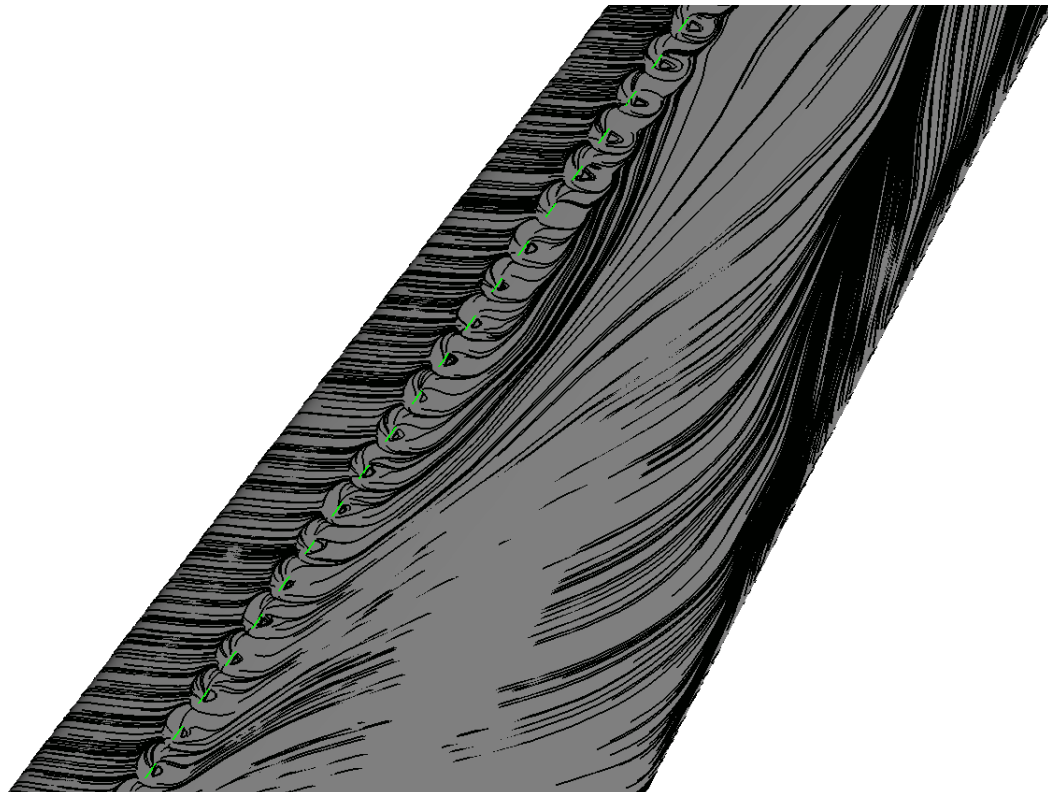


Figure 6.11: Wall Shear Stress streamlines over minitab installment location

6.3. Minitab Stowing Midflight with No Gust (FSI)

The stowing of minitabs is simulated by keeping the minitab deployed from the start till equilibrium state is reached set at $t = 0$. With the minitab deployed, the equilibrium lift coefficient and tip displacement reached was 0.371 and 1340.8mm respectively. The minitab is simulated to be stowed by switching the boundary condition of the minitab from wall to interior flow.

6.3.1. Variation of Lift Coefficient and Tip Displacement with Time (Minitab Stowing)

From Figure 6.12, the minitab is stowed at 0.2s from the start of the timeline. There is a small increase in CL immediately after stow in 0.03s. The CL follows a gradual dip and then begins a sharp rise to a lift coefficient local maxima of 0.394 at 0.5s ($\Delta CL = 5.84\%$). Once this peak is reached, the lift coefficient drops and oscillates in a decaying amplitude towards a steady state value of 0.383, which correlates to the lift coefficient of the clean configuration.

Applying similar reasoning as for the deployment of the minitabs, the initial rapid increase in lift 0.3s after stowing is attributed to the aerodynamic effects of the minitab stowing

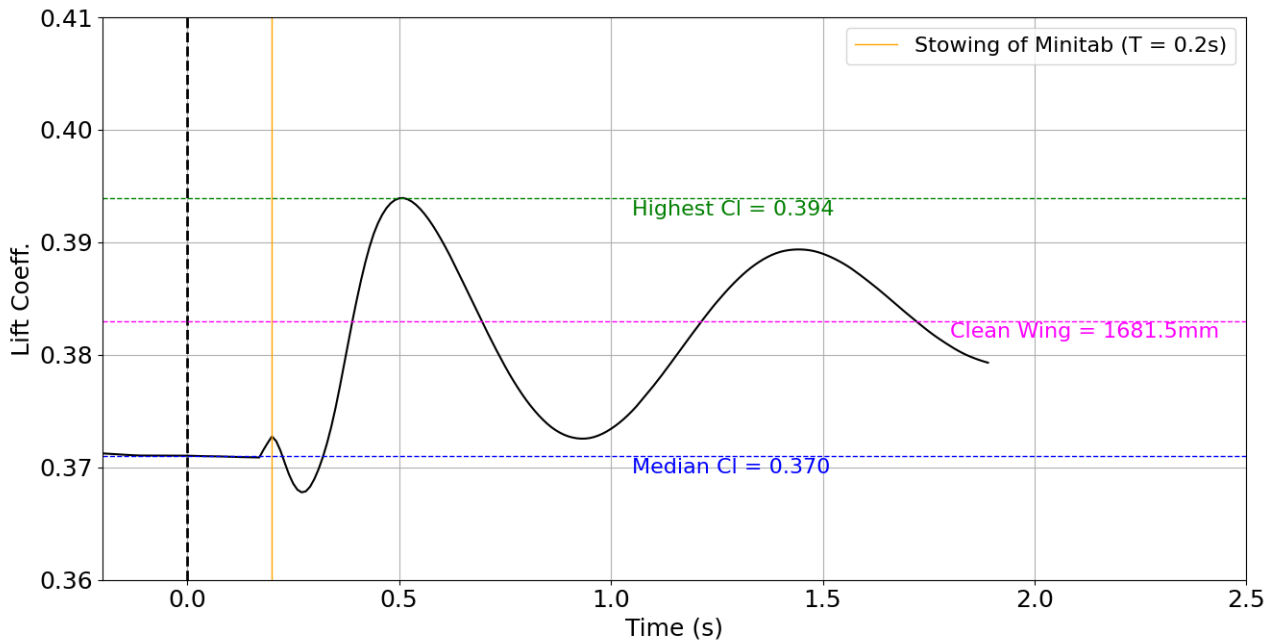


Figure 6.12: Variation of lift coefficient with time for minitab stowing

From Figure 6.13, the wing tip displacement responds with a delay of 0.25s from the time of stowing, resulting in a large wing tip deflection to 1904.04mm, 42% higher from the steady state wing tip displacement prior to stowing the minitabs. Passing this peak, the wing tip oscillates with a decaying amplitude towards a median wing tip displacement of 1681.5mm, corresponding to the clean configuration. Similar to the minitab deployment case, the delay in the response of the wing tip displacement is attributed to the significant structural inertia and dominant low frequency first bending mode of the wing's structure in response to stowing the minitabs.

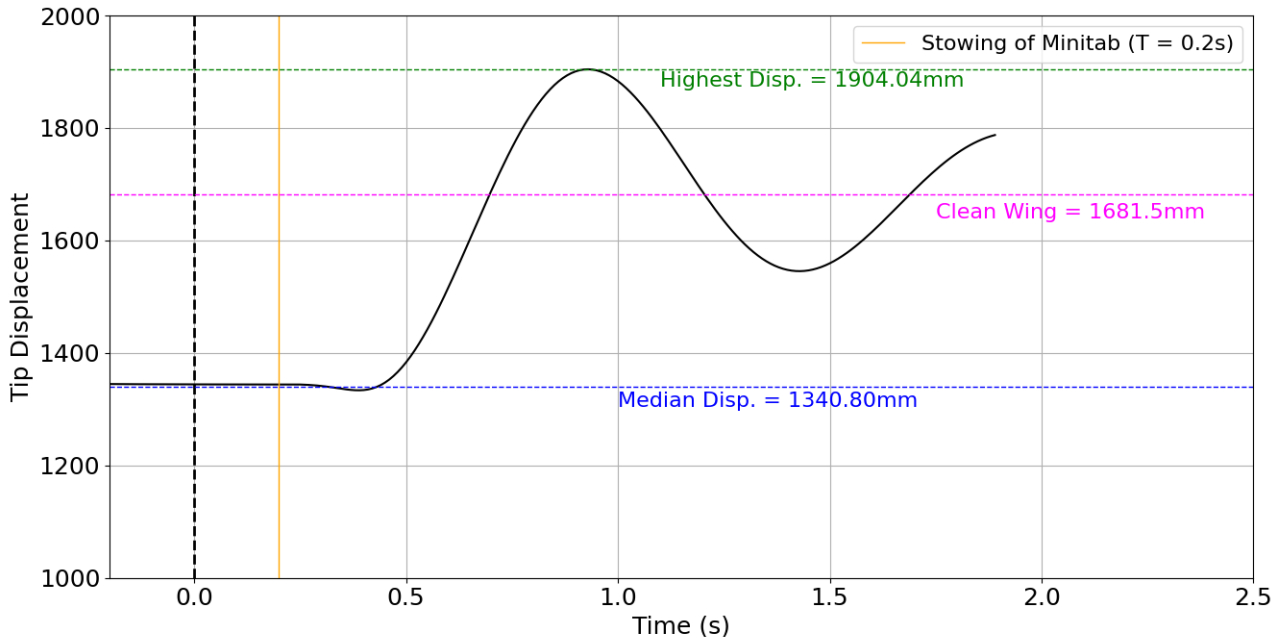


Figure 6.13: Variation of tip displacement with time for minitab stowing

Due to the large, abrupt increase in the wing tip displacement, the stow operation should be considered to be activated in the time period of the tip displacement decrease in the minitab "Deployment" process, seen in Figure 6.3 due to their contradicting behaviour.

6.4. Conclusions from Simulations of Deployment and Stowing of Minitab

Concluding the results from the minitab deployment and stow with no gust input, a key takeaway from the results is the lift forces in the deployment of minitab operation is heavily depending on the structure motion, however the rapid change in the lift forces within 0.2s after deployment and peak minima reached, are predominantly influenced by the aerodynamic effects of the minitabs.

During the deployment of the minitabs, a rapid drop in the lift forces occurs within a time interval of 0.2s from the moment of deployment, also labelled as "*Reaction Time*". Stowing of the minitabs is almost symmetric to the minitab deployment process, with the changes in the loads as a result of the aerodynamic effects of the minitab lasting 0.3s after stowing. Beyond this time period, the motion of the structure dominates the variation of the loads generated.

The structure oscillation after deployment/stowing is at a frequency of approximately 1Hz. Given the previously calculated first bending frequency of 0.82Hz, this matches well with the obtained variation in the tip displacement results. This result indicates that the minitab deployment and stowing predominantly influences the first bending mode of the wing. In addition, the significant structural inertia along with the low frequency first bending mode directly contribute to the delayed and slow response of the wing tip oscillations.

6.5. Clean Configuration with Various Gust Profiles (FSI)

In order to determine the load alleviating capabilities of minitabs, we require baseline data of the responses of a clean wing encountering various gust profiles.

6.5.1. Gust Shape and Amplitude Calculation (EASA CS 25.341)

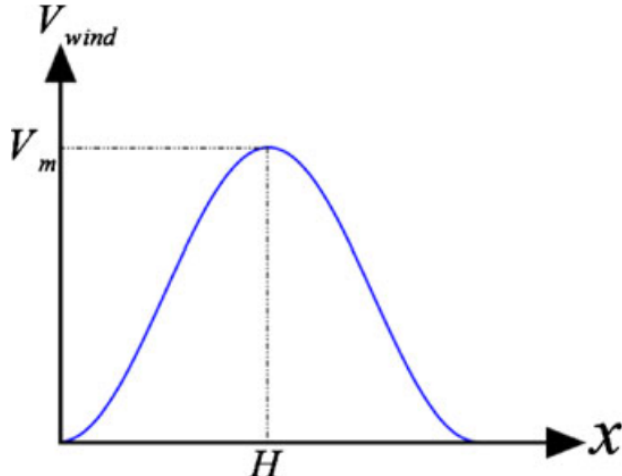


Figure 6.14: 1-cos Gust Profile [35]

Four gust profiles are simulated on the clean configuration, with variations in gust length and gust amplitude. These gusts are modelled as discrete "1-cos" gusts in accordance to the standards set by the EASA certification[5]. The mathematical expression of a discrete "1-cos" gust is defined in Equation 6.1:

$$\begin{aligned} V_m &= \frac{U_{ds}}{2} \left[1 - \cos \frac{\pi s}{H} \right] & 0 \leq s \leq 2H \\ V_m &= 0 & s \geq 2H \end{aligned} \quad (6.1)$$

where U_{ds} is the design gust amplitude, H is the gust length and V_m is the resultant gust velocity in the direction of freestream flow. The design gust amplitude U_{ds} is calculated using Equation 6.2:

$$U_{ds} = U_{ref} \cdot F_g \left[\frac{H}{107} \right]^{1/6} \quad (6.2)$$

where U_{ref} is the reference gust velocity and F_g is the flight profile alleviation factor. At maximum operating altitude, the flight profile alleviation factor is set to a value of 1. Since the clean configuration is simulated at a cruising altitude of 11000m, the value of F_g is approximated as 1.

The reference gust velocity U_{ref} may be reduced linearly from 13.41 m/s EAS at 4572 m to 6.36 m/s EAS at 18288 m . For the cruising altitude of 11000 m, U_{ref} is calculated to be 10.106 m/s. Finally, a set of gust lengths (H) must be chosen between 9 m to 107 m, in order to calculate the final gust amplitudes (V_m) from Equation 6.1. The selected gust lengths and calculated gust amplitudes of the 4 gust cases considered are stated in Table 6.1.

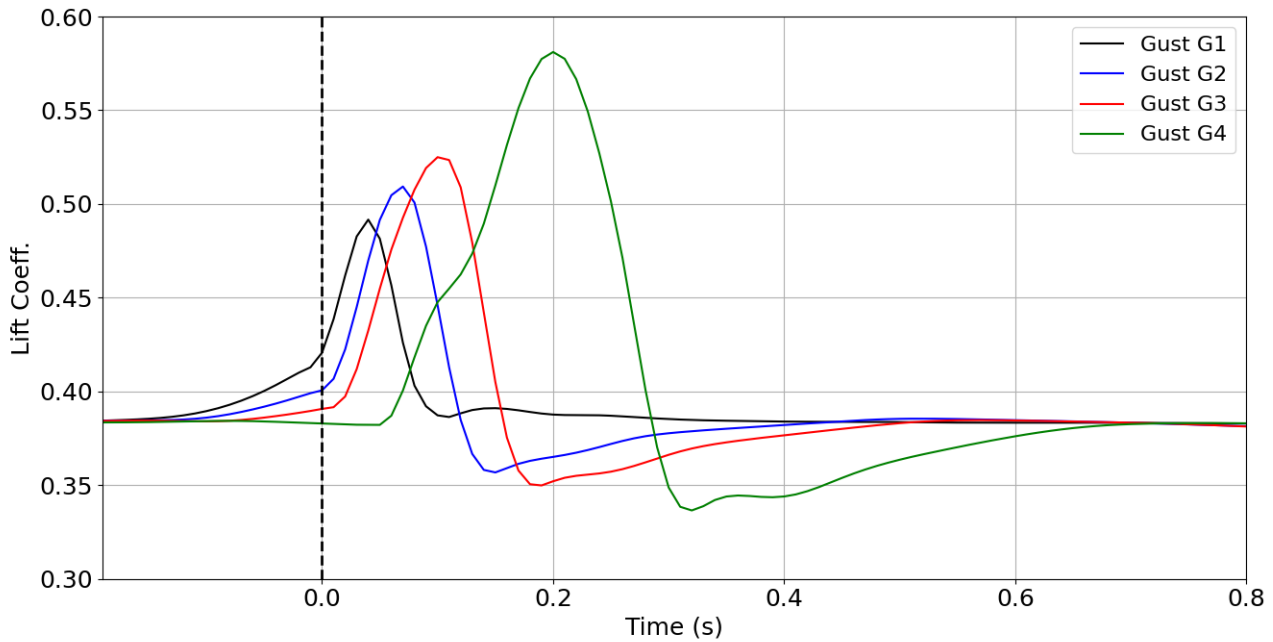
Table 6.1: Gust Profiles

Gust	Gust Amplitude (m/s)	Gust Length/Gradient (m)
G1	6.808	10
G2	7.473	17.5
G3	7.931	25
G4	8.902	50

6.5.2. Peak Lift Coefficient and Recovery Time for Various Gust Profiles

Figure 6.15 plots the variation in the lift coefficient in response to the chosen gust profiles stated in Table 6.1 for the clean configuration.

Plotting the peak lift coefficients reached for each gust case in Figure 6.16 demonstrates that larger gust lengths and subsequent gust amplitudes, the peak lift coefficient reached is higher. The extended duration over which the gust perturbation acts on the wing allowing for a more sustained lift generation process. Additionally, the higher gust amplitude increases the effective airflow velocity for a brief period results in a higher peak lift coefficient.

**Figure 6.15:** Variation of lift coefficient for all gust profiles in clean configuration

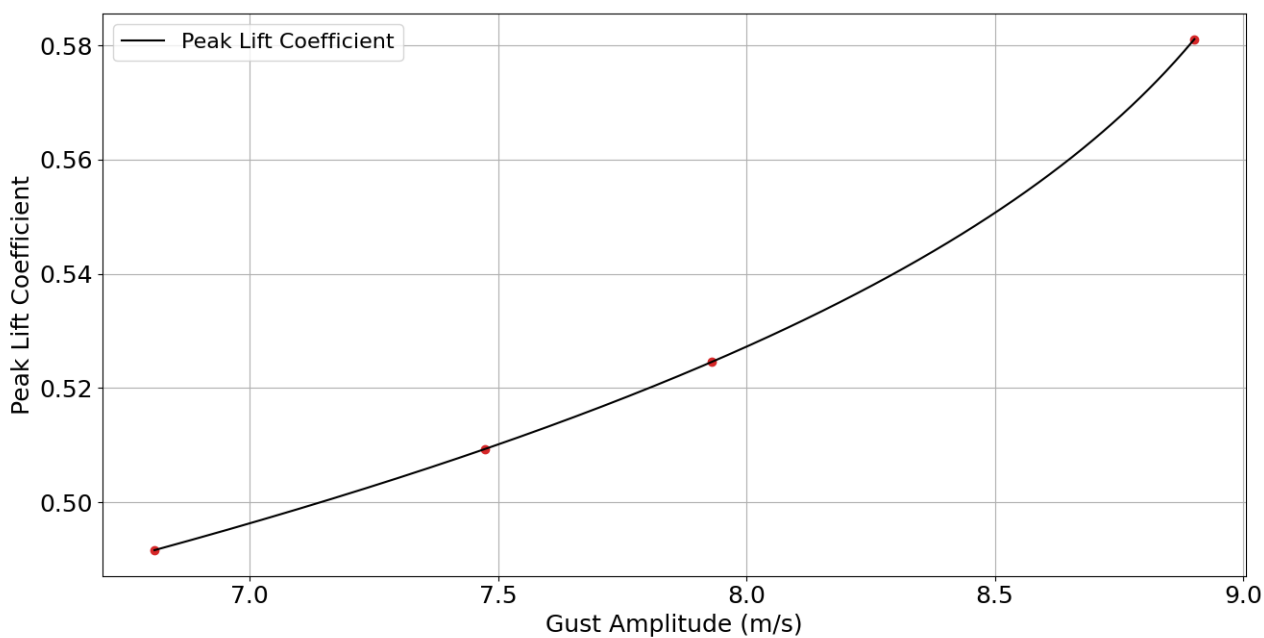


Figure 6.16: Variation of peak lift coefficient with gust length (m)

Although the gust profiles reach the wing's leading edge simultaneously, longer gust lengths distribute the perturbation over an extended duration. This results in a greater recovery time to steady state (T_{Rec}), as illustrated in Figure 6.17.

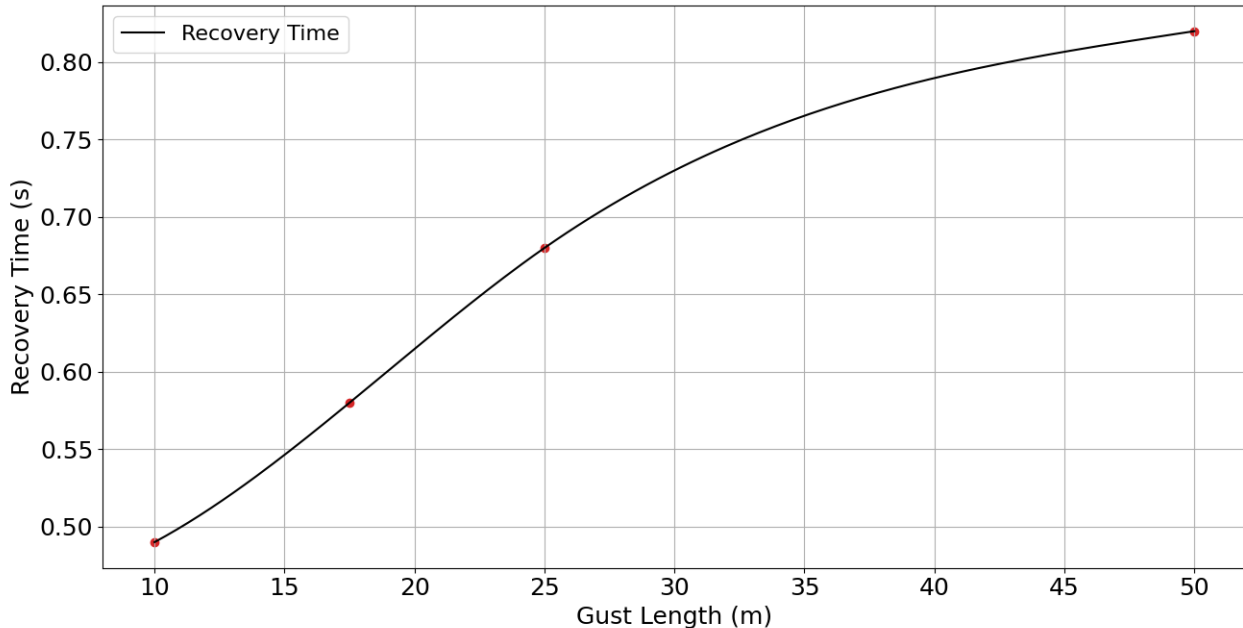


Figure 6.17: Effect of gust length on the recovery time(T_{rec})

6.6. Minitab Deployment Midflight with Gust (FSI)

With the aeroelastic results of the midflight deployment of the minitabs and a reaction time T_{rea} of 0.2s determined, the next step is to include gusts in order to determine the gust load alleviation capability of the minitabs. The minitabs will be deployed at various moments across the gust timeline, to determine an ideal time of deployment to maximize the alleviation of the gust loads.

To standardize the range of deployment times, a non-dimensional parameter known as the Deploy Time Ratio (DTR) will be utilized, evaluated by Equation 6.3. The Deploy Time Ratio (DTR) is defined as the sum of the time taken for minitab deployment (T_{dep}) and the reaction time (T_{rea}), divided by the time required for the gust to traverse its length in the freestream direction. Mathematically, it can be expressed by the Equation 6.3:

$$DTR = \frac{[T_{dep} + T_{rea}]}{\left[\frac{H}{U_\infty}\right]} \quad (6.3)$$

where T_{dep} is time of minitab deployment, T_{rea} is the minitab reaction time, H is the gust length and U_∞ is the freestream velocity. This dimensionless parameter evaluates the relation between the dynamics of the minitabs with the timescales of gust encounters.

For each gust case, 4 deployment times are chosen such that there is always an overlap between the time period of the gust peak perturbation and the minitab's reaction time interval. Since all the gust cases encounter with the wing at the same time, the time of gust onset is set as the starting point of the timeline ($t=0$). It is important to note here that for all the gust cases simulated, the minitab remains deployed even after the gust encounter. In later cases, the minitab will be stowed after the gust passes, hence mitigating this large negative structural displacement.

Gust Profile	Time of Gust Peak	Time of Deployment	DTR
G1	0.04s	-0.36s	-4.00
		-0.26s	-1.50
		-0.16s	1.00
		-0.06s	3.50
G2	0.07s	-0.33s	-1.92
		-0.23s	-0.46
		-0.13s	1.00
		-0.03s	2.46
G3	0.10s	-0.31s	-1.09
		-0.20s	-0.04
		-0.10s	1.00
		0.00s	2.04
G4	0.20s	-0.22s	-0.12
		-0.11s	0.44
		0.00s	1.00
		0.11s	1.56

6.6.1. Gust Case G1: Variation with Deploy Time Ratio (DTR)

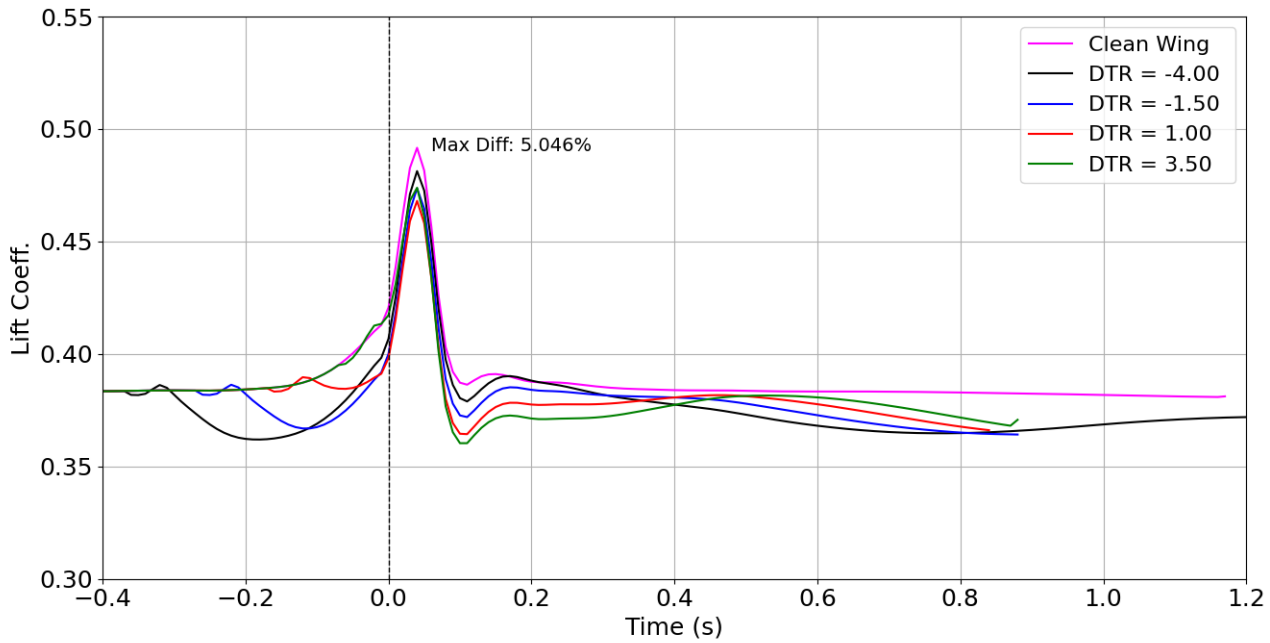


Figure 6.18: Gust G1: Lift coefficient variation for different DTR values

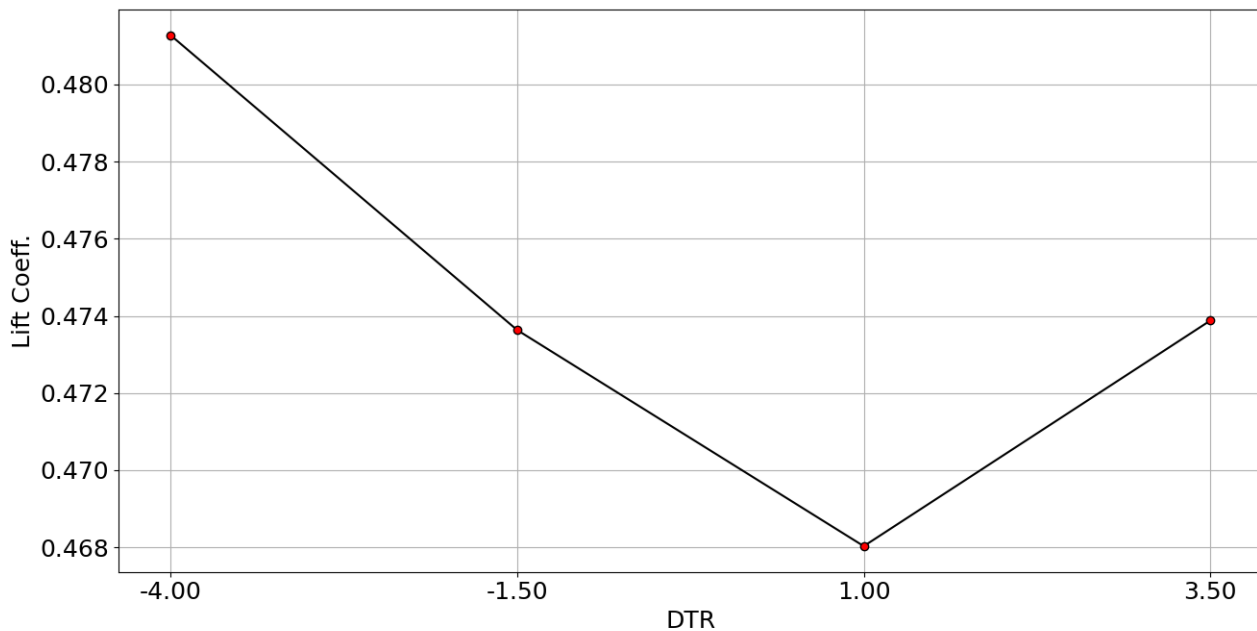


Figure 6.19: Lift Coefficient at Gust Peak (G1) vs DTR Configurations

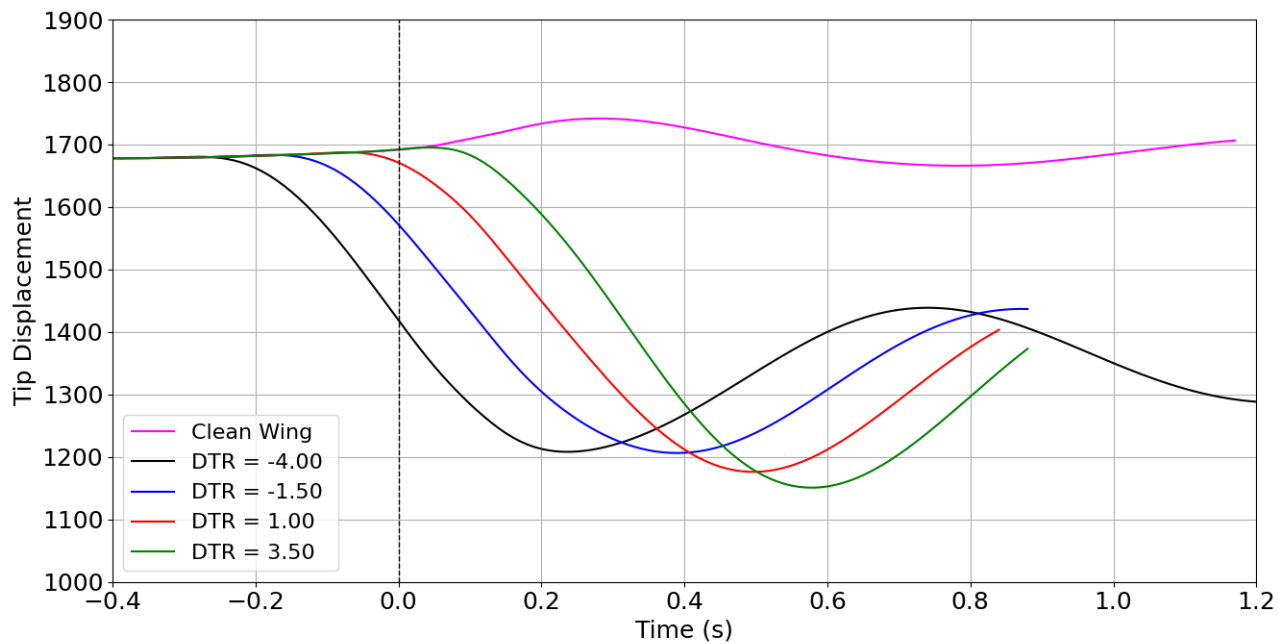


Figure 6.20: Gust G1: Wing tip displacement variation for DTR values

6.6.2. Gust Case G4: Variation with Deploy Time Ratio (DTR)

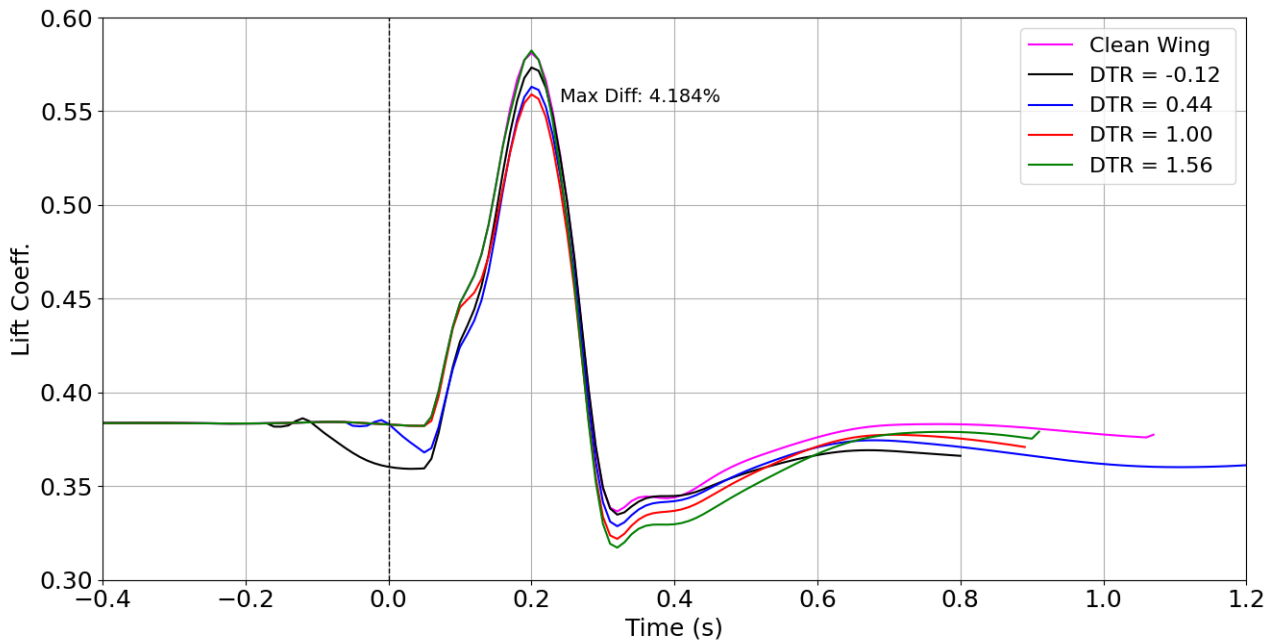


Figure 6.21: Gust G4: Lift coefficient variation for different DTR values

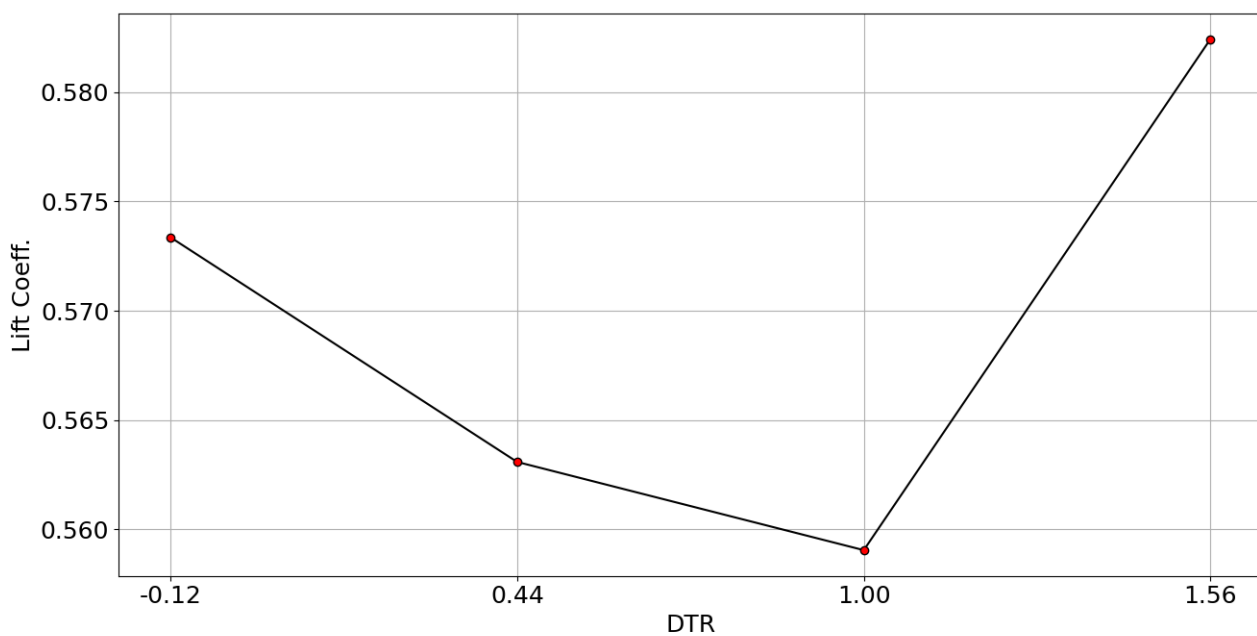


Figure 6.22: Lift Coefficient at Gust Peak (G4) vs DTR Configurations

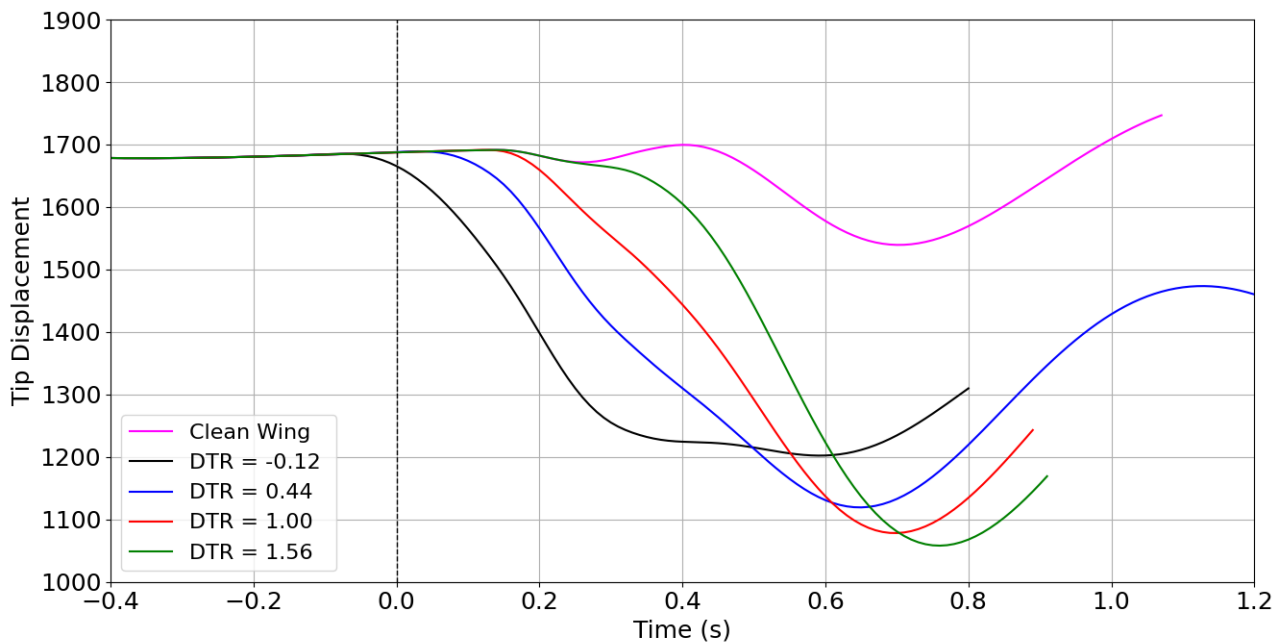


Figure 6.23: Gust G4: Wing tip displacement variation for different DTR values

Note that the results of the gust cases G1 and G4 are shown in this section, and results of gust cases G2 and G3 are plotted in Section A.3.

On average, there is a 5% reduction in the peak lift force as a result of the gust in comparison to the clean configuration. The primary conclusion from all the gust cases is a DTR value of 1.00 produces the maximum reduction in the peak gust load. Since a DTR = 1.00 corresponds to the reaction time of the minitabs lining up with the peak gust time, the combined effect of the minitab's load reduction and the increased load due to the gust, results in maximum load alleviation.

Another major conclusion that can be made is by having an earlier minitab deployment time, which corresponds to a lower DTR value, results in a reduced alleviation ability of the peak gust load. The earlier deployment times also produces a premature reduction in the lift forces which can be explained by the fact that the reaction time of the minitabs is reached before the peak of the gust. Upon comparing the various gust cases, higher load alleviation is seen for gusts of shorter gust lengths

Looking at the tip displacements, the increase in tip displacement due to the sharp gust is completely dominated by the large negative displacement change due to the minitab deployment. For the case of Gust G4, the large gust length results in a long duration for the wing tip to respond to the gust. Since the drop in the wing tip displacement as a result of the deployment of the minitab takes a shorter time in comparison to the response of the gust, the net response results in a reduction of the wingtip for a prolonged duration.

6.6.3. Special Case: Non Standard High Gust Amplitude

In order to assess the alleviating ability of the minitabs for powerful and sharp gusts, a special case of a gust with a large gust amplitude and short length, not adhering to the CS-25 standards was taken and simulated. To maximize the load alleviation, a DTR = 1.00 was also taken for the minitab deployment.

Table 6.2: Gust Profile (G5)

Gust	Gust Amplitude (m/s)	Gust Length/Gradient (m)
G5	11.2	15

From Figure 6.24, it indicates a 9.095% reduction in peak lift due to the minitab deployment, which is nearly double the reduction observed in previous gust cases. Furthermore, the tip displacement variation in Figure 6.25 exhibits a consistent trend, characterized by slow, decaying oscillatory motion which ultimately stabilizes to steady state.

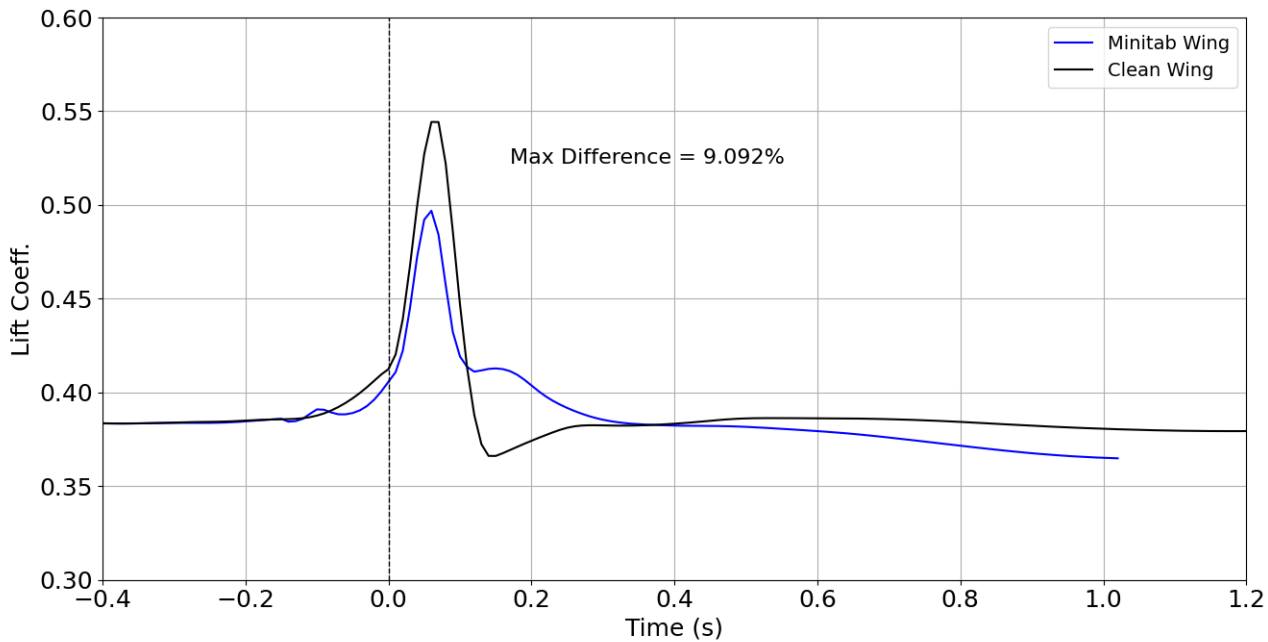


Figure 6.24: Gust G5: Variation in Lift coefficient between the clean and minitab configurations

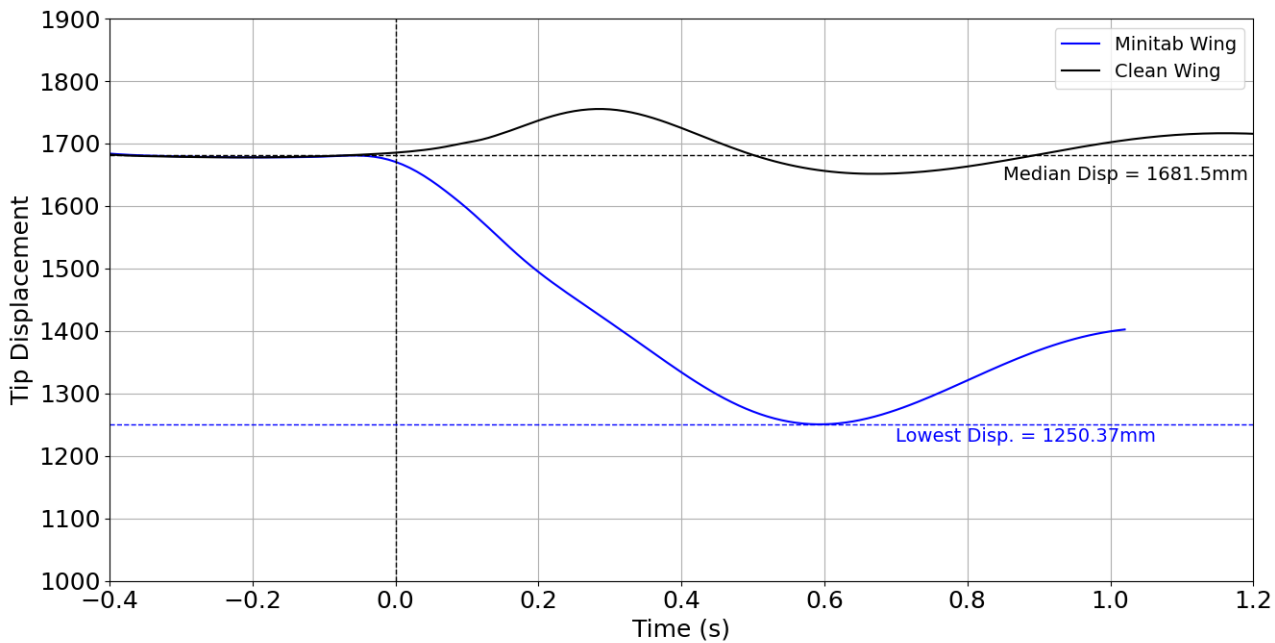


Figure 6.25: Gust G5: Variation in Wing Tip displacement between the clean and minitab configurations

Higher gust amplitudes result in an increased load magnitude across the wing span. The loads concentrated over the outboard span of the wing are alleviated to a greater extent, as the minitabs

facilitate more flow separation in the wake. In combination with the short reaction time of the minitabs, this results in reducing the peak loads experienced by the wing to a greater extent. This case demonstrates that the minitab is more effective in alleviating loads, particularly for shorter-duration, higher-amplitude gusts compared to prolonged gusts with extended recovery times.

6.6.4. Special Case: Gust Frequency matching Structure Oscillatory Frequency (G6)

In the case of minitab deployment with no gust in Section 6.2, the frequency of the oscillatory motion of the structure is approximately 1Hz. A special case of a gust is taken, with effective frequency of the $1-\cos$ gust equal to 1Hz. This case is simulated in order to analyze if any undesirable effects appear in the structure's response when the gust is at the same frequency as the frequency of the wing structure primary motion. The required gust length (H) was determined from Equation 6.4 using the freestream velocity of 250m/s (corresponding to $M = 0.85$ at 11000m altitude) and a gust frequency of 1Hz. This calculation results in a gust length of 125m.

$$f = \frac{U_\infty}{2H} \quad (6.4)$$

Table 6.3: Gust Profile (G6)

Gust	Gust Amplitude (m/s)	Gust Length/Gradient (m)
G6	10.371	125

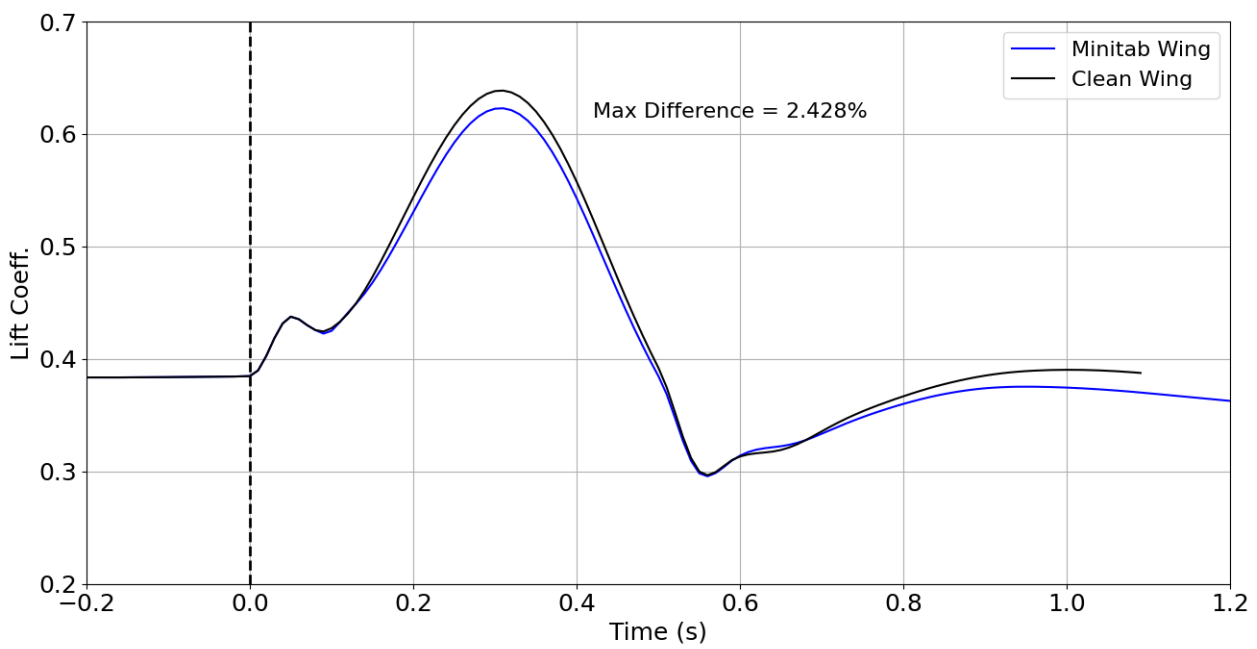


Figure 6.26: Gust G6: Variation in Lift coefficient between the clean and minitab configurations

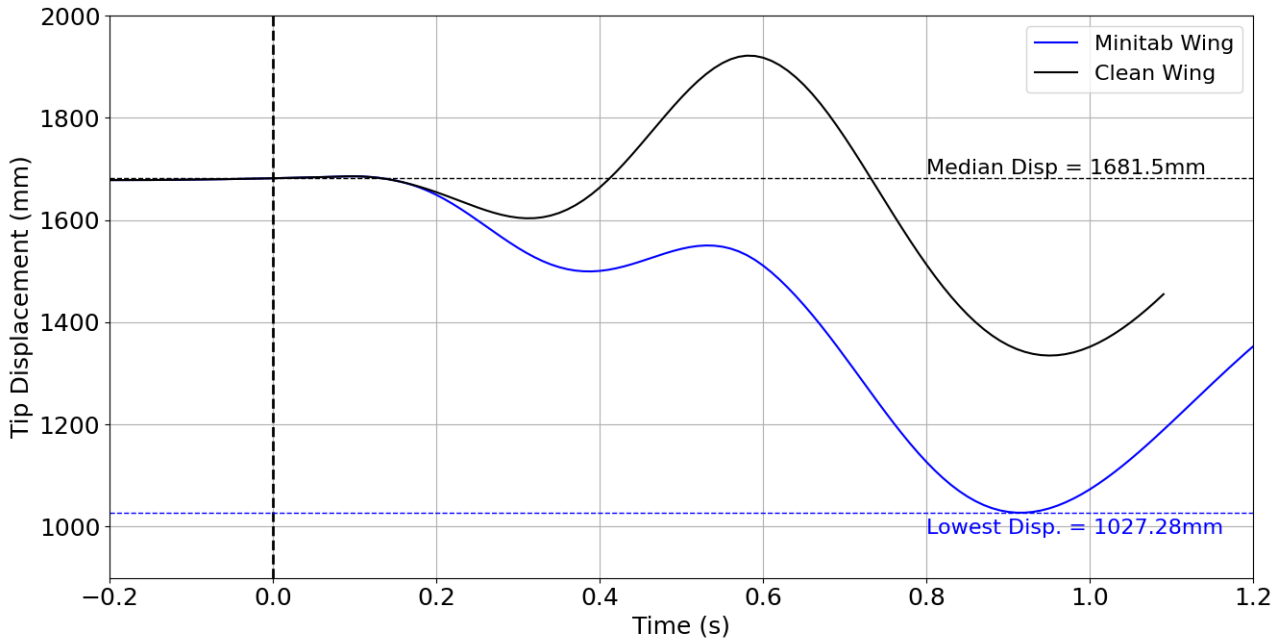


Figure 6.27: Gust G6: Variation in Tip displacement between the clean and minitab configurations

As inferred from large gust length cases in previous sections, comparing the lift coefficient variation between the clean and minitab configurations in Figure 6.26, the minitab deployment exhibits a 2.43% reduction in the peak gust load. A major result noted in this gust case is the extreme oscillation amplitude in the wing tip displacement attained as seen in Figure 6.27. Since the structure's natural bending frequency and the gust frequency are very closely matched here, there exists a near resonant behaviour between the wing structure and gust, which drives the oscillations to a higher amplitude. The resonant behaviour sustains the larger amplitude oscillations resulting in the wing tip staying in an off-nominal position for an extended period.

6.6.5. Final Conclusions

The major result of the deployment time study is that the effectiveness of the minitab in alleviating the lift load on full scale wing models is large, but only in a short time interval after its deployment, also known as the *Reaction Time*. Inclusion of flexibility into the structural model, results in the wing settling onto a new wing shape, which reduces the influence of the minitabs when left deployed over a longer duration.

The minitabs are more effective in reducing the peak loads for sharp, higher frequency gusts, rather than gusts with large lengths and subsequent longer recovery times.

The resulting motion of the wing tip due to the minitab deployment results in large oscillations of 1Hz, which matches with the 1st bending frequency of the wing. This validates the fact that the deployment of minitabs predominantly excites the 1st bending mode of the wing structure. In cases where the gust frequency is close to the 1st bending frequency, resonant behaviour emerges, resulting in larger amplitude of the wing tip oscillations and prolonged duration to recover to steady conditions.

6.7. Minitab Stowing after Gust Peak (FSI)

To determine a complete "Deploy + Stow" Timeline for a gust, the time to stow the minitab should also be considered. As seen in Section 6.3, the stowing of the minitab also has large aeroelastic effects such as large tip displacement and lift coefficient changes. A sensitivity study of the stow operation, using a non dimensional parameter STR (Stow Time Ratio) is performed for the Gust G1 case, to determine an appropriate stow time.

$$STR = \frac{T_{stow}}{\left[\frac{H}{U_\infty} \right]} \quad (6.5)$$

where T_{stow} is time at which the minitab is stowed, H is the gust length and U_∞ is the freestream velocity.

Three values of STR were chosen, starting from the moment after the gust peak passes, while keeping the minitab deployment DTR = 1.00 constant for all cases. Similar to the deployment time sensitivity, the gust onset is considered as the starting point of the timeline, $t = 0$.

Table 6.4: Minitab Stow Time (Gust G1)

Time of Gust Peak	Time of Minitab Stow	STR
0.04s	0.05s	1.25
0.04s	0.10s	2.50
0.04s	0.15s	3.75

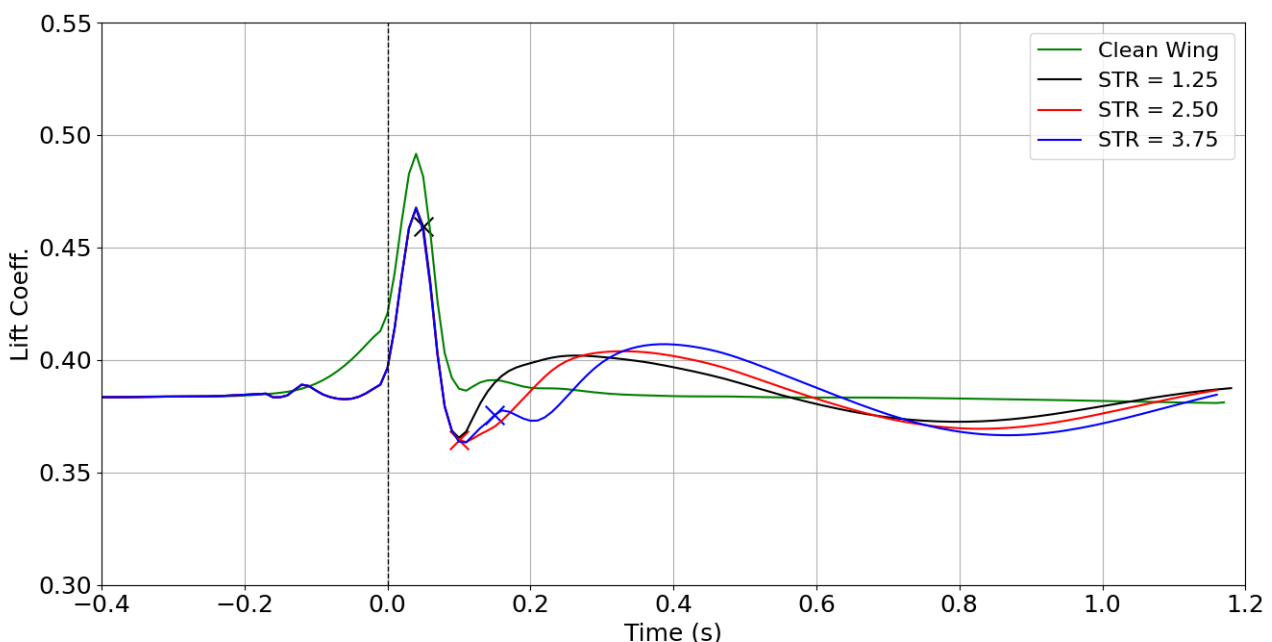


Figure 6.28: Gust G1: Lift coefficient variation in response for different STR values

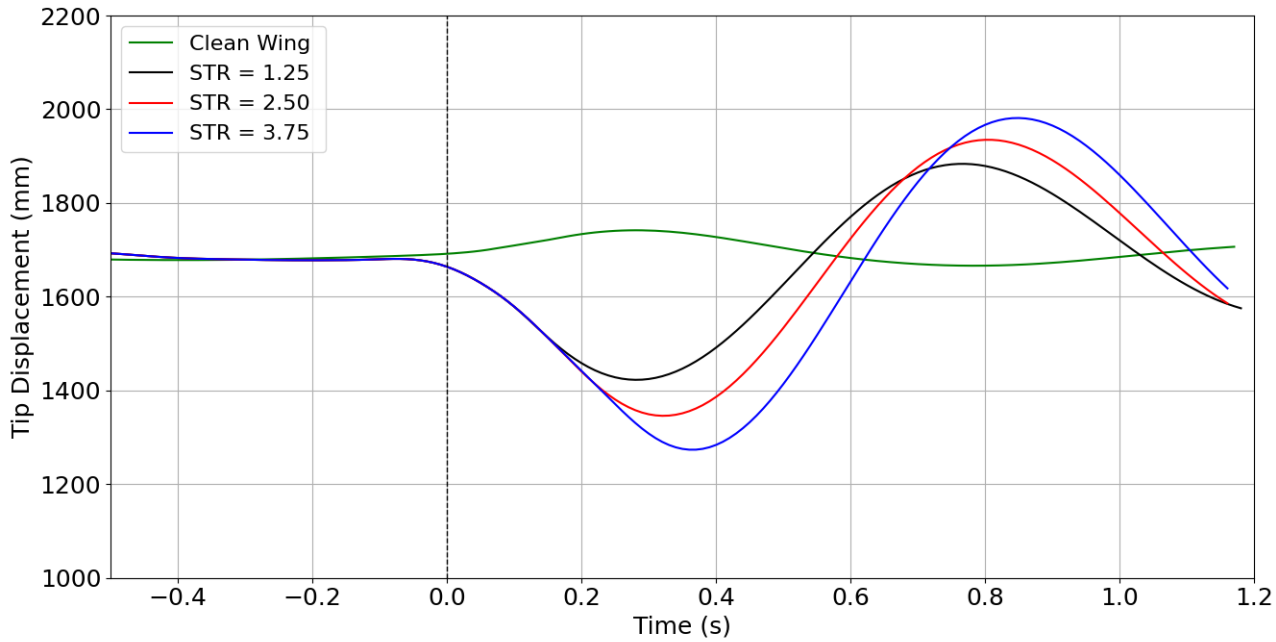


Figure 6.29: Gust G1: Wing tip displacement variation in response for different STR values

As STR values increase, indicating a longer time interval between the gust peak and minitabs stowing, the amplitude of the oscillation in the lift coefficient increases, and the recovery time to reach steady state is prolonged. Figure 6.29 demonstrates that an earlier stow time of the minitab results in a reduced amplitude oscillation of the tip towards steady state. Amplitude of the oscillations also grows with increased delay in the stow operation. The wing structure's response is a combination of excitations due to the minitab deployment, stowing and gust acting at different times which precludes an identification of a single dominant frequency of the oscillatory motion.

While the lift coefficient variation and wing tip displacement do provide a good insight into the overall response to the minitab stowing, it is important to acknowledge the limitation of this data as a factor in determining an appropriate time to stow the minitabs. Ideally, the root bending and torsion moments for the various STR values would offer a better understanding in the internal loads of the wing structure.

The data suggests that an earlier stow time of the minitabs allows the lift loads and the wing tip displacement result in reduced oscillation amplitudes and faster recovery to steady state, however due to limitations in sensing, actuation and control system response times, the operation of the minitab to respond within 0.01s of the gust peak as is the case of STR = 1.25, is not realistic, hence the chosen stow time of the minitabs will be STR = 2.50.

6.8. Final Deployment and Stow Scheme of the Minitab (FSI)

Combining all the results from the previous sections, the minitab is set to deploy at DTR = 1.00 and stow at STR = 2.50, for the gust G1 case. Ideally, all gust cases should be analyzed for an ideal deployment and stowing time, however due to the large computational and time requirements, only the case of gust G1 is analyzed within the scope of this thesis.

As illustrated in Figure 6.30, while the peak lift coefficient is reduced by 5%, there is a notable oscillatory motion in the structure tip displacement following the stowing operation. The combined effects of the minitab deployment, stowing and the gust, occurring at different times can have undesirable consequences to the wing structure. In order to determine if the oscillations are critical in terms of the internal loads, the root bending and torsion moments during the deployment and stowing operation are plotted.

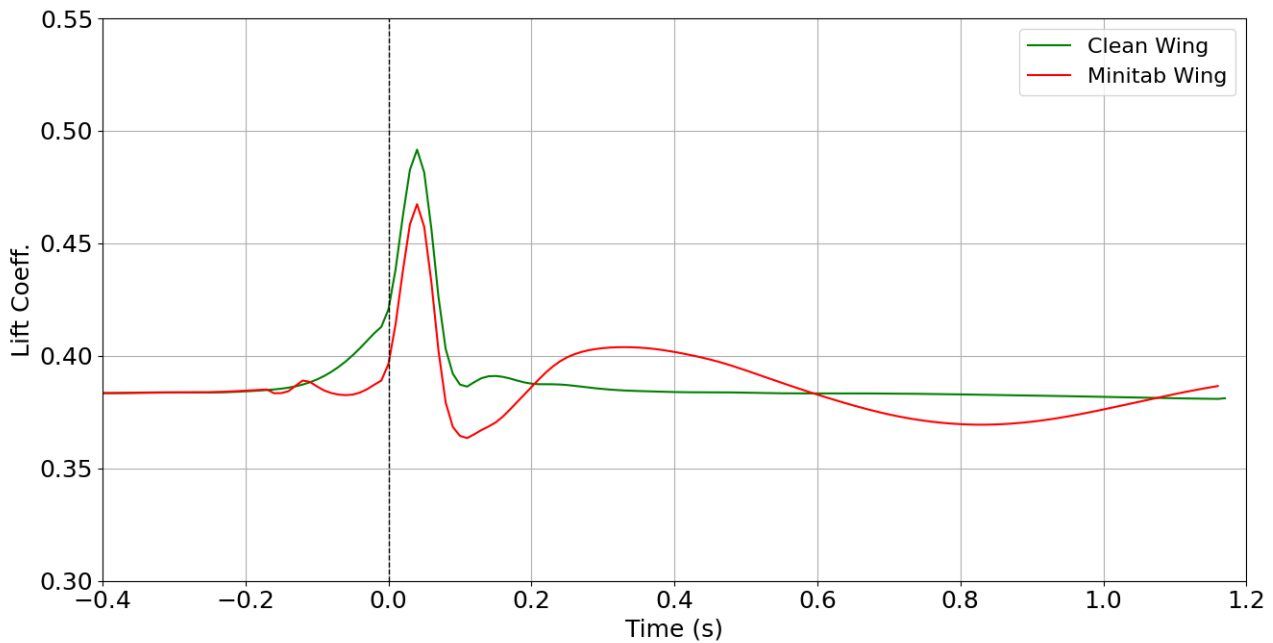


Figure 6.30: Lift Coefficient: Clean Wing and Minitab Wing with Deploy-Stow Cycle

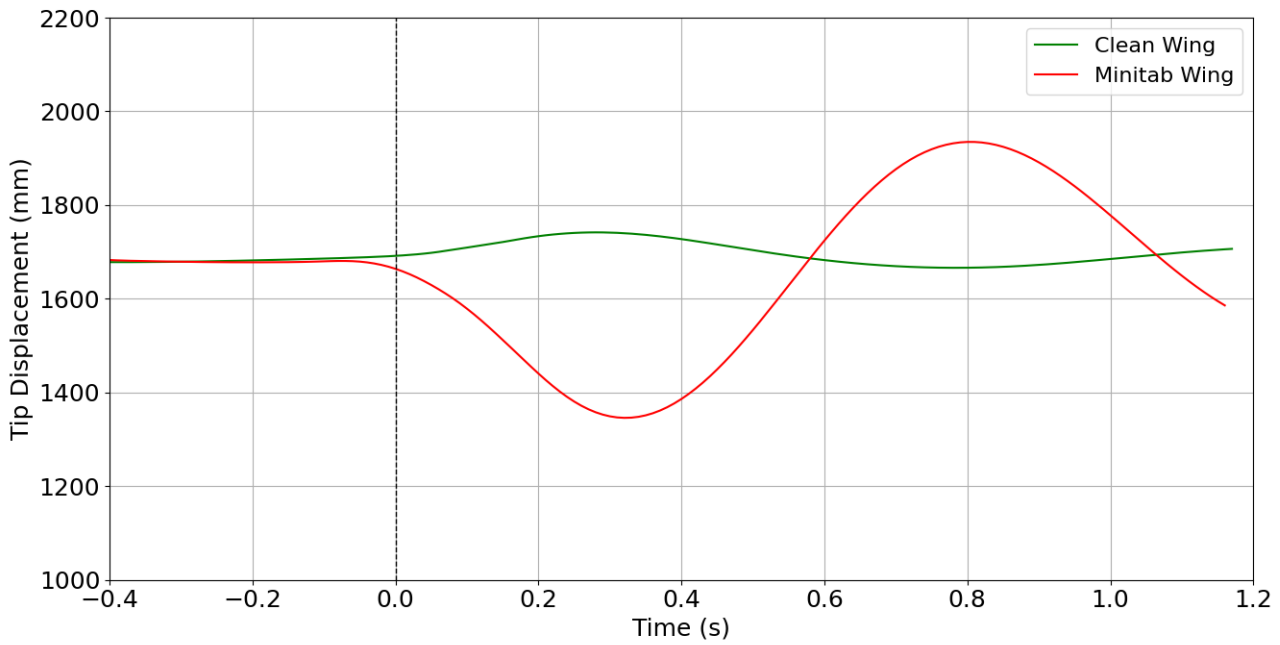


Figure 6.31: Tip Displacement: Clean Wing and Minitab Wing with Deploy-Stow Cycle

A comparative analysis of the bending moment variation between the clean and minitab configurations under the same gust conditions exhibits a peak bending moment reduction of 8.54% from the clean configuration. While the minitab reduces the peak bending moment, the subsequent stowing of the minitab introduces a sudden increase in bending moment which is followed by an pronounced oscillatory trajectory with multiple cycles, which finally converges to a steady state condition.

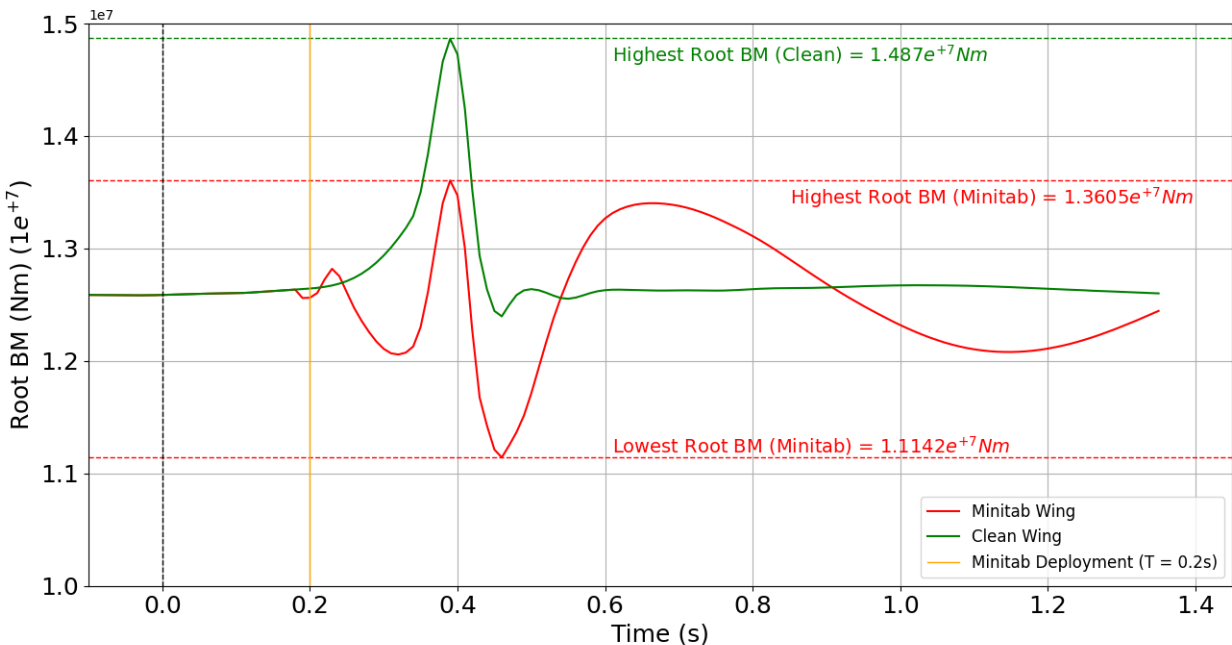


Figure 6.32: Root Bending moment variation: Clean Wing and Minitab Wing with Deploy-Stow Cycle

Examining the root torsional moment, as depicted in Figure 6.33, the minitab deployment reduces the peak torsional moment by 6%. However the subsequent stowing of the minitab induces a sharp increase in the torsional moment. This is followed by a period of oscillation before the moment gradually settles to the baseline state corresponding to the clean wing configuration.

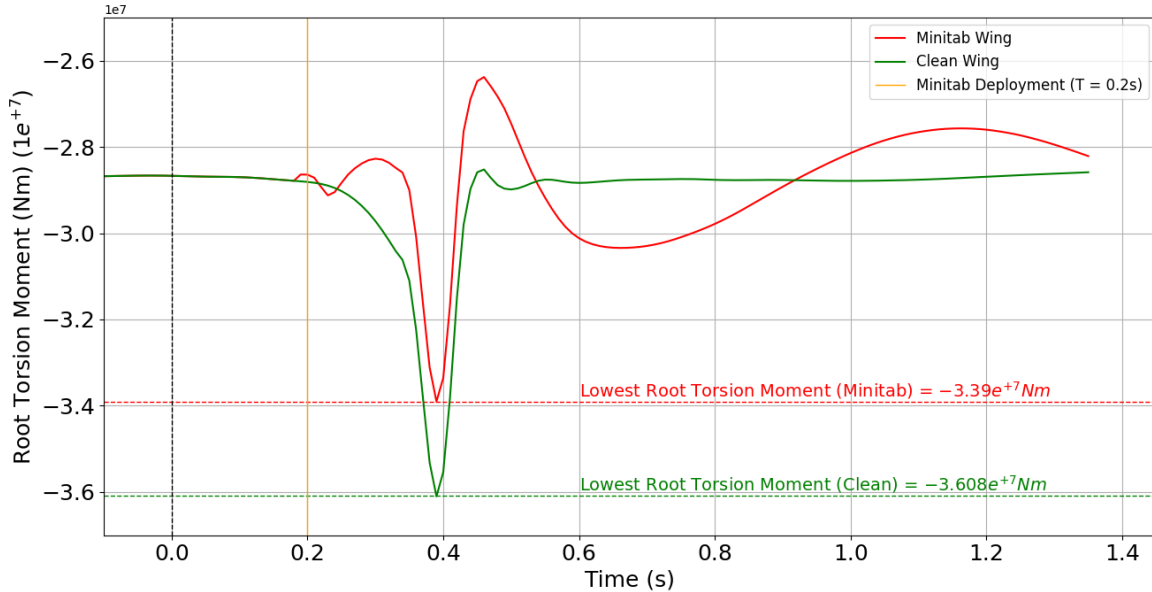


Figure 6.33: Root Torsion moment variation: Clean Wing and Minitab Wing with Deploy-Stow Cycle

Analyzing the bending and torsion moments, it indicates the resultant wing tip oscillations remain within acceptable structural limits. The magnitudes of the moments do not approach a level that would raise any concerns to the structural integrity. A consequence of the minitab deployment and stowing is the induced multiple cycle oscillations in the moment past the gust peak. While these oscillations are not severe enough to raise any structural concerns, the cumulative effect over time may contribute to a reduced fatigue life of the wing structure.

Conclusions and Future Recommendations

The objective of this thesis is to study the aeroelastic behaviour of minitabs, and determine the efficacy of the minitabs in response to gusts. Multiple minitabs were set on the upper surface of the wing, and actuation of the minitab was simulated with a boundary condition switch. With static and dynamic FSI simulations, it was shown that the combined aerodynamic and structural influence of the deployment process creates a larger load reduction than its steady state condition in a short duration.

Since the minitab deployment has a set reaction time to reach the peak load reduction, a sweep analysis of the deployment time was conducted in order to determine the most efficient time to deploy for various gusts. It was determined that the peak effectiveness of the minitab is reached when the reaction time of the minitab lines up with the time of peak gust load.

Variation in the gust lengths and gust amplitudes were also simulated with the deployment process. It was shown that the minitab loses its efficacy with larger gust lengths, and performs better for sharper, high amplitude gust. For the various gusts, when the minitab is deployed at the ideal time, it showed an average of 5.0% reduction in the peak loads.

Simulating the mid flight deployment and stowing of these minitabs showed large aeroelastic effects, with large tip oscillations, which dominated over the motion induced due to the gust itself. These oscillations were determined to be primarily a 1st bending mode oscillation of approximately 1Hz. Gusts with frequencies close to the structure 1st bending frequency were determined to be the limiting case. Emergence of resonant behaviour with the minitab deployment for that particular gust frequency, resulted in large oscillation amplitudes and longer recovery times as compared to other gust lengths. While the motion of the structure is primarily the 1st bending mode, analyzing the frequency content of the responses due to the minitab deployment/stowing and the gusts will determine the critical modes of the structure that are excited and need to be dealt with.

With the complete minitab deployment and stowing process in response to a gust, the peak lift due to the gust was reduced, but it was followed by a oscillating motion of the wing. Evaluating the root bending and torsion moments, it showed that while the peak value of the moments due to the gust were reduced by the minitab, the lower amplitude oscillations persisted with multiple cycles, which is a potential concern for the internal structure's fatigue life.

The inclusion of flexibility to the wing, reduces the performance of the minitab, when compared to the rigid wing static CFD results from previous studies however, the minitabs still prove to be a effective as a load alleviation method. Conducting aeroelastic studies of various configurations of the minitabs, in terms of its geometry, placement location and quantity must be tested before implementation. The large aeroelastic effects and strong influence in the structure motion has shown certain undesirable effects in terms of large displacements prolonged cyclic loads and moments, which can be a potential fatigue lift concern, hence should be studied separately through wind tunnel tests of intricate and realistic structural models.

The simplification of the structural model to a beam model, limited the detail in which the shape of the wing changed due to the minitab. Transonic flow is highly sensitive to the wall surface motion and deformation. Inclusion of the wingbox as the structure model will provide a more detailed image of the wing shape and obtain better characteristics of the flow such as shock wave positions, flow separations and a more detailed representation of the wing geometry. Additionally, since results from this thesis along with results of the static CFD results show good confidence in the concept of the minitab, the next stage in evaluating this concept will be prototyping a scaled wing model with these minitabs. Wind tunnel testing of these models in gust conditions, will obtain real world responses and data on the performance of the minitabs.

Finally, the original concept of the ASVG, has a deployment and stow operation by rotating the minitab, compared to the ON/OFF method, that was tested in this thesis. This abrupt boundary condition can introduce unintended responses and effects in the aerodynamics and structural responses into the results. Inclusion of the rotation motion of the ASVG from the VG to the minitab configuration and back will provide a better idea of the performance of the proposed concept and capture any new flow and aeroelastic phenomena emerging due to the rotatory motion.

References

- [1] Xavier Carrillo Córcoles. "An experimental study on flared folding wingtips". eng. In: *Master's Thesis, TU Delft* (2022).
- [2] GL Crouse Jr et al. "Transonic aeroelasticity analysis using state-space unsteady aerodynamic modeling". In: *Journal of Aircraft* 29.1 (1992), pp. 153–160.
- [3] K.J. Badcock et al. "Transonic aeroelastic simulation for instability searches and uncertainty analysis". In: *Progress in Aerospace Sciences* 47.5 (2011), pp. 392–423. DOI: <https://doi.org/10.1016/j.paerosci.2011.05.002>. URL: <https://www.sciencedirect.com/science/article/pii/S0376042111000352>.
- [4] National Archives Office of the Federal Register et al. "14 CFR § 25.341 - Gust and turbulence loads". In: *Office of the Federal Register, National Archives and Records Administration* (). URL: <https://www.govinfo.gov/app/details/CFR-2020-title14-vol1/CFR-2020-title14-vol1-sec25-341>.
- [5] 2020 EASA. "CS-25 Amendment 26: Certification specifications and acceptable means of compliance for large aeroplanes." In: (2020). URL: <https://www.easa.europa.eu/en/document-library/certification-specifications/cs-25-amendment-26-0>.
- [6] Luca Marino et al. "Parametric study of a switchable vortex generator for load alleviation in transonic conditions". In: *AIAA SCITECH 2024 Forum*. DOI: 10.2514/6.2024-2110. URL: <https://arc.aiaa.org/doi/abs/10.2514/6.2024-2110>.
- [7] Yonghong Li et al. "A Review of Flow Control for Gust Load Alleviation". In: *Applied Sciences* 12.20 (2022). DOI: 10.3390/app122010537. URL: <https://www.mdpi.com/2076-3417/12/20/10537>.
- [8] D. J. Heathcote et al. "Aerodynamic Load Alleviation Using Minitabs". In: *Journal of Aircraft* 55.5 (2018), pp. 2068–2077. DOI: 10.2514/1.C034574.
- [9] Peter Bjørn Andersen. "Advanced Load Alleviation for Wind Turbines using Adaptive Trailing Edge Flaps: Sensoring and Control". eng. 2010.
- [10] Tianshu Liu et al. "Thin-Airfoil Theoretical Interpretation for Gurney Flap Lift Enhancement". In: *Journal of Aircraft* (2007). DOI: 10.2514/1.27680.
- [11] Aubryn M Cooperman et al. "Active load control of a wind turbine airfoil using microtabs". In: *Journal of Aircraft* 50.4 (2013), pp. 1150–1158.
- [12] J. Alber et al. "Aerodynamic effects of Gurney flaps on the rotor blades of a research wind turbine". In: *Wind Energy Science* 5.4 (2020), pp. 1645–1662. DOI: 10.5194/wes-5-1645-2020. URL: <https://wes.copernicus.org/articles/5/1645/2020/>.
- [13] J. P. Baker et al. "Two-Dimensional Wind Tunnel and Computational Investigation of a Microtab Modified Airfoil". In: *Journal of Aircraft* 44.2 (2007), pp. 563–572. DOI: 10.2514/1.24502.
- [14] E. N Jacobs. "Airfoil Section Characteristics as Affected by Protuberances". eng. 1934.
- [15] Ilias Kiat. "Parametric investigation of mini-tab for load alleviation". eng. In: *Master's Thesis, TU Delft* (2024).

- [16] John Vassberg et al. "Development of a common research model for applied CFD validation studies". In: *26th AIAA applied aerodynamics conference*. 2008, p. 6919.
- [17] Timothy R. Brooks et al. "Undeflected common research model (uCRM): An aerostructural model for the study of high aspect ratio transport aircraft wings". In: 2017. URL: <https://api.semanticscholar.org/CorpusID:115319111>.
- [18] Dassault Systems. *Ruled Surfaces and the Ruled Surface PropertyManager*. URL: https://help.solidworks.com/2019/english/SolidWorks/sldworks/c_mold_tools_ruled_surfaces.htm.
- [19] John D. Anderson. *Fundamentals of aerodynamics*. 5th. McGraw-Hill, Feb. 2011. URL: <http://www.worldcat.org/isbn/9780073398105>.
- [20] Koichi Hashiguchi. "Chapter 5 - Conservation laws and stress tensors". In: *Nonlinear Continuum Mechanics for Finite Elasticity-Plasticity*. Ed. by Koichi Hashiguchi. Elsevier, 2020, pp. 123–149. DOI: <https://doi.org/10.1016/B978-0-12-819428-7.00005-5>. URL: <https://www.sciencedirect.com/science/article/pii/B9780128194287000055>.
- [21] Jurij Sodja. "Turbulence models in CFD". In: *University of Ljubljana* (2007), pp. 1–18.
- [22] Pietro Catalano et al. "An evaluation of RANS turbulence modelling for aerodynamic applications". In: *Aerospace Science and Technology* 7.7 (2003), pp. 493–509. DOI: [https://doi.org/10.1016/S1270-9638\(03\)00061-0](https://doi.org/10.1016/S1270-9638(03)00061-0). URL: <https://www.sciencedirect.com/science/article/pii/S1270963803000610>.
- [23] Shibo Wang et al. "The performance of different turbulence models (URANS, SAS and DES) for predicting high-speed train slipstream". In: *Journal of Wind Engineering and Industrial Aerodynamics* 165 (2017), pp. 46–57. DOI: <https://doi.org/10.1016/j.jweia.2017.03.001>. URL: <https://www.sciencedirect.com/science/article/pii/S0167610516307243>.
- [24] R Nichols. "Applications of RANS/LES turbulence models". In: *41st Aerospace Sciences Meeting and Exhibit*. 2003, p. 83.
- [25] Chuanqiang Gao et al. "Transonic aeroelasticity: A new perspective from the fluid mode". In: *Progress in Aerospace Sciences* 113 (Feb. 2020), p. 100596. DOI: [10.1016/j.paerosci.2019.100596](https://doi.org/10.1016/j.paerosci.2019.100596).
- [26] Xiaoshu Lü et al. "Improving the Energy Efficiency of Buildings Based on Fluid Dynamics Models: A Critical Review". In: *Energies* 14 (Aug. 2021), p. 5384. DOI: [10.3390/en14175384](https://doi.org/10.3390/en14175384).
- [27] François G Schmitt. "About Boussinesq's turbulent viscosity hypothesis: historical remarks and a direct evaluation of its validity". In: *Comptes Rendus Mécanique* 335.9-10 (Oct. 2007), pp. 617–627. DOI: [10.1016/j.crme.2007.08.004](https://doi.org/10.1016/j.crme.2007.08.004). URL: <https://hal.science/hal-00264386>.
- [28] Cadence CFD. *What is the Spalart Allmaras Turbulence Model?* 2022. URL: <https://resources.system-analysis.cadence.com/blog/msa2024-what-is-the-spalart-allmaras-turbulence-model>.
- [29] Daniel Pineiro Rielo. "Development of a Fluid-Structure Interaction simulation algorithm for the analysis of the static and dynamic". In: *Master's thesis, Universidade de Vigo (Spain) - Delft University of Technology (The Netherlands)* (2019).
- [30] F KISSLING. "Ground vibration test- A tool for rotorcraft dynamic and aeroelastic investigations". In: *(European Rotorcraft and Powered Lift Aircraft Forum, University of Southampton, Southampton, England, Sept. 22-24, 1975.) Vertica*, vol. 1. 2. 1976, pp. 149–163.

-
- [31] Paul M.G.J Lancelot. "Transonic Wing and Control Surface Loads Modelling for Aerostervoelastic Analysis". eng. 2023. DOI: <https://doi.org/10.4233/uuid:e37566e8-cb46-4f90-863d-9cfe0b634507>.
 - [32] Rachel Leuthold. "Multiple-Wake Vortex Lattice Method for Membrane-Wing Kites". PhD thesis. Dec. 2015. DOI: 10.13140/RG.2.2.30811.41765.
 - [33] M. Sayed et al. "Aeroelastic Simulations Based on High-Fidelity CFD and CSD Models". In: *Handbook of Wind Energy Aerodynamics*. Ed. by Bernhard Stoevesandt et al. Cham: Springer International Publishing, 2022, pp. 491–558. DOI: 10.1007/978-3-030-31307-4_22.
 - [34] R.L. Taylor O.C. Zienkiewicz et al. "The Finite Element Method for Fluid Dynamics". In: *Handbook of Wind Energy Aerodynamics*. Butterworth-Heinemann, 2014. URL: <https://www.sciencedirect.com/book/9781856176354/the-finite-element-method-for-fluid-dynamics>.
 - [35] Elie Kahale et al. *autonomous path tracking of a kinematic airship in presence of unknown gust*. Oct. 2013.
 - [36] MDO Lab. "uCRM: undeflected Common Research Model". In: *Mendeley Data* V1 (2019). URL: 10.17632/gpk4zn73xn.1.

A

Appendix

A.1. CAD Modelling Minitabs (Complete Procedure)

1. Download and import the uCRM9 geometry as provided by MDO Lab[36] based on the work of Brookes et al.[17]. Scale it according to the size required by the user.



Figure A.1: CAD Model of the uCRM9 Wing

2. From a plan view, project the footprint of the wing as a sketch on to a parallel plane.
3. Next step will be to create a spline which maintains a constant local chord ratio distance from the leading edge. For this thesis, a local chord ration of $x/c = 0.15$ was taken. A spline here is required due to the changing chord length across the span of the wing.
 - 3.1. Create a parallel linear pattern of the wing root edge with 12 instances from the root to the tip.
 - 3.2. Trim out the excess length of the line outside the planform area of the wing. The original projection sketch of the wing planform will be the tool to trim out the excess length.
 - 3.3. Measure the lengths of each of these 12 instances and mark a point 15% of its respective length from the leading edge.
 - 3.4. Use the '**Spline Tool**' to create a spline passing through all the 12 created points.

See Figure A.2 to obtain a visual of the sketch created in step 3.

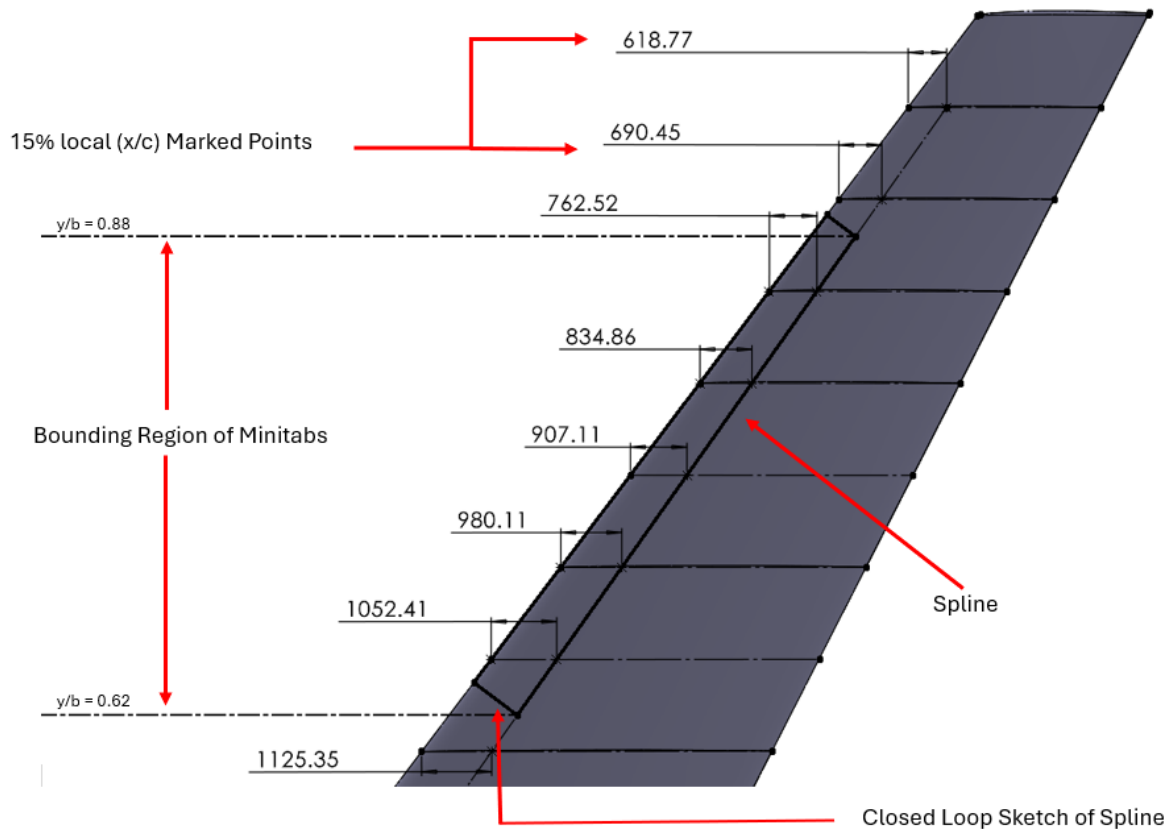


Figure A.2: Spline Sketch

4. Mark the section of the span which will have the minitabs and draw 2 construction lines parallel to the wing root, bounding the region of the minitabs. For this thesis, a span of $y/b = 0.62$ to 0.88 was chosen, which is referred from the previously conducted CFD study of minitabs[15].
Set the parts of the Spline not within the region of the minitabs as construction lines.
5. Once the spline is complete, close the spline into a loop by creating a rectangle with the spline as one of the sides. Ensure this rectangle lies within the planform area of the uCRM9 wing. This can be seen in Figure A.2, where in the leading edge and the spline are a part of the closed loop. This is required since the spline will be converted into an edge in a future step. Since the edge creation process, requires a closed loop sketch, a single line/spline will not be sufficient.
6. Once the closed loop is complete, convert all the remaining sketch entities, apart from the closed loop with the spline into construction lines.
This will ensure no visibility of these sketch entities nor unnecessary interference in future steps.
7. Select the '**Split Line**' command:
 - 7.1. Set the Type of Split to '**Projection**' to project this sketch back to the surface of the wing.
 - 7.2. In the Sketch Selections Window, select the closed loop sketch created in the previous step.
 - 7.3. In the Surface Selections Window, select the surface over which the user wants to create the minitab over. In this case, it is projected to the upper surface of the wing.

This step will split the wing surface and create edges in the shape of the sketch on the wing surface as seen in Figure A.3.

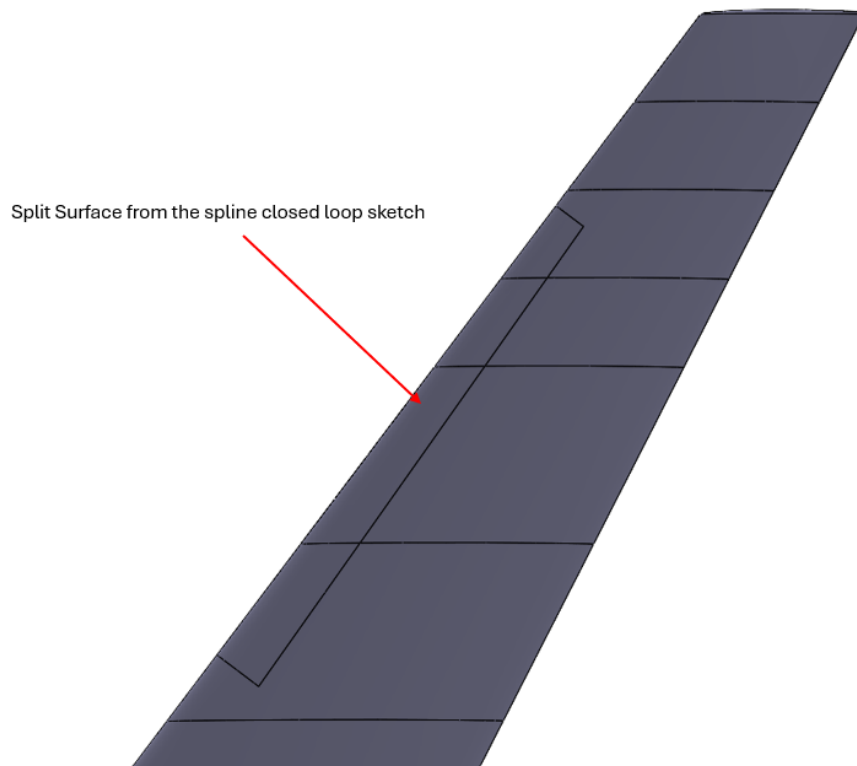


Figure A.3: Spline Surface Split Sketch

8. Select the '**Ruled Surface**' command:
 - 8.1. Set the type to '**Normal to Surface**'
 - 8.2. Set the '**Distance**' to the desired height of the minitab. For this case, 30mm was chosen.
 - 8.3. In the '**Edge Selection**' window, select the spline as the edge to draw the surface from.
 - 8.4. Ensure the option '**Connecting Surface**' is enabled. This ensures a connection between the created surface and the underlying wing body.

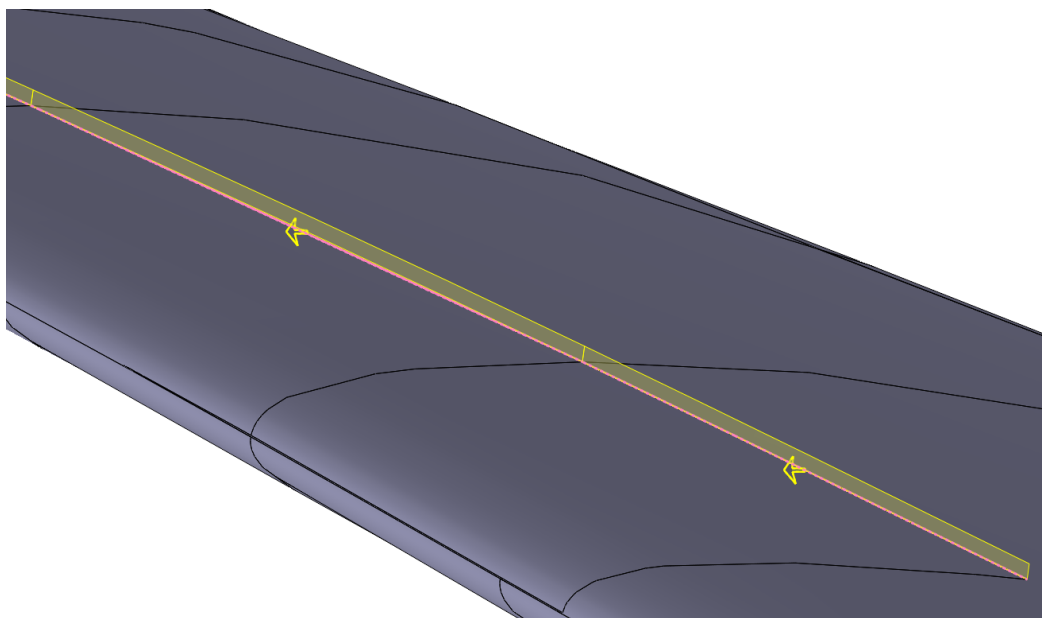


Figure A.4: Ruled Surface Preview

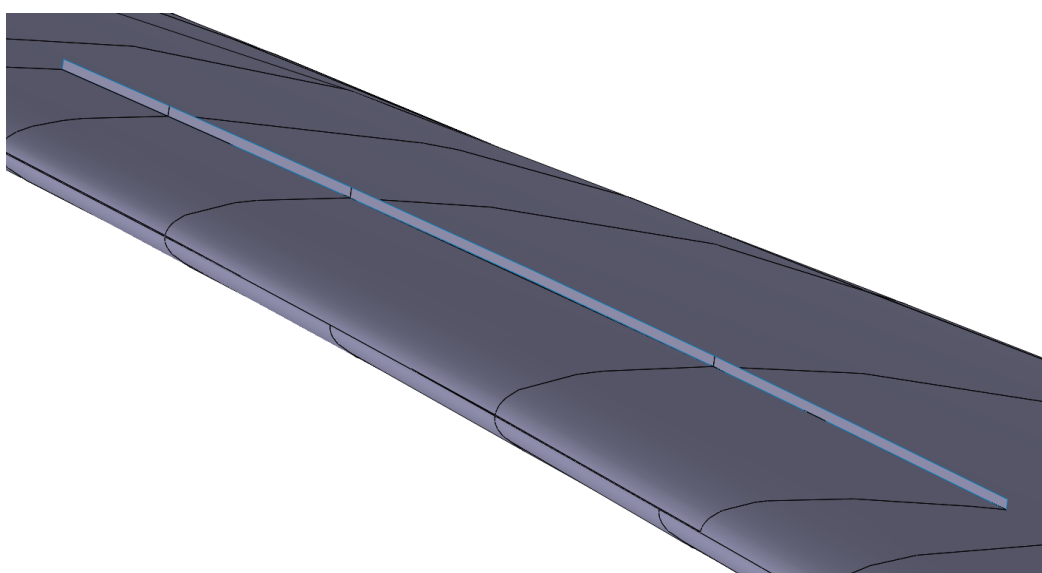


Figure A.5: Completed Minitab Surface of Wall Ratio = 1

This step will create a single continuous minitab of Wall Ratio = 1 along the chosen span of the wing.

Modelling Multiple Minitabs

9. In order to split this into multiple minitabs, section the created spline in Step 4 based on the required geometry, wall ratio and number of instances of the minitab.

Ensure that each section of the spline that will be a minitab, should have its own separate closed loop sketch. In simpler terms, the user must repeat step 5 for each instance of the minitab.

An advantage of this method is the ease in creating multiple iterations to the minitab layout,

number of instances and sizes without recreating the spline which is the most time consuming step of the complete process for each minitab.

10. Finally, in step 8, in the '**Edge Selection**' window, only select the edges which will become the minitab instances.

A drawback to this process is the requirement for a closed loop to create the edges on the wing surface. This leads to unnecessary split of a clean wing surface into multiple smaller surfaces as seen in Figure A.6, which is an example of a model with Minitab Wall Ratio = 0.4. This can cause potential meshing and topological issues when the fluid domain is created down the line. A simple fix for this issue can be summarised into the following steps:

1. Save the created geometry at the end of Step 10 as a (.STEP) file.
2. Open a new instance of SolidWorks and import the clean uCRM9 wing from Step 1
3. Insert the created minitab geometry at the end of step 10 into the current geometry.
4. Delete the instance of the wing with the split surfaces, while retaining the minitab surface bodies
5. Enable Shared Topology between the minitab surfaces and the clean uCRM9 wing.

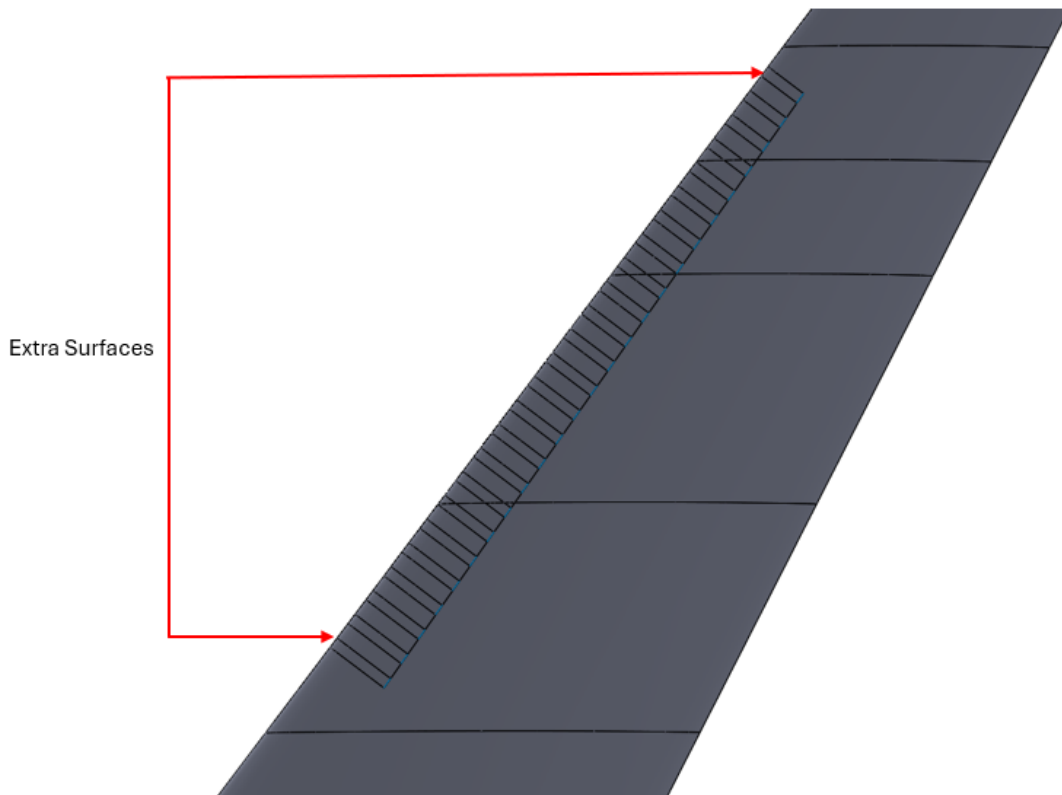


Figure A.6: Additional Surfaces due to Split Line Command (Wall Ratio = 0.4)

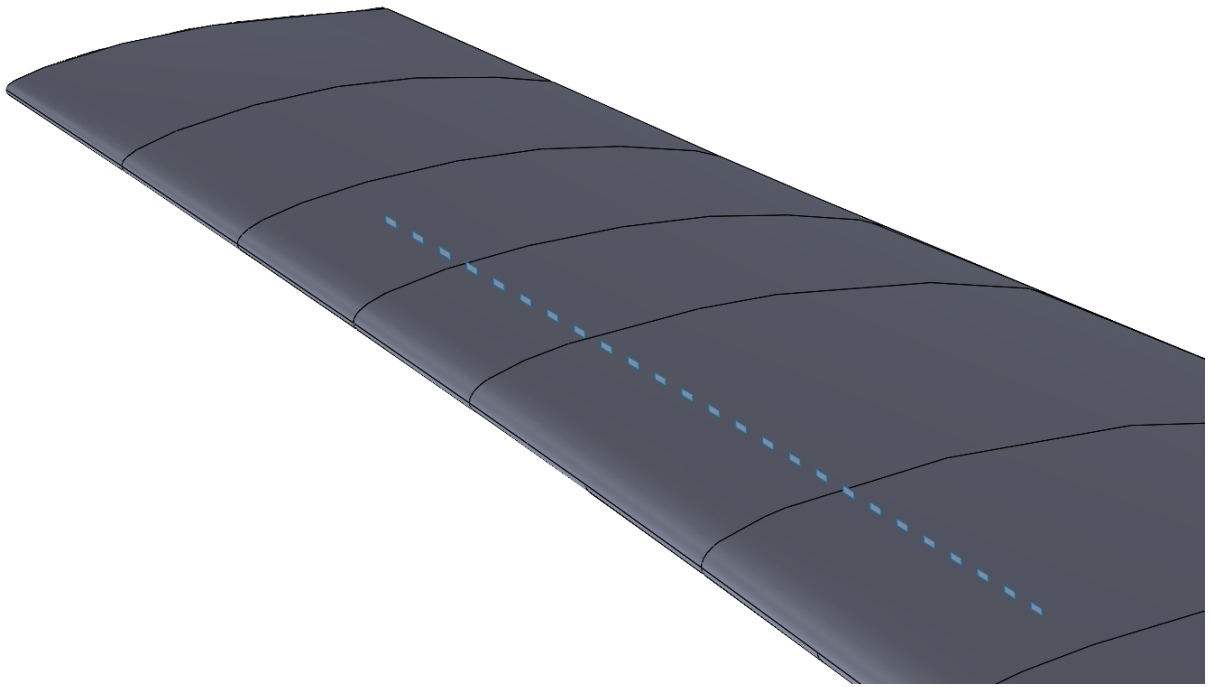


Figure A.7: Example of a Fixed Version of Minitab Surface Model (Wall Ratio = 0.4)

A.2. Damping Coefficient Sensitivity Study

Dynamic FSI Results of the clean wing in gust conditions from Pinero [29] was chosen as the comparison case. Each variation of the damping method and its parameters from Section 3.3.2 was setup as separate test cases and an overall comparison was done as seen in Figure A.10 and Figure A.8. One of the key takeaways from the study was, even a small addition of damping was sufficient to eliminate low frequency oscillations that exist with no damping included. The peak Cl values reached with all the damping cases were very similar, all ranging with 1% of each other.

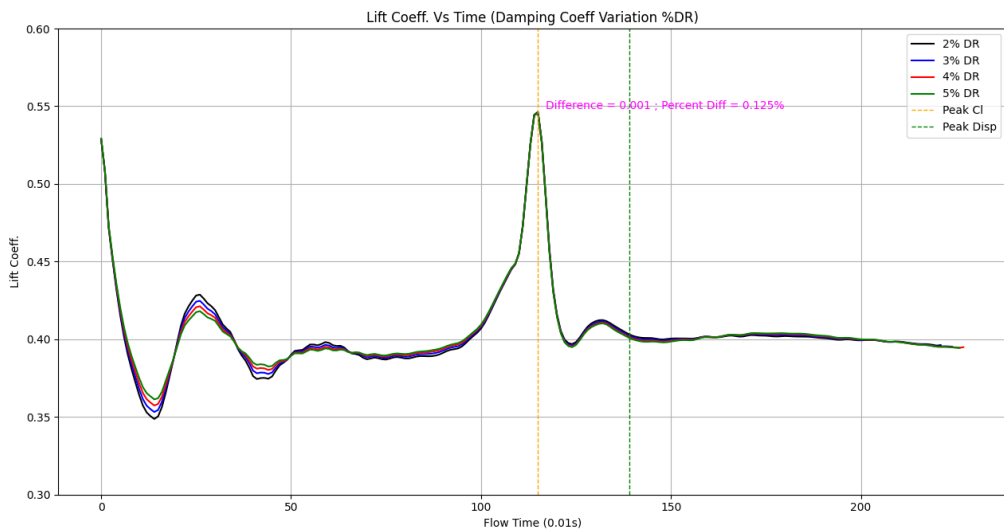


Figure A.8: Lift Coefficient vs Timestep (Modal Damping)

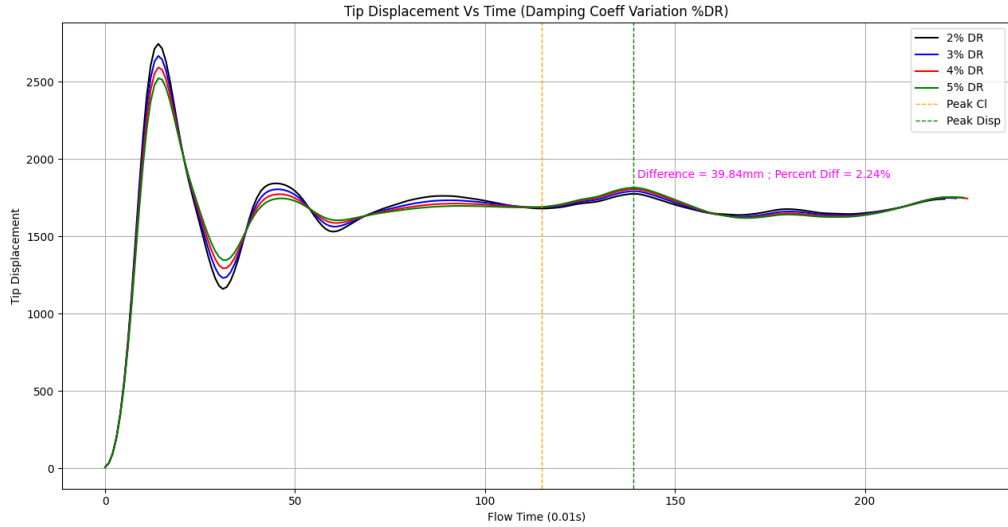


Figure A.9: Tip Displacement vs Timestep (Modal Damping)

Results from the Modal Damping cases showed small high frequency oscillations that persists throughout the simulation, but the cause was unable to be determined. However, comparing all the tested damping ratios (ζ), it showed negligible differences.

The tip displacement also showed the same high frequency oscillations, and a general lack of stability in the tip displacement, before and after the gust encounter.

Hence the modal damping method was not chosen, due to the presence of the higher frequency oscillations, lack of stability in the tip displacement and the selection of the damping ratio could not be justified without additional information.

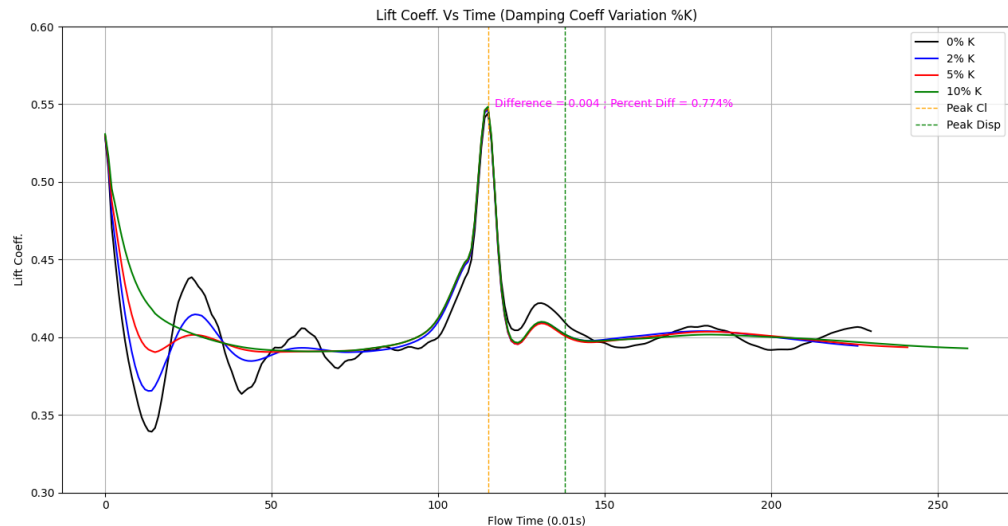


Figure A.10: Lift Coefficient vs Timestep (Rayleigh Damping)

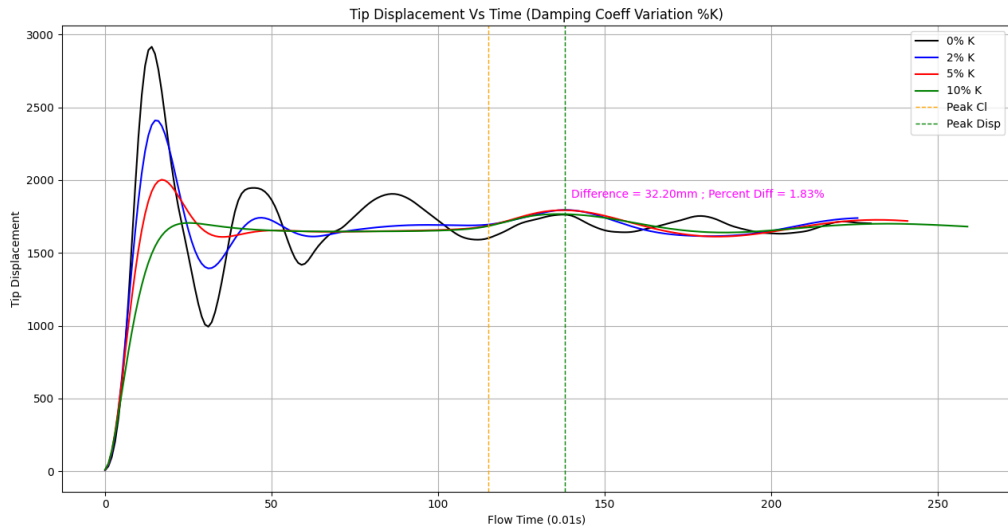


Figure A.11: Tip Displacement vs Timestep (Modal Damping)

Results from the Rayleigh Damping cases showed that 2% (K) damping was still resulting in very low frequency and low amplitude oscillations. With a value of 10% (K), the lift coefficient was over-damped, which can be noticed in the initial timesteps of the simulation, with the lack of any oscillations to a stable value. An intermediate value of 5% (K), showed slight over-damping behaviour, but is believed to show relatively good agreement with typical behaviour of structures and valid for the dynamic FSI simulations.

A.3. Minitab Deployment on Gust cases (G2, G3)

Results of the minitab deployment for gusts G2 and G3 are shown below:

A.3.1. Case 2: Gust G2

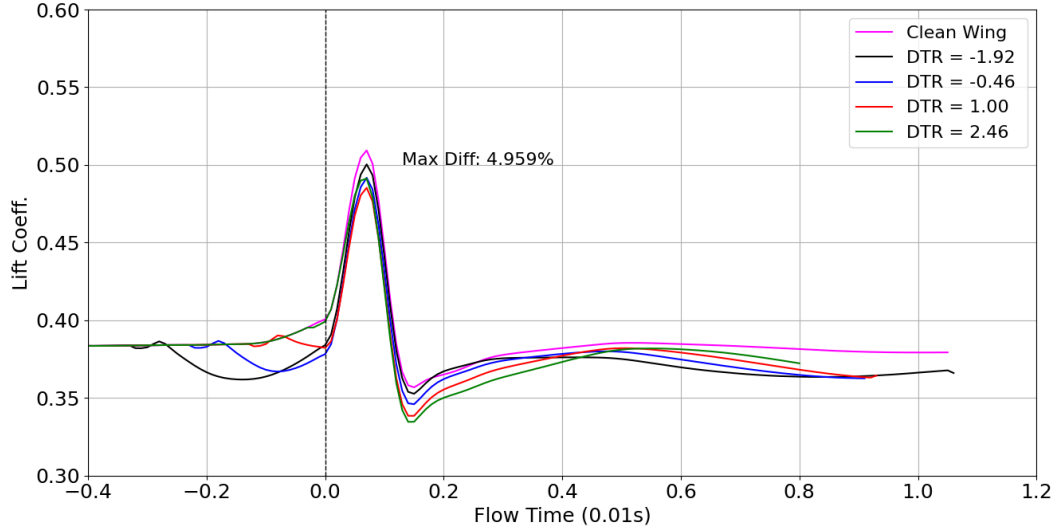


Figure A.12: Lift Coefficient vs Timestep (Gust G2)

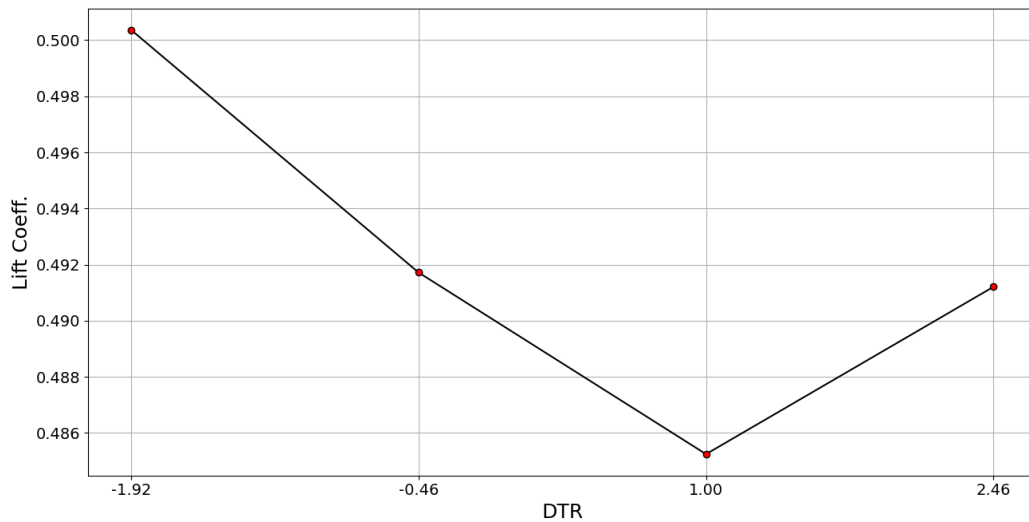


Figure A.13: Lift Coefficient at Gust Peak (G2) vs DTR Configurations

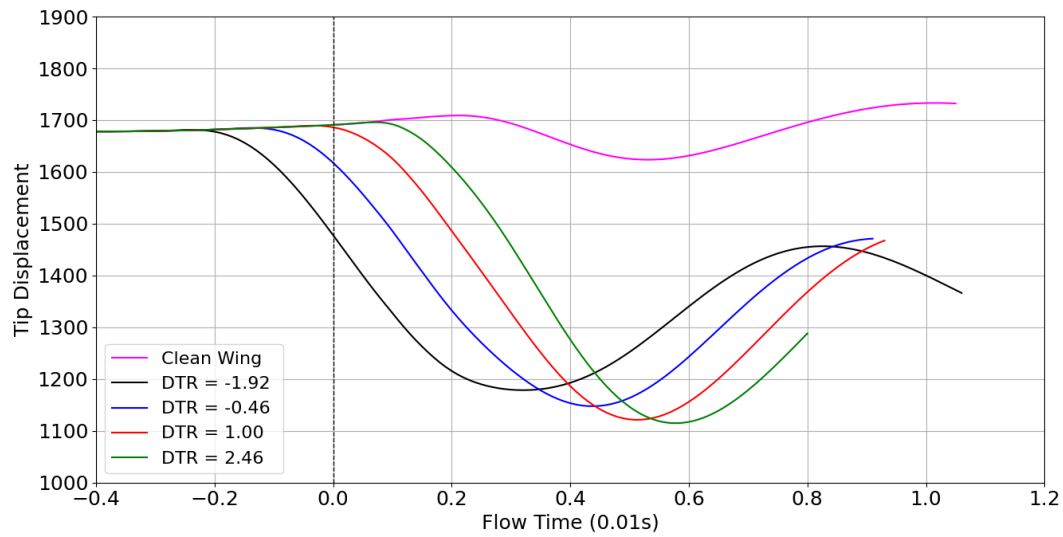


Figure A.14: Tip Displacement vs Timestep with (Gust G2)

A.3.2. Case 3: Gust G3

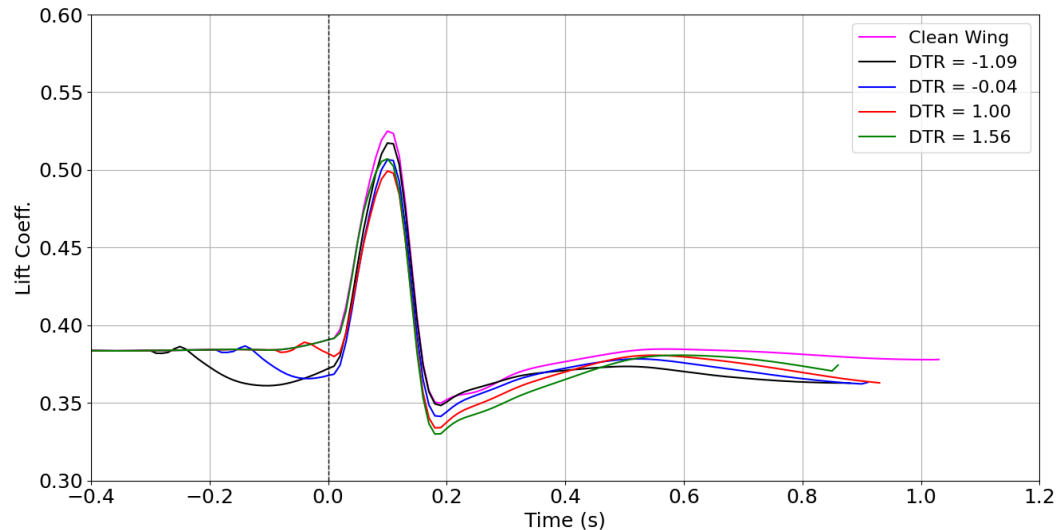


Figure A.15: Lift Coefficient vs Timestep (Gust G3)

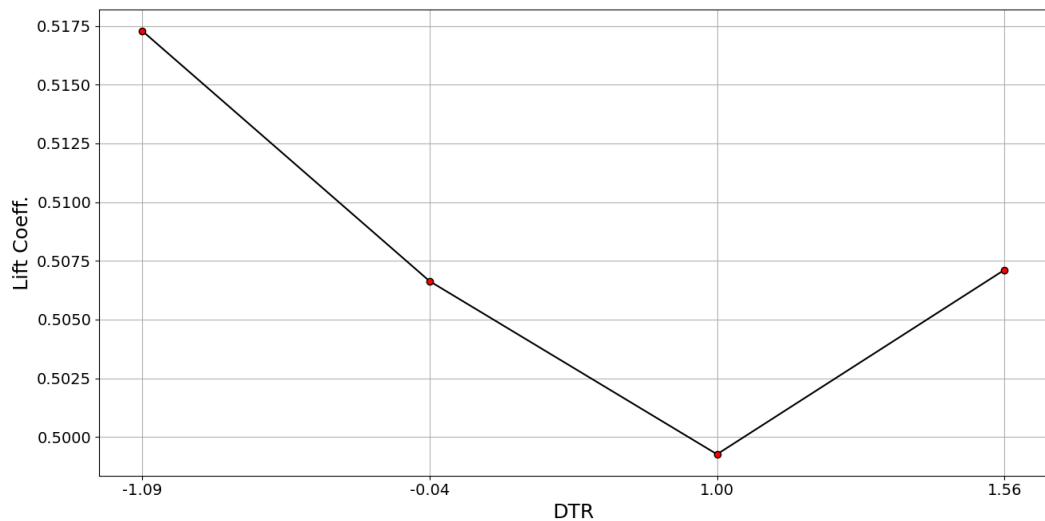


Figure A.16: Lift Coefficient at Gust Peak (G3) vs DTR Configurations

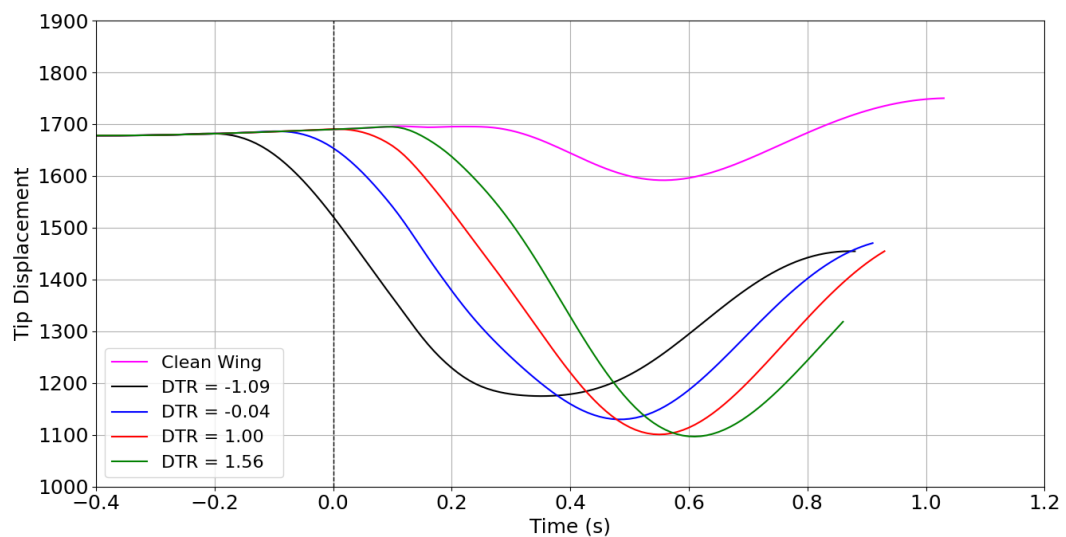


Figure A.17: Tip Displacement vs Timestep with (Gust G3)